

Benchmarking Chest X-ray Diagnosis Models Across Multinational Datasets

Qinmei Xu^{1#}, Yiheng Li^{1#}, Xianghao Zhan¹, Ahmet Gorkem Er¹, Brittany Dashevsky², Chuanjun Xu⁴, Mohammed Alawad⁵, Mengya Yang⁶, Liu Ya⁶, Changsheng Zhou⁶, Xiao Li⁶, Haruka Itakura³, Olivier Gevaert^{1*}

[1] Stanford Center for Biomedical Informatics Research (BMIR), Department of Medicine, Stanford University, Stanford, CA, USA

[2] Stanford Breast Imaging, Department of Radiology, Stanford University, Stanford, CA, USA

[3] Division of Oncology, Department of Medicine, Stanford University, Stanford, CA, USA

[4] Department of Radiology, the Second Hospital of Nanjing, Nanjing University of Chinese Medicine, Nanjing, China

[5] National Center for AI (NCAI), Saudi Data and AI Authority (SDAIA), Riyadh, Saudi Arabia

[6] Department of Radiology, Jinling Hospital, Nanjing, Jiangsu, China

These authors contributed equally to this work.

* Corresponding author: olivier.gevaert@stanford.edu

Abstract

Foundation models leveraging vision-language pretraining have shown promise in chest X-ray (CXR) interpretation, yet their real-world performance across diverse populations and diagnostic tasks remains insufficiently evaluated. This study benchmarks the diagnostic performance and generalizability of foundation models versus traditional convolutional neural networks (CNNs) on multinational CXR datasets. We evaluated eight CXR diagnostic models - five vision-language foundation models and three CNN-based architectures - across 37 standardized classification tasks using six public datasets from the USA, Spain, India, and Vietnam, and three private datasets from hospitals in China. Performance was assessed using AUROC, AUPRC, and other metrics across both shared and dataset-specific tasks. Foundation models outperformed CNNs in both accuracy and task coverage. MAVL, a model incorporating knowledge-enhanced prompts and structured supervision, achieved the highest performance on public (mean AUROC: 0.82; AUPRC: 0.32) and private (mean AUROC: 0.95; AUPRC: 0.89) datasets, ranking first in 14 of 37 public and 3 of 4 private tasks. All models showed reduced performance on pediatric cases, with average AUROC dropping from 0.88 +/- 0.18 in adults to 0.57 +/- 0.29 in children ($p = 0.0202$). These findings highlight the value of structured supervision and prompt design in radiologic AI and suggest future directions including geographic expansion and ensemble modeling for clinical deployment. Code for all evaluated models is available at

<https://drive.google.com/drive/folders/1B99yMQm7bB4h1sVMIBja0RfUu8gLktCE>

Introduction

Chest radiography remains one of the most widely used diagnostic imaging modalities worldwide, playing a pivotal role in the evaluation of thoracic conditions such as pneumonia, pneumothorax, and pulmonary nodules [1–3]. With rising clinical workloads and growing demands for rapid interpretation, machine learning [4-9]—particularly deep learning—based models [10-13]—has emerged as a promising solution for automated and scalable chest X-ray analysis [14-15]. Traditional convolutional neural networks (CNNs), including DenseNet and ResNet [14], have demonstrated strong performance on large-scale public datasets such as CheXpert, PadChest, and VinDr-CXR [16–20]. However, these models are constrained by their reliance on manually labeled training data, limited adaptability to new clinical environments, and poor generalization across demographic and geographic domains.

Recently, foundation models—particularly vision-language models trained with contrastive or cross-modal supervision—have shown great potential in medical image analysis [21–25]. These models align visual features with textual disease descriptions, enabling few-shot and zero-shot classification without extensive retraining. Architectures such as CheXzero [21], BioViL-T [22], MAVL [23], MedKLIP [24], and PsPG [25] extend this paradigm to chest radiograph interpretation, incorporating additional strategies such as temporal context modeling, structured knowledge integration, and prompt tuning. Despite their potential, the real-world performance of these models—particularly across diverse populations, clinical sites, and diagnostic categories—remains insufficiently characterized.

Prior evaluations have largely been limited to U.S.-based or single-institution datasets, with little attention paid to performance on underrepresented cohorts, such as pediatric patients or international populations. In addition, the impact of key architectural differences—such as aspect-based visual grounding (e.g., MAVL [23]) or pseudo-prompt learning (e.g., PsPG [25])—on classification robustness across common and rare findings is not well understood.

To address these gaps, we conducted a large-scale, multinational benchmarking study of eight chest X-ray diagnostic models, including five recent foundation models and three traditional CNN-based architectures. We systematically evaluated model performance across 37 standardized classification tasks using six public datasets from the USA, Spain, Vietnam, and India, and three previously unseen, multi-center private datasets from four hospitals in China. This study is, to our knowledge, the most comprehensive head-to-head evaluation of chest X-ray AI models to date, offering insights into diagnostic accuracy, generalizability, and robustness across heterogeneous imaging domains and clinical populations.

Results

Overall Model Performance on Public Datasets

We evaluated and compared eight recent chest X-ray diagnostic models (Table 1), which can be categorized into two groups based on their learning paradigms: Traditional Supervised Learning Models and Foundation Models. Foundation Models leverage advanced vision-language pretraining techniques for multimodal learning, including:

- **CheXzero** [21]: Built on CLIP, using contrastive learning between images and reports;
- **BioViL-T** [22]: An extension of CLIP with temporal modeling capabilities;
- **MAVL** [23]: Combines contrastive and supervised learning with knowledge-enhanced mechanisms;
- **MedKLIP** [24]: Incorporates contrastive and supervised learning to enhance concept grounding;
- **PsPG** [25]: A hybrid CLIP-CoOp model featuring a prompt decoder, spatial fusion, and pairwise co-occurrence encoding.

By contrast, traditional supervised models rely solely on CNNs trained with labeled radiographs. These include **DenseNet**, **ResNet** [14], and **X-Raydar** [15], a multi-scale CNN architecture.

All eight models were benchmarked on six publicly available datasets from the USA, India, Vietnam, and Spain—CheXpert [17], NIH (Google) [26], OpenI [27], VinDr-CXR [19], PadChest [18], and MIDRC [28] (Table 2). Performance was assessed across 37 standardized classification tasks spanning pulmonary, cardiovascular, skeletal, pleural, and device-related findings. Two complementary metrics quantified diagnostic accuracy: AUROC, reflecting overall discriminative ability, and AUPRC, emphasizing positive case detection under class imbalance.

We first examined the number of tasks for which each model achieved the highest combined AUROC and AUPRC (Figure 1). The foundation model MAVL ranked first in 14 tasks—the most among all models—followed by BioViL-T (8 tasks), CheXzero (5), ResNet (4), DenseNet (3), MedKLIP (3), and PsPG (1). Notably, the top three performers—MAVL, BioViL-T, and CheXzero—were all foundation models.

Next, we analyzed total and mean AUROC/AUPRC values across all classification tasks for which each model produced predictions (Figure 2). MAVL, evaluated on 24 tasks, again achieved the highest performance with a mean AUROC of 0.82 ± 0.13 and AUPRC of 0.32 ± 0.27 . MedKLIP, evaluated on the same subset of tasks, performed comparably (AUROC: 0.81 ± 0.13 ; AUPRC: 0.30 ± 0.27), reinforcing its robustness.

Other foundation models—BioViL-T, CheXzero, and PsPG—were evaluated on all 37 tasks but demonstrated lower mean performance (AUROC: 0.65–0.66; AUPRC: 0.14–0.18). This performance drop was driven largely by poor results on rare or ambiguously labeled tasks (e.g., Flattened Diaphragm, Hemidiaphragm Elevation, Hilar Enlargement), where AUROCs neared 0.50 and AUPRCs fell below 0.09 (Supplementary Note 1). This highlights a trade-off: while broader task coverage increases flexibility, it may compromise performance on low-prevalence findings.

In contrast to foundation models with broader task coverage, traditional CNN-based models like DenseNet and ResNet were each evaluated on 17 tasks. DenseNet achieved a mean AUROC of 0.82 ± 0.09 and an AUPRC of 0.30 ± 0.26 , while ResNet yielded 0.78 ± 0.12 and 0.27 ± 0.19 , respectively—both slightly lower than those of MAVL. X-Raydar, a multi-scale CNN architecture, evaluated on 16 tasks, underperformed across the board (AUROC: 0.49 ± 0.06 ; AUPRC: 0.11 ± 0.13).

In summary, foundation models—especially MAVL—not only delivered top overall performance but also demonstrated strong consistency across clinically meaningful tasks. Their success reflects the advantages of combining large-scale multimodal pretraining with focused diagnostic task design, achieving a balance between broad applicability and reliable, high-quality decision-making in real-world settings.

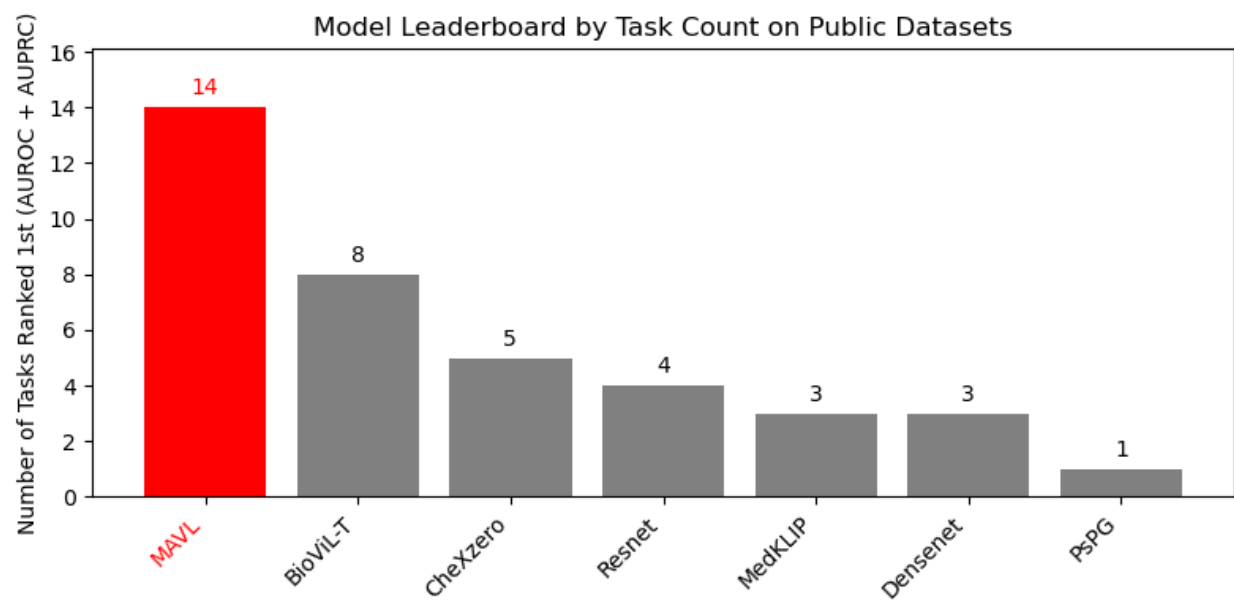


Figure 1. Number of public tasks in which each model ranked first based on the sum of AUROC and AUPRC. Models achieving the highest number of top rankings are highlighted in red.

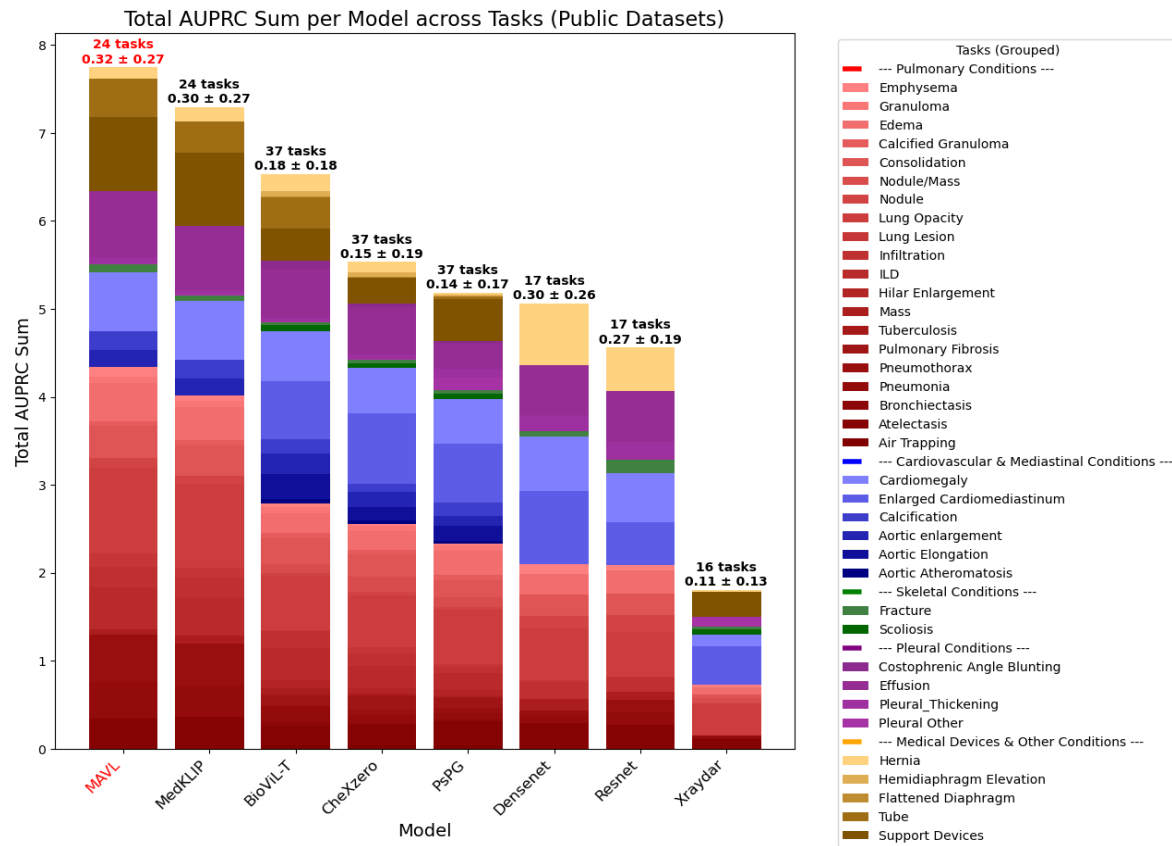
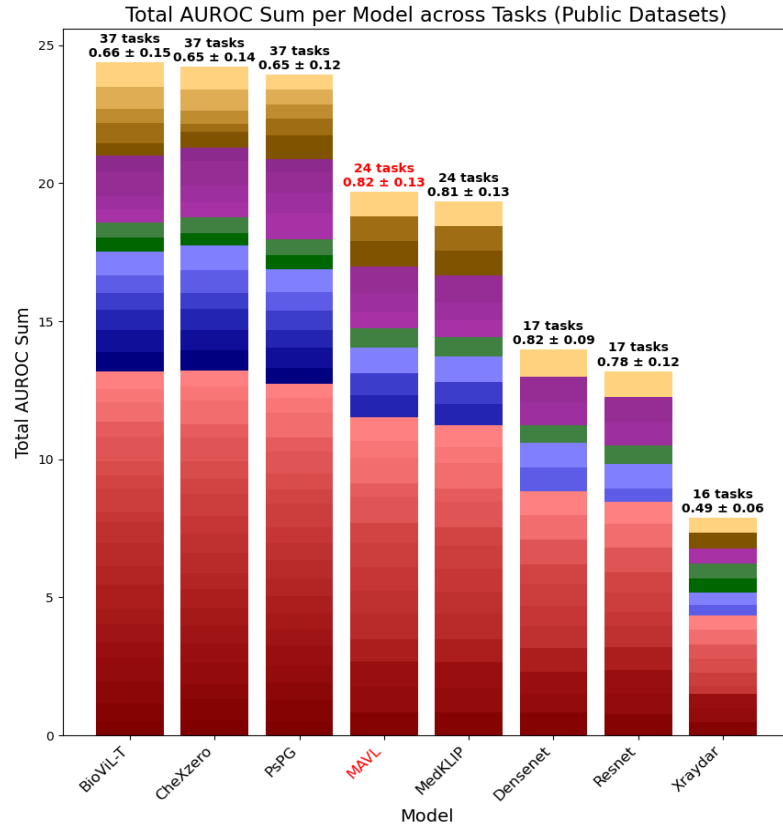


Figure 2. Total and Mean AUROC / AUPRC Across Tasks for Each Model (Public Datasets). Each bar represents the cumulative AUROC or AUPRC across all evaluated public tasks, with contributions stacked by clinical category. The text above each bar indicates the mean \pm standard deviation across tasks. The model with the highest mean score across tasks—prioritized over others by task coverage in the event of a tie—is highlighted in red.

Model Performance on Shared Diagnostic Tasks on Public Dataset

To enable a fair head-to-head comparison, we analyzed a subset of 11 shared diagnostic tasks that all eight models were capable of predicting. As shown in Figure 3 (top), MAVL dominated the leaderboard, ranking first in 7 out of 11 tasks based on the combined AUROC and AUPRC—far ahead of all other models. MedKLIP followed with two first-place finishes, while DenseNet and ResNet each led in one.

Figure 3 (bottom) further confirms MAVL’s robustness, achieving the highest average AUROC (0.88 ± 0.08) and AUPRC (0.39 ± 0.27) across the shared tasks. MedKLIP ranked a close second (AUROC: 0.87 ± 0.10 ; AUPRC: 0.36 ± 0.26). In contrast, traditional CNN models (DenseNet and ResNet) showed moderately strong AUROCs (0.81 and 0.78 , respectively) but lower AUPRCs (0.28). Other foundation models like CheXzero, PsPG, and BioViL-T, though more broadly applicable in task coverage, lagged behind in mean AUROC (0.70 - 0.75) and AUPRC (0.22 - 0.24). The traditional model X-Raydar ranked last overall, with a mean AUROC of 0.49 and AUPRC of 0.09 .

To better visualize per-task variation, we plotted each model’s AUROC and AUPRC across the 11 shared tasks using radar plots (Figure 4). MAVL and MedKLIP outperform and match top performance on most of the tasks for both AUROC and AUPRC, with particularly strong results on Pneumothorax, Pneumonia, Consolidation, Edema, Lung Lesion, and Lung Opacity—key pulmonary findings in clinical triage. Traditional models such as DenseNet and ResNet performed best on Hernia and Fracture in the AUPRC radar plots but lagged behind on most other tasks.

Together, these shared-task analyses reinforce the superior and consistent performance of foundation models—especially MAVL—across both balanced and imbalanced classification tasks.

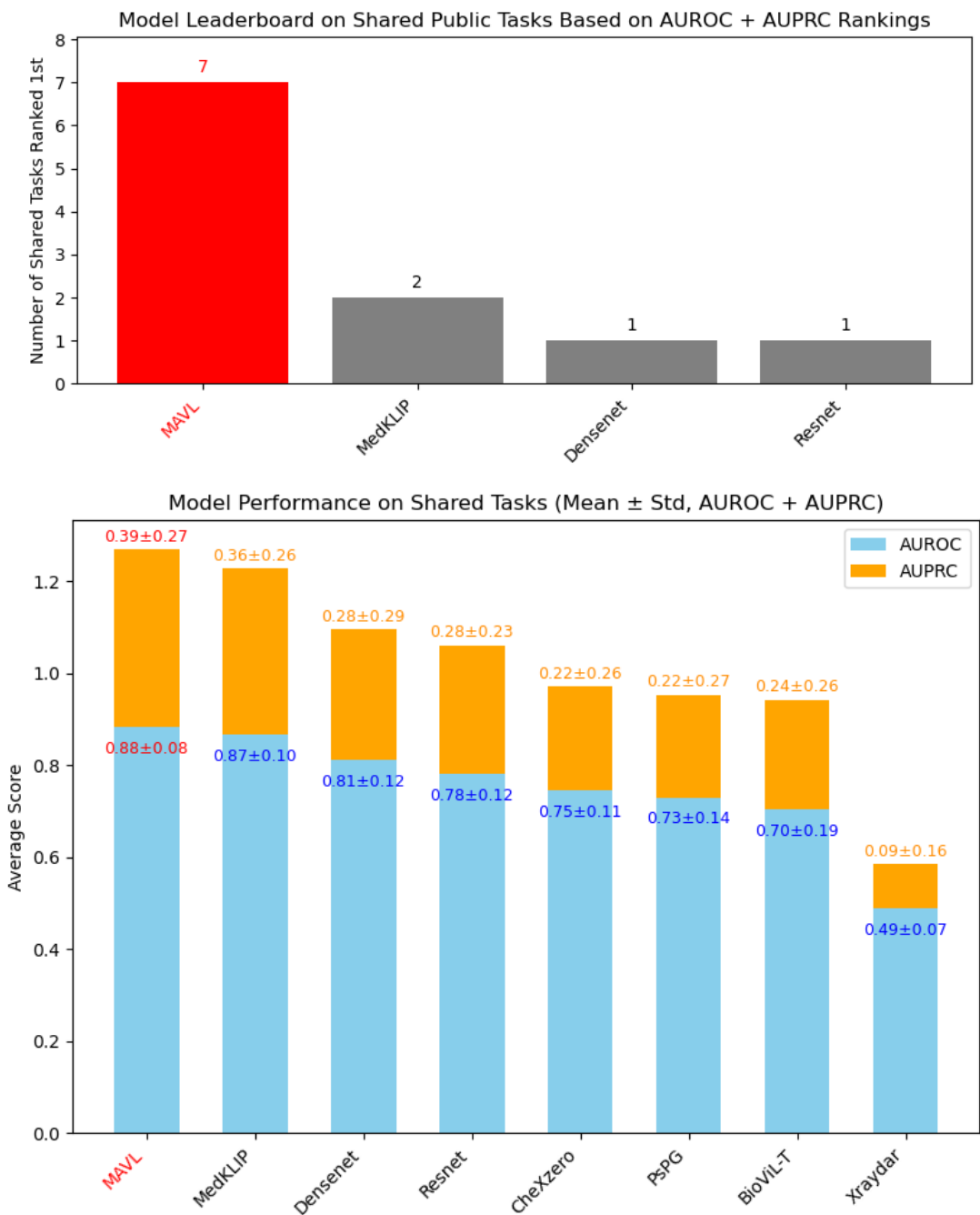
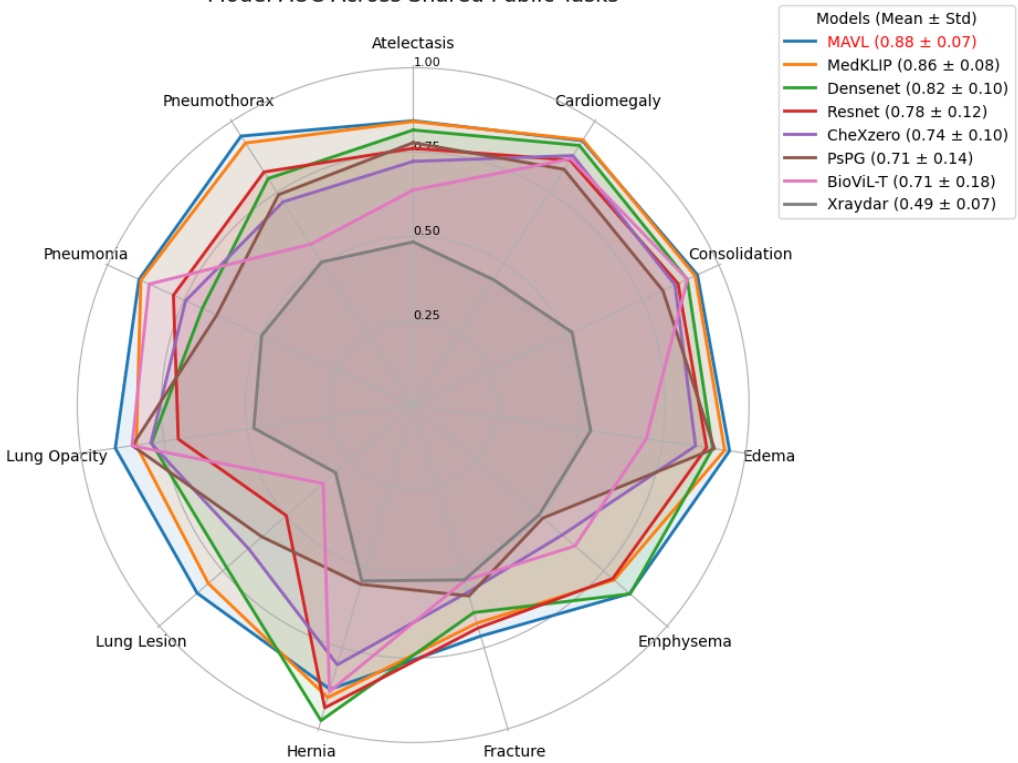


Figure 3. Benchmarking Model Performance on 11 Shared Public Tasks. Top: Number of tasks where each model ranked first based on combined AUROC and AUPRC. Bottom: Mean AUROC and AUPRC (\pm SD) across the 11 shared tasks for each model. The top-performing model, based on the highest combined average AUROC and AUPRC, is highlighted in red.

Model AUC Across Shared Public Tasks



Model PR AUC Across Shared Public Tasks

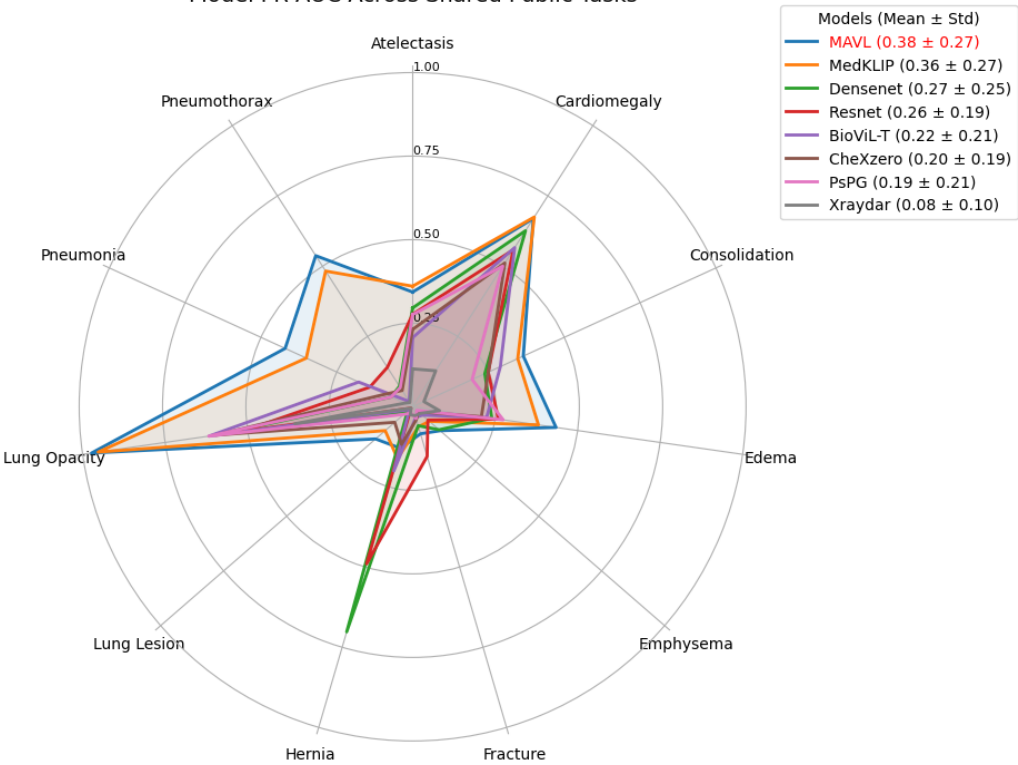


Figure 4. Radar plot of AUROC and AUPRC across 11 shared public tasks predicted by all models. Each axis represents one diagnostic task, and each curve represents a model's average AUROC or AUPRC across public datasets. Shaded areas indicate performance variability. The legend lists each model's mean score \pm standard deviation (SD) across all included tasks. The top-performing model in the legend is highlighted in red.

Model Generalizability on Private Datasets Across Tasks and Populations

To assess model generalizability in clinically realistic settings, we evaluated all models on four diagnostic tasks—Pneumothorax, Pneumonia, Effusion, and Fracture—using three novel private datasets collected from four hospitals in China (Table 2).

Overall, the foundation model MAVL achieved the highest average performance across tasks (AUROC: 0.95 ± 0.05 ; AUPRC: 0.89 ± 0.04), followed by MedKLIP (AUROC: 0.94 ± 0.06 ; AUPRC: 0.86 ± 0.06) (Figure 5). In contrast, other foundation models with broader pretraining objectives—CheXzero (AUROC: 0.77 ± 0.13 ; AUPRC: 0.53 ± 0.15), BioViL-T (AUROC: 0.72 ± 0.12 ; AUPRC: 0.46 ± 0.10), and PsPG (AUROC: 0.64 ± 0.14 ; AUPRC: 0.43 ± 0.02)—demonstrated only moderate performance.

Despite being a traditional CNN model, ResNet ranked third overall (AUROC: 0.91 ± 0.04 ; AUPRC: 0.71 ± 0.19), although the higher variability in AUPRC suggests reduced consistency across tasks. DenseNet followed (AUROC: 0.84 ± 0.15 ; AUPRC: 0.61 ± 0.15), with a similar trend. X-Raydar showed the lowest performance (AUROC: 0.36 ± 0.10 ; AUPRC: 0.16 ± 0.09), indicating poor generalizability.

At the task level (Figure 6), MAVL consistently outperformed other models in adult cohorts, ranking first in three of four tasks: Pneumothorax (AUROC: 0.98, AUPRC: 0.90), Pneumonia (AUROC: 0.95, AUPRC: 0.88), and Fracture (AUROC: 0.97, AUPRC: 0.86). MedKLIP ranked second overall and achieved top performance in Effusion detection (AUROC: 0.97, AUPRC: 0.95).

Crucially, all models were trained exclusively on adult chest radiographs. When evaluated on the pediatric pneumonia cohort (Nanjing_pediatric dataset), the average

AUROC across all models dropped substantially—from 0.81 ± 0.18 in adults to 0.57 ± 0.29 in children (Figure 7, top panel). Even MAVL, the top-performing model, showed a decrease in AUROC from 0.95 to 0.81. Given the limited number of models ($n = 8$) and the unequal variances between groups, we employed a non-parametric bootstrap approach (10,000 iterations) to more robustly assess the significance of this performance decline. The resulting 95% confidence interval for the mean AUROC difference (adult – pediatric) was [0.034, 0.462], with a bootstrap p-value of 0.0202—indicating a statistically significant reduction in diagnostic performance when models were applied to pediatric cases (Figure 7, bottom panel). These findings underscore a critical challenge in achieving robust cross-population generalization.

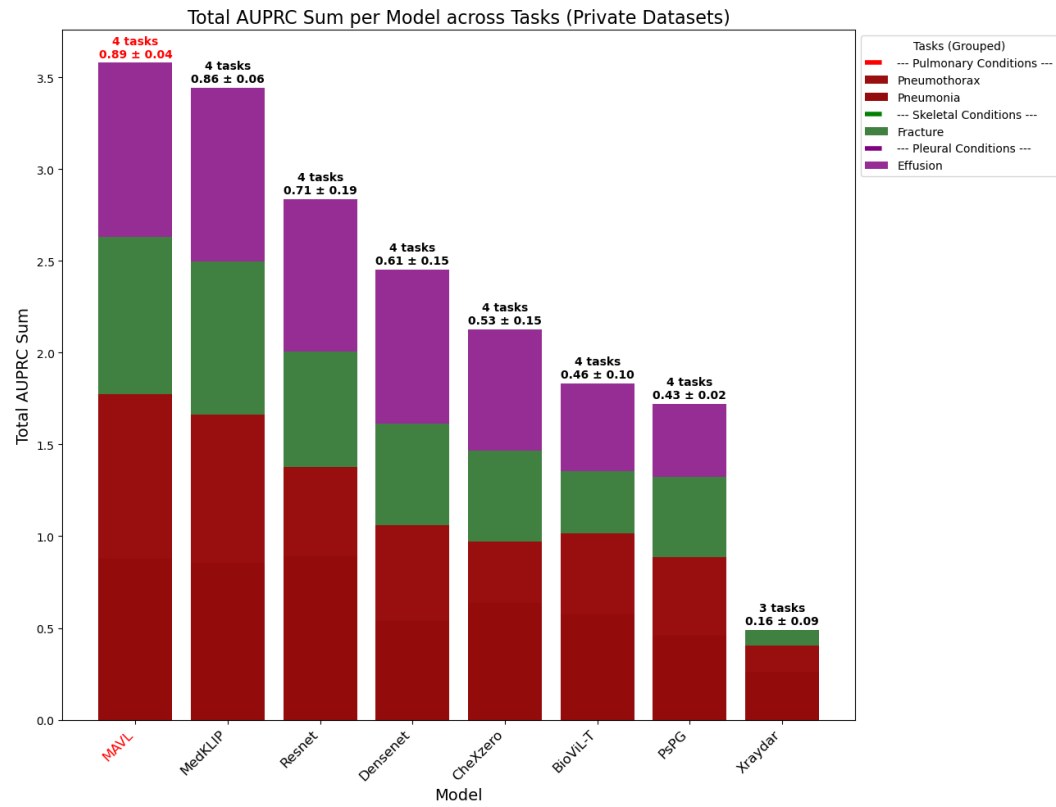
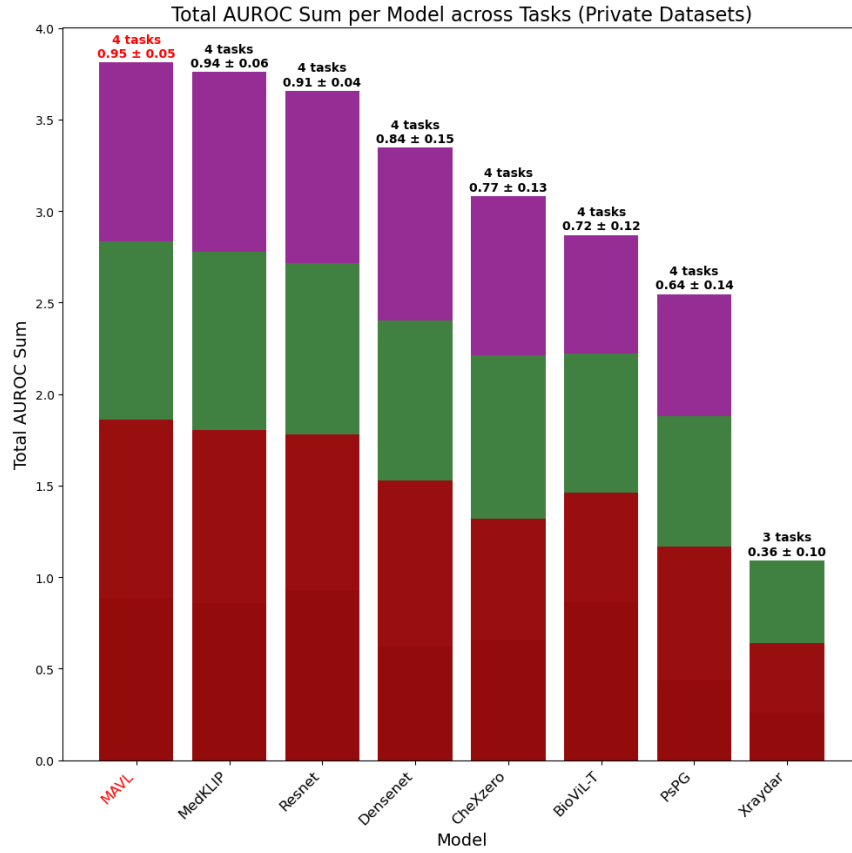


Figure 5. Total and Mean AUROC/AUPRC Across Tasks per Model (Private Datasets).
Each bar height reflects the total AUROC sum; the text above each bar denotes mean \pm standard deviation across tasks.

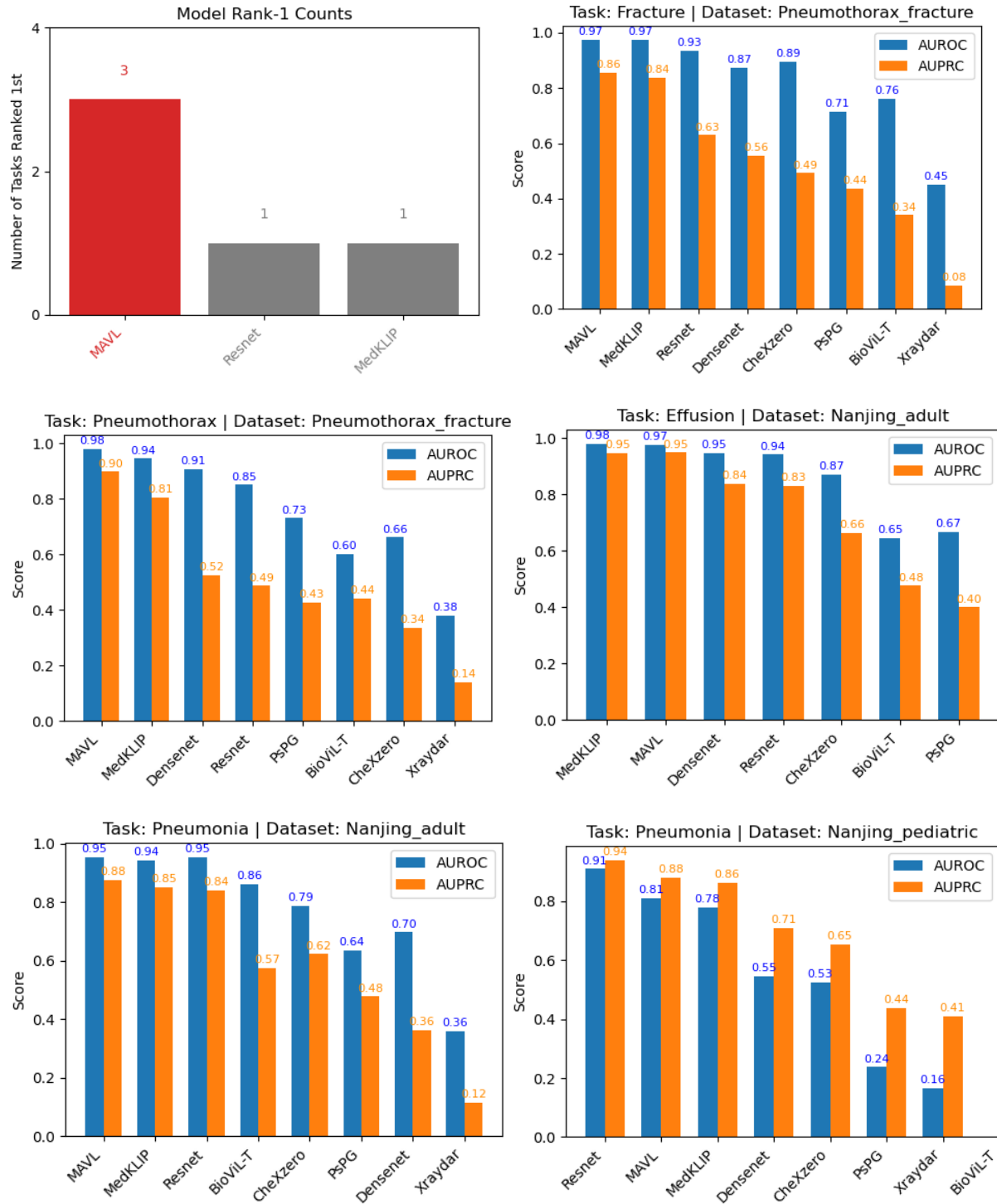


Figure 6. Performance Comparison of Eight Models on Private Datasets Across Four Diagnostic Tasks. Bar plots compare the performance of eight chest X-ray diagnostic models (MAVL, MedKLIP, ResNet, DenseNet, CheXzero, BioViL-T, PsPG, and X-Raydar) on four tasks—Fracture and Pneumothorax (Pneumothorax_Fracture dataset), and Pneumonia and Effusion (Nanjing Adult and Pediatric datasets). Top left: Number of tasks where each model

ranked first based on combined AUROC and AUPRC. Other panels: Task-specific AUROC (blue) and AUPRC (orange) for each model.

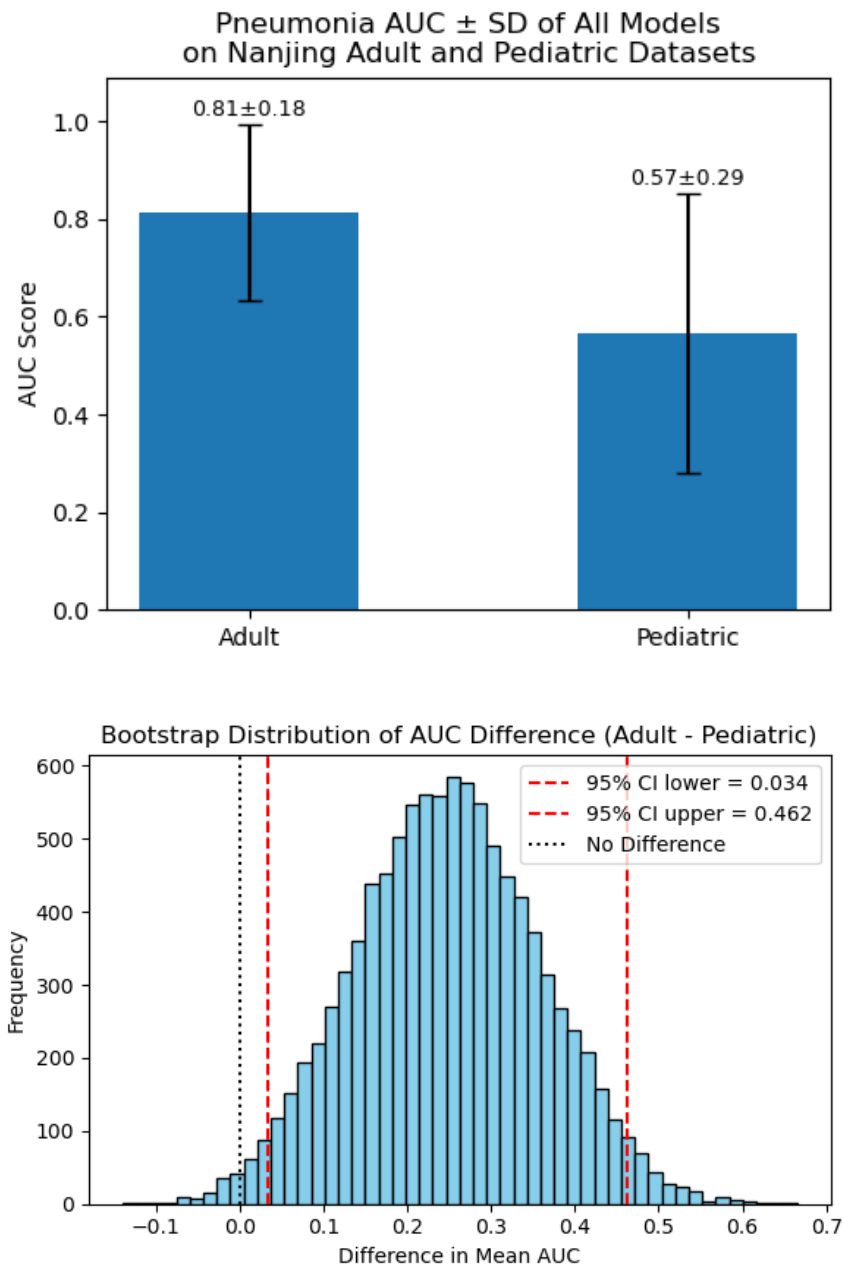


Figure 7. Comparative Model Performance on Nanjing Adult and Pediatric Chest X-rays. Bar plot (top) shows mean AUROC \pm standard deviation for pneumonia classification across all models, tested separately on adult and pediatric chest radiographs. Bootstrap analysis (bottom) was used to evaluate the statistical significance of the observed performance drop in pediatric cases. A total of 10,000 bootstrap samples were drawn to estimate the 95% confidence interval

for the mean AUROC difference (adult – pediatric), which did not include zero (CI = [0.034, 0.462]; $p = 0.0202$), indicating a statistically significant reduction in performance.

Discussion

This benchmarking study comprehensively evaluated eight chest X-ray diagnostic models—five foundation models and three traditional CNN architectures—across six public and three private datasets encompassing 37 classification tasks. Among them, the foundation model MAVL consistently achieved the highest and most stable diagnostic performance across both public (mean AUROC: 0.82; AUPRC: 0.32) and private (mean AUROC: 0.95; AUPRC: 0.89) datasets. These results underscore the advantage of vision-language foundation models—particularly those equipped with structured supervision and multi-aspect grounding—in enhancing model generalizability and robustness across diverse imaging domains.

MAVL, developed by Phan et al. [23], integrates contrastive vision-language pretraining, supervised fine-tuning, and knowledge-enhanced prompt generation to improve visual-semantic alignment in medical imaging. Specifically, MAVL's pretraining strategy decomposes complex disease entities into interpretable sub-aspects—such as opacity, shape, anatomical location, and texture—and grounds these in structured textual prompts derived from medical knowledge bases and GPT-generated disease descriptions. This multi-aspect grounding mechanism enables MAVL to more precisely localize and classify subtle radiographic patterns than CLIP-like architectures that rely solely on global image-text contrastive learning. In our benchmark, this design translated into top-ranked performance in 14 out of 37 public classification tasks, and leading AUROC and AUPRC values across 11 shared tasks—especially for high-clinical-salience findings like Pneumothorax, Pneumonia, Edema, and Lung Opacity.

On private datasets collected from multiple hospitals in China, MAVL further demonstrated strong generalizability (AUROC: 0.95 ± 0.05 ; AUPRC: 0.89 ± 0.04), outperforming all other models in three of four tasks. Compared with other foundation

models (e.g., CheXzero, BioViL-T), MAVL’s architecture appears better suited for real-world deployment due to its superior performance on common but heterogeneous pathologies. Its dual pretraining/fine-tuning framework likely contributes to its robustness across different imaging sources and label distributions.

Despite these strengths, MAVL's current open-source implementation has notable limitations. Its “disease dictionary” is fixed to 24 predefined labels, which restricts its flexibility in broader clinical settings. Furthermore, like all models evaluated, MAVL exhibited a performance drop when applied to pediatric cohorts—its AUROC decreased from 0.95 in adults to 0.81 in children—highlighting the need for population-specific adaptation. Future work should explore expanding its label vocabulary, incorporating cross-population fine-tuning strategies, and integrating uncertainty quantification to improve interpretability and reliability in real-world clinical deployment.

While MedKLIP [24] and MAVL share a common objective—enhancing vision-language alignment through medical knowledge and structured supervision—their performance diverged in our benchmark: MedKLIP ranked first in only 3 public tasks and 1 private task. This discrepancy may be attributed to fundamental differences in their text representation strategies. MedKLIP encodes each disease as a full-sentence clinical description derived from knowledge bases, which can introduce semantic noise and may not align well with subtle radiographic cues. By contrast, MAVL’s use of modular, aspect-based prompts provides more targeted visual grounding, potentially supporting more accurate classification across a broader range of findings.

BioViL-T [22] was one of only three models capable of completing all 37 public classification tasks (alongside CheXzero and PsPG). Although originally designed to capture temporal context in longitudinal chest radiographs, BioViL-T also demonstrated moderate yet stable performance in static image classification, with an overall AUROC of 0.66 ± 0.15 on public datasets and 0.72 ± 0.12 on private datasets. These results suggest that BioViL-T’s strengths lie in its broad task coverage and generalizability rather than peak diagnostic accuracy. Its cross-task adaptability and zero-shot capabilities remain valuable for scalable deployment. However, its relatively lower

performance in high-clinical-relevance tasks indicates that temporal modeling alone may be insufficient for optimal transferability without the support of structured supervision or domain-specific adaptation strategies.

CheXzero [21] and PsPG [25] were the two other models capable of performing all 37 public classification tasks. Both are CLIP-based vision-language foundation models designed for chest radiograph interpretation. CheXzero leverages contrastive learning between chest X-ray images and unstructured radiology reports to support true zero-shot multi-label classification across a broad label space. However, on public datasets, its overall diagnostic performance was modest, with a mean AUROC of 0.65 ± 0.14 . This suggests that while CheXzero offers broad task coverage, it lacks the visual precision required to excel in fine-grained classification benchmarks. On private datasets, its performance was moderate (mean AUROC: 0.77), but it failed to rank among the top models. Notably, its AUROC dropped from 0.79 in adult pneumonia to 0.53 in pediatric pneumonia, indicating limited adaptability to anatomical variation and image scaling. This may stem from its ViT-B/32 backbone, which employs a 32×32 patch size and 224×224 input resolution—compromising spatial granularity and reducing sensitivity to subtle findings such as pneumothorax or effusion. These observations highlight a key trade-off in CheXzero’s design: broad zero-shot generalizability comes at the cost of fine-detail recognition.

PsPG similarly supports zero-shot classification across all 37 tasks but adopts an alternative strategy by replacing natural language prompts with automatically generated pseudo-prompts. While this design is computationally efficient, PsPG achieved only limited diagnostic performance on both public (mean AUROC: 0.52) and private (mean AUROC: 0.64) datasets. The lack of explicit semantic guidance may hinder its ability to generalize across diverse clinical findings. These results highlight the importance of developing more expressive and context-aware prompt mechanisms to support robust zero-shot medical image understanding.

In contrast, traditional CNN models such as DenseNet and ResNet [14]—though trained on large-scale labeled chest radiographs—were limited to predicting only 17 fixed

classification tasks. To ensure a fair comparison, we evaluated performance across the 11 tasks supported by all models. On these shared tasks, DenseNet (AUROC: 0.81; AUPRC: 0.28) and ResNet (AUROC: 0.78; AUPRC: 0.28) demonstrated lower overall performance and reduced sensitivity to positive cases compared to foundation models such as MAVL (AUROC: 0.88; AUPRC: 0.39) and MedKLIP (AUROC: 0.87; AUPRC: 0.36). A similar performance gap was observed on private datasets, where both DenseNet and ResNet continued to underperform relative to foundation models, indicating limitations in diagnostic capability and generalizability. While ResNet underperformed compared to foundation models in overall performance, it notably achieved the highest AUROC in both adult (0.95) and pediatric (0.91) pneumonia classification tasks, suggesting that its residual architecture may confer added robustness in certain settings, particularly under domain shift.

X-Raydar [15], a CNN architecture trained on curated UK datasets, consistently ranked last, demonstrating poor transferability to international data (AUROC: 0.49 ± 0.06 ; AUPRC: 0.11 ± 0.13 on public datasets; AUROC: 0.36 ± 0.10 on private datasets). These findings reinforce the vulnerability of fully supervised models to overfitting on narrow source distributions and highlight the limitations of unimodal feature learning in capturing diverse radiographic presentations.

This study has several limitations. First, MAVL's current open-source implementation supports only 24 predefined disease labels, restricting its adaptability to broader or evolving clinical vocabularies. Second, all evaluated models—including MAVL—showed reduced diagnostic accuracy in pediatric populations, highlighting the need for age-specific adaptation. Third, although the inclusion of private datasets enhanced real-world applicability, most of these data originated from China, which may limit the generalizability of model performance across different healthcare systems and patient demographics. To address these limitations, we are actively expanding our benchmarking efforts. In addition to the current datasets from China, the USA, India, Vietnam, and Spain, we are incorporating newly acquired chest X-ray datasets from Germany, Turkey, and Japan to enable broader geographic and population coverage. These additions will support more rigorous cross-national validation and help ensure

that AI models perform equitably across underrepresented regions. Moreover, future work will explore model ensemble strategies—such as late fusion or confidence-aware integration—to combine the complementary strengths of different architectures and further improve diagnostic robustness in heterogeneous clinical settings.

In conclusion, foundation models that incorporate structured medical knowledge and multi-aspect visual grounding—particularly MAVL—demonstrate clear advantages over traditional CNNs in diagnostic performance and generalizability across multinational chest X-ray datasets. These findings underscore the potential of clinically guided vision-language models to support scalable, adaptable, and high-fidelity diagnostic tools in real-world healthcare systems.

Methods

Datasets

We tested and compared the models using 9 datasets from the USA, India, Vietnam, Spain, and China. Six of these are publicly available datasets, while six are private datasets. For more details, please refer to Table 1.

Public Dataset

CheXpert [17] comprises 224,316 chest radiographs from 65,240 patients. These images were retrospectively collected from Stanford Hospital (including both inpatient and outpatient centers) between October 2002 and July 2017, along with their corresponding radiology reports. Each report is annotated for 14 observations, classified as positive (1), negative (0), or uncertain (-1), with unmentioned observations left blank. The test set includes 500 studies from 500 patients, each independently annotated by eight board-certified radiologists. These annotations are binarized into negative (0) and positive (1) labels. In this study, we use labels marked as 0 (negative) and 1 (positive) for training and evaluating the model, excluding all cases with other labels.

MIDRC [28] includes COVID-19-related chest X-ray images from South Korea, India, and the USA. In this study, we selected two cohorts to evaluate our model's performance: Cohort mRALE Score ≥ 1 : This cohort contains 1,650 chest X-ray images. All images have mRALE scores [29] of at least 1, indicating that all patients exhibit pulmonary edema. Cohort mRALE Score 0: This cohort includes 400 chest X-ray images with mRALE scores of 0, indicating no signs of pulmonary edema. We used this dataset to evaluate the model's performance in predicting pulmonary edema, with Cohort mRALE Score ≥ 1 serving as the positive dataset and Cohort mRALE Score 0 as the negative dataset.

NIH Google [26] includes 1,818 test images from the DS1 public dataset, sourced from multiple hospital networks across the United States, and 2,412 validation images from the ChestX-ray14 public dataset. These images are annotated with five radiologist-adjudicated labels. In our study, we used these 4,376 images for model evaluation.

Openi [27] OpenI contains 8,121 chest X-ray images from 3,996 patients sourced from the Indiana Network for Patient Care in the United States. The dataset includes 18 key findings extracted from the radiology reports. In this study, we utilized the entire dataset for model evaluation.

PadChest [18] comprises over 160,000 images from 67,000 patients, interpreted and reported by radiologists at Hospital San Juan (Spain) between 2009 and 2017. The reports are annotated with 174 distinct radiographic findings and 19 differential diagnoses, organized into a hierarchical taxonomy, and mapped to standard Unified Medical Language System (UMLS) terminology. Of these reports, 27% were manually annotated by trained physicians, while the remaining annotations were generated using a supervised method based on a recurrent neural network (RNN) with attention mechanisms. Since the dataset does not include a predefined split into training and test sets, we used the entire dataset for model evaluation.

VinDr-CXR [19] comprises 18,000 postero-anterior (PA) chest X-ray scans collected from Hospital 108 and Hanoi Medical University Hospital in Vietnam. The dataset is divided into a training set of 15,000 scans and a test set of 3,000 scans. Each training image was independently annotated by three radiologists, whereas test images underwent a more rigorous process, with annotations derived from the consensus of five radiologists. The annotations include 22 critical findings (local labels) and 6 diagnoses (global labels). In our study, we utilized the test set for model evaluation.

Private Dataset

Nanjing Adult Dataset includes patients aged 18 to 88 years from Juxian Hospital, Huaian Hospital, Qixia Hospital, and Qidu Hospital in Nanjing, China. It comprises 3,470 chest X-rays categorized into five diagnostic labels: normal (n=1,115), pneumonia (n=183), and effusion (n=112).

Pneumothorax_fracture Dataset includes patients aged 18 to 88 years from Juxian Hospital, Huaian Hospital, Qixia Hospital, and Qidu Hospital in Nanjing, China. It comprises 1,074 chest X-rays categorized into three diagnostic labels: normal (n=9,16), pneumothorax (n=69), and fracture (n=89).

Models

We tested and compared three categories comprising a total of 8 models (Table 2):

(a) Foundation Models: This category includes models that leverage advanced pre-training techniques for multimodal learning. Specifically, we evaluated: **CheXzero** [21]: Built on Contrastive Language-Image Pre-Training (CLIP); **BioViL-T** [22]: Utilizing Temporal CLIP for temporal modeling; **MAVL** [23]: Combining contrastive and supervised learning with knowledge-enhanced mechanisms; **MedKLIP** [24]: Incorporating contrastive and supervised learning for knowledge-enhanced performance; **PsPG** [25]: A hybrid model integrating CLIP with CoOp (prompt learning methods), including a Prompt Decoder, Spatial Fusion, and Soft Pairwise Co-occurrence.

(b) Traditional Supervised Learning Models: These are conventional models based on Convolutional Neural Networks (CNNs), including **DenseNet** [14]; **ResNet** [14]; and **X-Raydar** [15] (a multi-scale CNN architecture).

Model Evaluation Workflow

Data Loading and Preprocessing

To ensure consistent input representations across all models, we first standardized the chest X-ray images by normalizing their intensity values to the range $[-1024, 1024]$, following the same processing steps with the TorchXRyVision package. Each image was then reformatted into a single-channel tensor of size $[1, H, W]$. Subsequently, model-specific preprocessing steps were applied as required, such as resizing to predefined dimensions, performing center cropping to focus on the most informative regions, and converting intensity values into alternative ranges (e.g., $[0, 255]$) as dictated by the model's design. These preprocessing adjustments are crucial for achieving optimal inference performance, given that different models may be sensitive to variations in data preparation steps.

Evaluating Metric

We used the following evaluation metrics to assess the diagnostic performance of different models on various datasets for detecting abnormalities in chest X-rays: ROC-AUC: Measures the overall ability of the model to distinguish between classes; PR-AUC (Precision-Recall AUC): Focuses on the performance for the positive class, especially useful for imbalanced datasets; Sensitivity (Recall): Evaluates the model's ability to correctly identify positive cases; Specificity:

$$\text{Specificity} = \frac{\text{True Negatives (TN)}}{\text{True Negatives (TN)} + \text{False Positives (FP)}}$$

Assesses the model's ability to correctly identify negative cases; Balanced Accuracy:

$$\text{Balanced Accuracy} = \frac{\text{Sensitivity} + \text{Specificity}}{2}$$

Provides a balanced assessment by averaging sensitivity and specificity, reducing the impact of class imbalance; Accuracy:

$$\text{Accuracy} = \frac{\text{True Positives (TP)} + \text{True Negatives (TN)}}{\text{Total Number of Samples}}$$

Calculates the overall proportion of correct predictions; Precision:

$$\text{Precision} = \frac{\text{True Positives (TP)}}{\text{True Positives (TP)} + \text{False Positives (FP)}}$$

Measures the proportion of true positives among all predicted positives; F1 Score:

$$\text{F1 Score} = 2 \cdot \frac{\text{Precision} \cdot \text{Recall}}{\text{Precision} + \text{Recall}}$$

Balances precision and recall, providing a single metric for imbalanced datasets.

To compare the average performance of models for each prediction task across different datasets, we identified a subset of ten tasks that all models were capable of predicting. For this unified task subset, we calculated each model's average AUC, average sensitivity, and average balanced accuracy for each prediction task across different datasets. We visualized these results using radar charts.

Table 1. Overview of Recent Chest X-ray Diagnostic Models

| Model Name | Year | Model Type | Training Datasets | Evaluation Datasets | Prediction Tasks |
|-------------------------|------|--|--|--|------------------|
| Foundation Model | | | | | |
| CheXzero | 2022 | CLIP (Contrastive Language-Image Pre-Training) | MIMIC-CXR | CheXpert, PadChest | Zero-short [30] |
| BioViL-T | 2023 | Temporal CLIP | MIMIC-CXR v2, Chest ImaGenome | MS-CXR-T (released dataset, for temporal tasks) | Zero-short |
| MAVL | 2024 | Contrastive + Supervised Learning (Knowledge-Enhanced) | MIMIC-CXR v2 (pre-training), ChestX-ray14, CheXpert, PadChest, RNSA, SIIM, COVIDx, | ChestX-ray14, CheXpert, PadChest, RNSA, SIIM, COVIDx | Zero-short |
| MedKLIP | 2023 | Contrastive + Supervised Learning (Knowledge-Enhanced) | MIMIC-CXR v2 | ChestX-ray14, RSNA Pneumonia, SIIM-ACR Pneumothorax, COVIDx CXR-2 and COVID Rural, Edema Severity (from MIMIC-XCR) | Zero-short |
| PsPG | 2024 | CLIP + CoOp (prompt learning methods) + Prompt Decoder, Spatial fusion, Soft pairwise co-occurrence | MIMIC-CXR, CheXpert | CheXpert-test, PadChest, VinDr-CXR, and Private-CXR | Zero-short |

Traditional CNN-based Model

| | | | | | |
|----------|------|-------------------------------|---|--|---------------------|
| DenseNet | 2021 | DenseNet (CNN) | NIH, RSNA, NIH Google, PadChest, CheXpert, MIMIC, OpenI, NLMTB, SIIM, VinBrain, ObjectCXR | NIH, RSNA, NIH Google, PadChest, CheX, MIMIC, OpenI, NLMTB, SIIM, VinBrain, ObjectCXR | 18 medical findings |
| X-Raydar | 2023 | Multi-scale InceptionV3 (CNN) | NHS Britain dataset (2,513,546 chest X-ray studies taken from 13 years) | 1. consensus set sampled from all 6 hospitals, 2. NHS random sampled dataset, 3. MIMIC-CXR dataset | 45 medical findings |
| ResNet | 2021 | ResNet (CNN) | NIH, RSNA, NIH Google, PadChest, CheX, MIMIC, OpenI, NLMTB, SIIM, VinBrain, ObjectCXR | NIH, RSNA, NIH Google, PadChest, CheX, MIMIC, OpenI, NLMTB, SIIM, VinBrain, ObjectCXR | 18 medical findings |

Table 2. Overview of the Nine Datasets for Model Evaluation

| | CheXpert | MIDRC | NIH Google | OpenI | Pad Chest | VinDr- CXR | Pneumot horax_ fracture | Nanjing Adult | Nanjing Pediatic |
|------------------------------------|----------------------|----------------------------------|------------------------|---------------------|------------------------------|-------------------------------|-------------------------------|------------------|---------------------|
| Private or Public | Public | Public | Public | Public | Public | Public | Private | Private | Private |
| Geographic Region | Western USA | South Korea, India, USA | Northeast USA | USA | Spain | Vietna m | China | China | China |
| Images (Total/ Frontal) | 223,414 / 191,010 | 6,650/ 6,650 | 4,376 / 4,376 | 7,470 / 4,014 | 158,62 6 / 108,72 2 | 15,000 / 15,000 | 1,074 / 1,074 | 3,470 / 3,470 | 371 / 371 |
| Test Split | Test split, n=668 | NA | Test split, n=1,818 | NA | NA | Test split, n=3,00 0 | NA | NA | NA |

Labels available for each dataset

| | |
|----------------------|---|
| Air Trapping | X |
| Aortic Atheromatosis | X |

| | | | | | |
|--------------------------------|---|--|---|---|---|
| Aortic Elongation | | | X | | |
| Aortic Enlargement | | | | | X |
| Atelectasis | X | | X | X | X |
| Bronchiectasis | | | | X | |
| Bone Destruction | | | | | |
| Calcification | | | | | X |
| Calcified Granuloma | | | X | | |
| Cardiomegaly | X | | X | X | X |
| Consolidation | X | | | X | X |
| Costophrenic Angle Blunting | | | | X | |
| Chronic Bronchitis | | | | | |

| | | | | | | | |
|-------------------------------|---|---|---|---|---|---|---|
| Edema | X | X | | X | X | | |
| Effusion | X | | | X | X | X | X |
| Emphysema | | | | X | X | | |
| Enlarged Cardiomediastinum | X | | | | | | |
| Fibrosis | | | | X | X | | |
| Flattened Diaphragm | | | | | X | | |
| Fracture | X | | X | X | X | | X |
| Fibrotic Band | | | | | | | |
| Granuloma | | | | X | X | | |
| Ground Glass Opacity | | | | | | | |

| | | | | | |
|--|---|---|---|---|---|
| Hemidiaphragm Elevation | | | | X | |
| Hernia | | | X | X | |
| Hilar Enlargement | | | | X | |
| ILD | | | | | X |
| Infiltration | | | X | X | X |
| Incomplete Expansion of the Lung | | | | | |
| Lung Lesion | X | | X | | X |
| Lung Opacity | X | X | X | | X |
| Mass | | | X | X | |
| Nodule/Mass | | X | | | X |

Scoliosis

X

Spondylosis

Subcutaneous
Emphysema

Supportive Device

Tuberculosis

X

Healed Tuberculosis

Tube

X



Reference

- [1] Megat Ramli, P.N., Aizuddin, A.N., Ahmad, N., Abdul Hamid, Z. and Ismail, K.I., 2025. A Systematic Review: The Role of Artificial Intelligence in Lung Cancer Screening in Detecting Lung Nodules on Chest X-Rays. *Diagnostics*, 15(3), p.246.
- [2] Burgos, C., Mendez, L.M., Rodriguez, M.M., Martinez, A., Sanchez, P., Tovar, C., Naranjo Vanegas, M., Friedrich, G., Vásquez-Hoyos, P., Mesa-Rubio, M.L. and Triana-Rodriguez, G.A., 2025. What to Look for in Chest X-Rays of Pediatric Patients With COVID-19: Insights From a Colombian Cohort. *Pediatric Pulmonology*, 60(3), p.e27495.
- [3] Hyun, K., Kim, J.J., Im, K.S., Kim, Y.H. and Ryu, J.H., 2025. Prediction of ipsilateral and contralateral pneumothorax using a simple chest X-ray. *Journal of Thoracic Disease*, 17(2), p.898.
- [4] Xu, Q., Sun, Z., Li, X., Ye, C., Zhou, C., Zhang, L. and Lu, G., 2021. Advanced gastric cancer: CT radiomics prediction and early detection of downstaging with neoadjuvant chemotherapy. *European radiology*, 31(11), pp.8765-8774.
- [5] Huang, M., Xu, Q., Zhou, M., Li, X., Lv, W., Zhou, C., Wu, R., Zhou, Z., Chen, X., Huang, C. and Lu, G., 2023. Distinguishing multiple primary lung cancers from intrapulmonary metastasis using CT-based radiomics. *European Journal of Radiology*, 160, p.110671.
- [6] Xu, C., Xu, Q., Liu, L., Zhou, M., Xing, Z., Zhou, Z., Ren, D., Zhou, C., Zhang, L., Li, X. and Zhan, X., 2024. A tri-light warning system for hospitalized COVID-19 patients: Credibility-based risk stratification for future pandemic preparedness. *European Journal of Radiology Open*, 13, p.100603.
- [7] Zhan, X., Xu, Q., Zheng, Y., Lu, G. and Gevaert, O., 2025. Reliability-enhanced data cleaning in biomedical machine learning using inductive conformal prediction. *PLOS Computational Biology*, 21(2), p.e1012803.
- [8] Xu, Q., Zhan, X., Zhou, Z., Li, Y., Xie, P., Zhang, S., Li, X., Yu, Y., Zhou, C., Zhang, L. and Gevaert, O., 2021. AI-based analysis of CT images for rapid triage of COVID-19 patients. *NPJ digital medicine*, 4(1), p.75.

- [9] Sukhadia, S.S., Sadée, C., Gevaert, O. and Nagaraj, S.H., 2024. Machine Learning Enabled Prediction of Biologically Relevant Gene Expression Using CT-Based Radiomic Features in Non-Small Cell Lung Cancer. *Cancer Medicine*, 13(24), p.e70509.
- [10] Steyaert, S., Pizurica, M., Nagaraj, D., Khandelwal, P., Hernandez-Boussard, T., Gentles, A.J. and Gevaert, O., 2023. Multimodal data fusion for cancer biomarker discovery with deep learning. *Nature machine intelligence*, 5(4), pp.351-362.
- [11] Steyaert, S., Qiu, Y.L., Zheng, Y., Mukherjee, P., Vogel, H. and Gevaert, O., 2023. Multimodal deep learning to predict prognosis in adult and pediatric brain tumors. *Communications Medicine*, 3(1), p.44.
- [12] Carrillo-Perez, F., Pizurica, M., Marchal, K. and Gevaert, O., 2024. Synthetic multimodal data modelling for data imputation. *Nature Biomedical Engineering*, pp.1-5.
- [13] Cheerla, A. and Gevaert, O., 2019. Deep learning with multimodal representation for pancancer prognosis prediction. *Bioinformatics*, 35(14), pp.i446-i454.
- [14] Cohen, J.P., Viviano, J.D., Bertin, P., Morrison, P., Torabian, P., Guarrera, M., Lungren, M.P., Chaudhari, A., Brooks, R., Hashir, M. and Bertrand, H., 2022, December. TorchXRyVision: A library of chest X-ray datasets and models. In *International Conference on Medical Imaging with Deep Learning* (pp. 231-249). PMLR.
- [15] Cid, Y.D., Macpherson, M., Gervais-Andre, L., Zhu, Y., Franco, G., Santeramo, R., Lim, C., Selby, I., Muthuswamy, K., Amlani, A. and Hopewell, H., 2024. Development and validation of open-source deep neural networks for comprehensive chest x-ray reading: a retrospective, multicentre study. *The Lancet Digital Health*, 6(1), pp.e44-e57.
- [16] Huang, G., Liu, Z., Van Der Maaten, L. and Weinberger, K.Q., 2017. Densely connected convolutional networks. In *Proceedings of the IEEE conference on computer vision and pattern recognition* (pp. 4700-4708).
- [17] Irvin, J., Rajpurkar, P., Ko, M., Yu, Y., Ciurea-Ilicus, S., Chute, C., Marklund, H., Haghighi, B., Ball, R., Shpanskaya, K. and Seekins, J., 2019, July. Chexpert: A large chest radiograph dataset with uncertainty labels and expert comparison. In *Proceedings of the AAAI conference on artificial intelligence* (Vol. 33, No. 01, pp. 590-597).

- [18] Bustos, A., Pertusa, A., Salinas, J.M. and De La Iglesia-Vaya, M., 2020. Padchest: A large chest x-ray image dataset with multi-label annotated reports. *Medical image analysis*, 66, p.101797.
- [19] Nguyen, H.Q., Lam, K., Le, L.T., Pham, H.H., Tran, D.Q., Nguyen, D.B., Le, D.D., Pham, C.M., Tong, H.T., Dinh, D.H. and Do, C.D., 2022. VinDr-CXR: An open dataset of chest X-rays with radiologist's annotations. *Scientific Data*, 9(1), p.429.
- [20] Tiu, E., Talius, E., Patel, P., Langlotz, C.P., Ng, A.Y. and Rajpurkar, P., 2022. Expert-level detection of pathologies from unannotated chest X-ray images via self-supervised learning. *Nature biomedical engineering*, 6(12), pp.1399-1406.
- [21] Tiu, E., Talius, E., Patel, P., Langlotz, C.P., Ng, A.Y. and Rajpurkar, P., 2022. Expert-level detection of pathologies from unannotated chest X-ray images via self-supervised learning. *Nature biomedical engineering*, 6(12), pp.1399-1406.
- [22] Bannur, S., Hyland, S., Liu, Q., Perez-Garcia, F., Ilse, M., Castro, D.C., Boecking, B., Sharma, H., Bouzid, K., Thieme, A. and Schwaighofer, A., 2023. Learning to exploit temporal structure for biomedical vision-language processing. In *Proceedings of the IEEE/CVF Conference on Computer Vision and Pattern Recognition* (pp. 15016-15027).
- [23] Phan, V.M.H., Xie, Y., Qi, Y., Liu, L., Liu, L., Zhang, B., Liao, Z., Wu, Q., To, M.S. and Verjans, J.W., 2024. Decomposing disease descriptions for enhanced pathology detection: A multi-aspect vision-language pre-training framework. In *Proceedings of the IEEE/CVF Conference on Computer Vision and Pattern Recognition* (pp. 11492-11501).
- [24] Wu, C., Zhang, X., Zhang, Y., Wang, Y. and Xie, W., 2023. Medklip: Medical knowledge enhanced language-image pre-training for x-ray diagnosis. In *Proceedings of the IEEE/CVF International Conference on Computer Vision* (pp. 21372-21383).
- [25] Ye, Y., Zhang, J. and Shi, H., 2024, October. Pseudo-Prompt Generating in Pre-trained Vision-Language Models for Multi-label Medical Image Classification. In *Chinese Conference on Pattern Recognition and Computer Vision (PRCV)* (pp. 279-298). Singapore: Springer Nature Singapore.
- [26] Majkowska, A., Mittal, S., Steiner, D.F., Reicher, J.J., McKinney, S.M., Duggan, G.E., Eswaran, K., Cameron Chen, P.H., Liu, Y., Kalidindi, S.R. and Ding, A., 2020. Chest radiograph

interpretation with deep learning models: assessment with radiologist-adjudicated reference standards and population-adjusted evaluation. *Radiology*, 294(2), pp.421-431.

[27] Demner-Fushman, D., Kohli, M.D., Rosenman, M.B., Shooshan, S.E., Rodriguez, L., Antani, S., Thoma, G.R. and McDonald, C.J., 2016. Preparing a collection of radiology examinations for distribution and retrieval. *Journal of the American Medical Informatics Association*, 23(2), pp.304-310.

[28] Baughan, N., Whitney, H.M., Drukker, K., Sahiner, B., Hu, T., McNitt-Gray, M., Myers, K. and Giger, M.L., 2022, April. Sequestration of imaging studies in MIDRC: a multi-institutional data commons. In *Medical Imaging 2022: Image Perception, Observer Performance, and Technology Assessment* (Vol. 12035, pp. 91-98). SPIE.

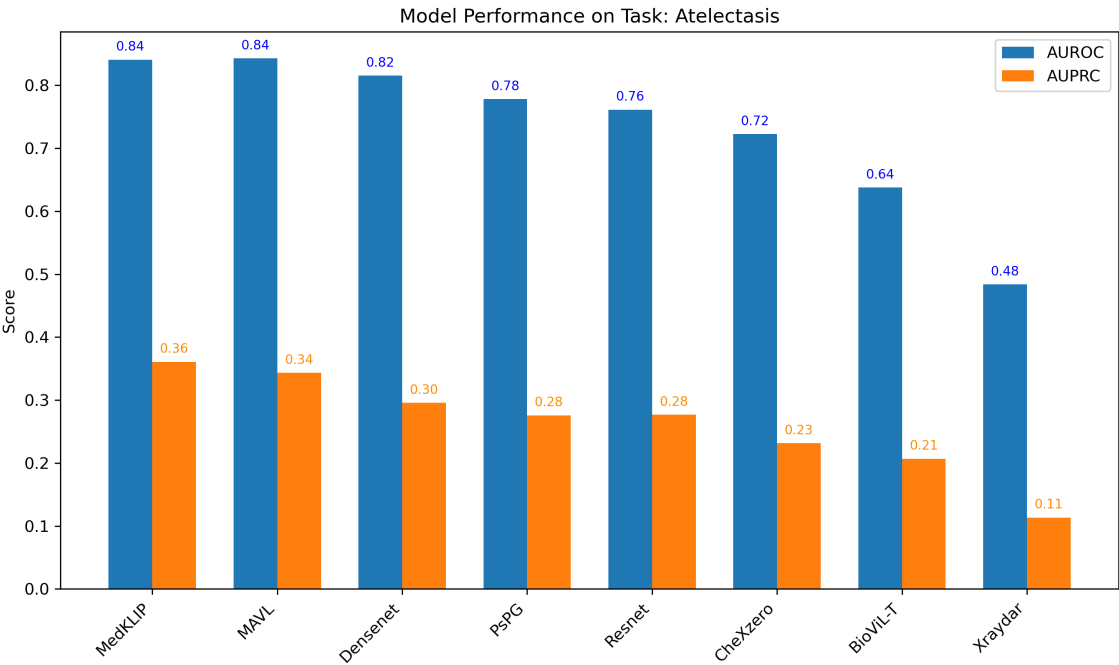
[29] Li, M.D., Arun, N.T., Gidwani, M., Chang, K., Deng, F., Little, B.P., Mendoza, D.P., Lang, M., Lee, S.I., O'Shea, A. and Parakh, A., 2020. Automated assessment and tracking of COVID-19 pulmonary disease severity on chest radiographs using convolutional siamese neural networks. *Radiology: Artificial Intelligence*, 2(4), p.e200079.

[30] Pourpanah, F., Abdar, M., Luo, Y., Zhou, X., Wang, R., Lim, C.P., Wang, X.Z. and Wu, Q.J., 2022. A review of generalized zero-shot learning methods. *IEEE transactions on pattern analysis and machine intelligence*, 45(4), pp.4051-4070.

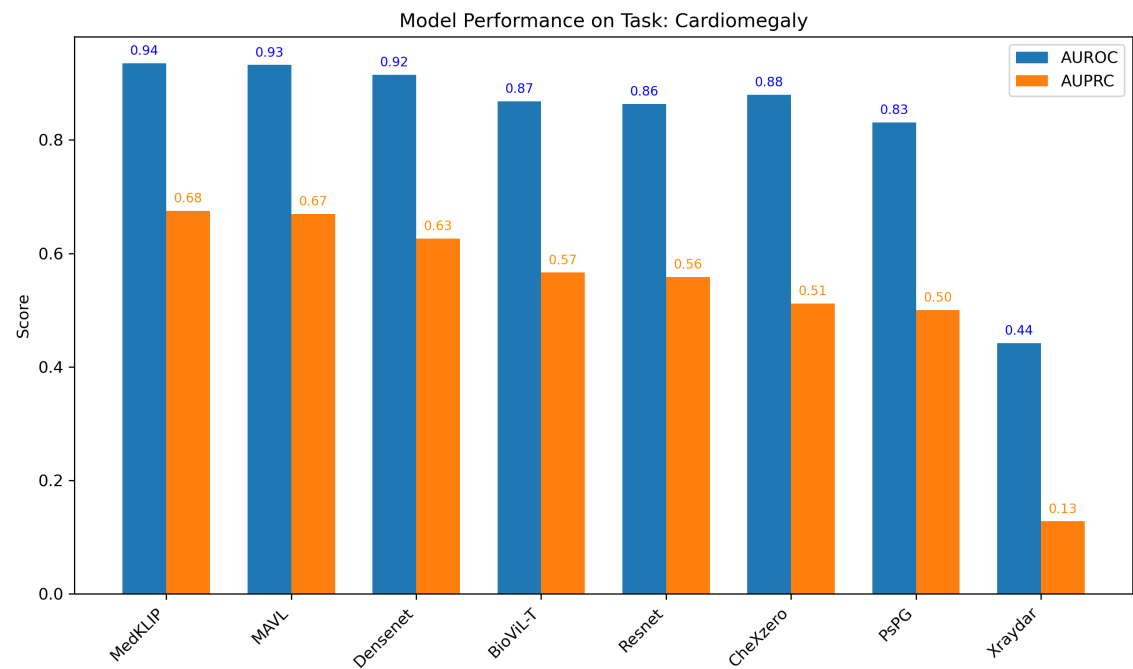
Supplementary Note 1

Chest X-ray Model Benchmark – Tasks in Public Datasets

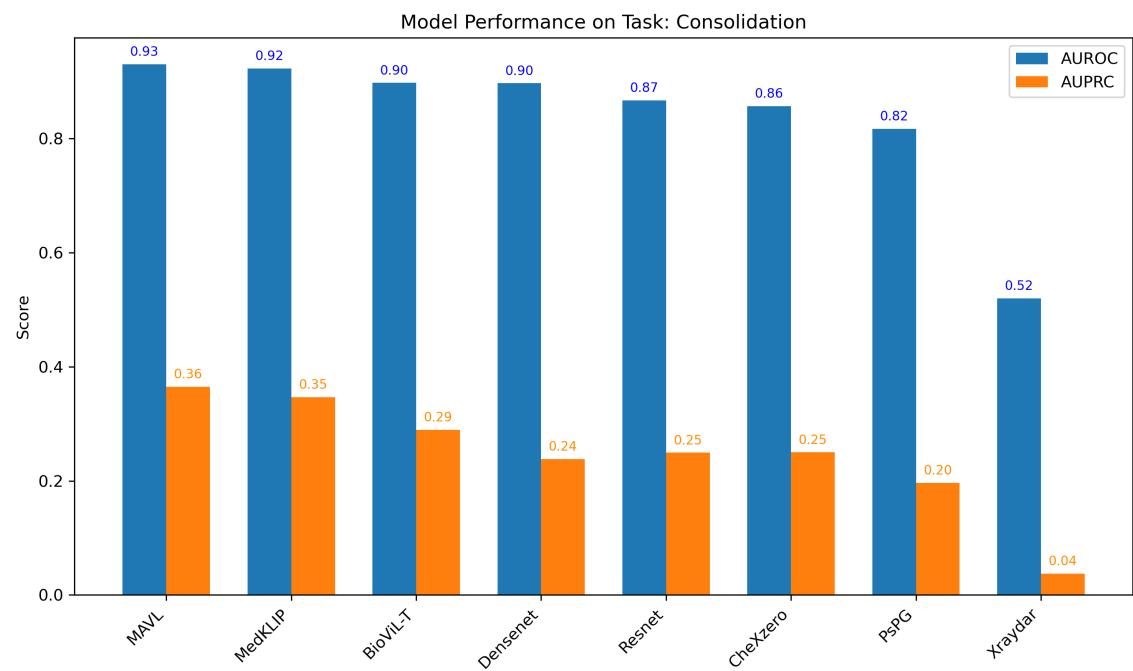
Atelectasis



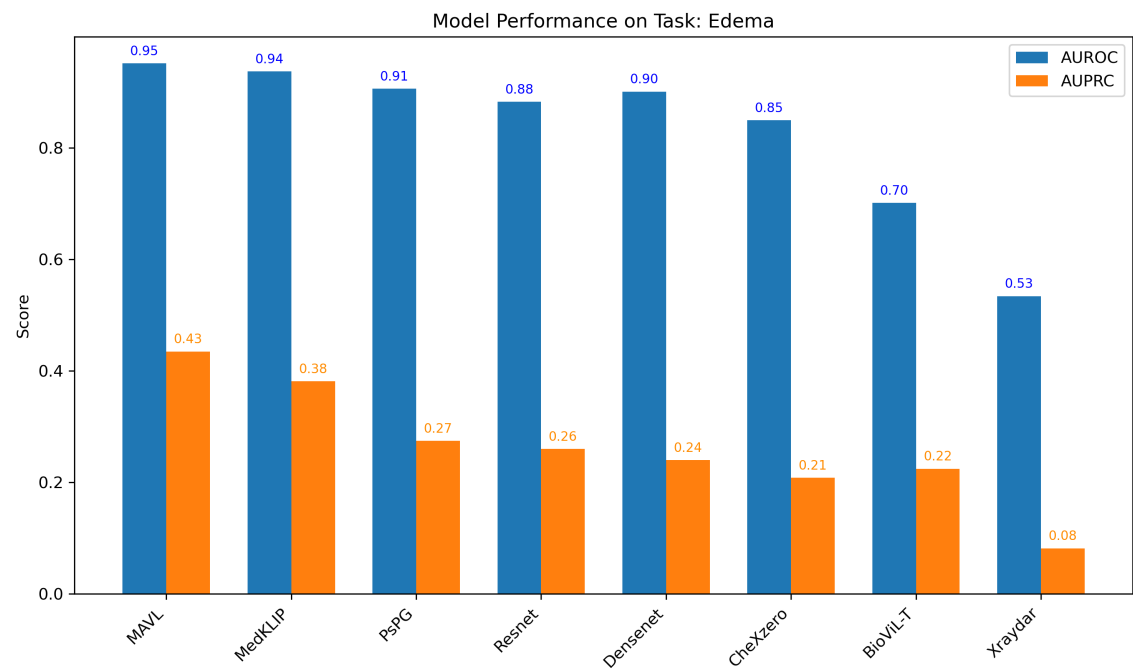
Cardiomegaly



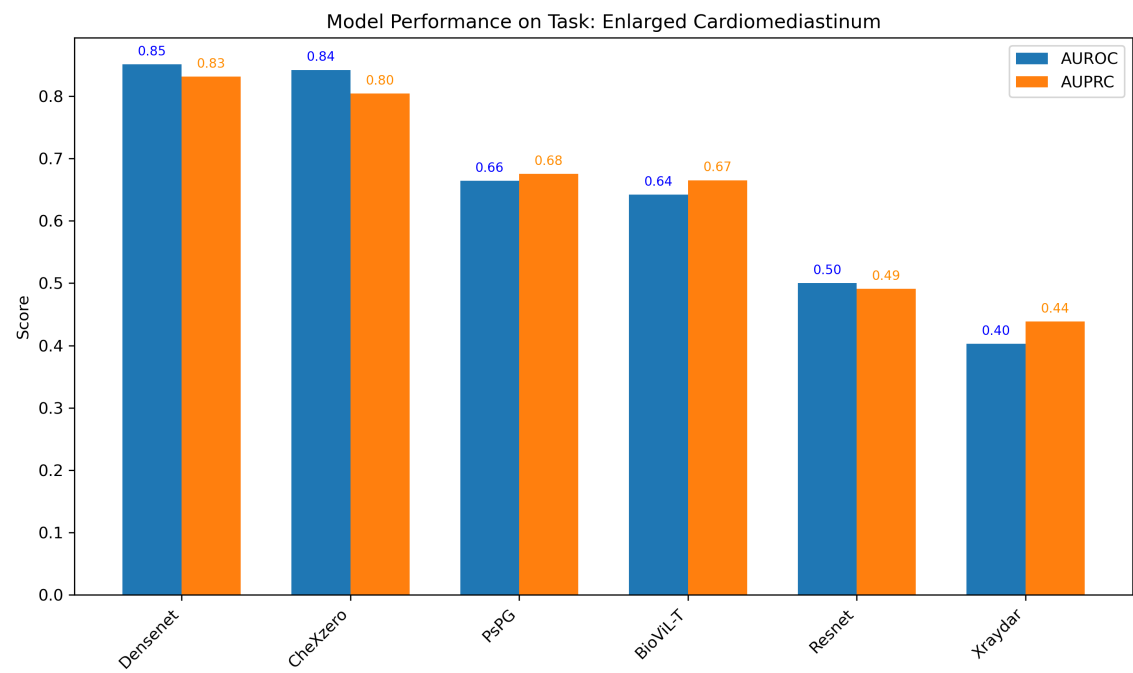
Consolidation



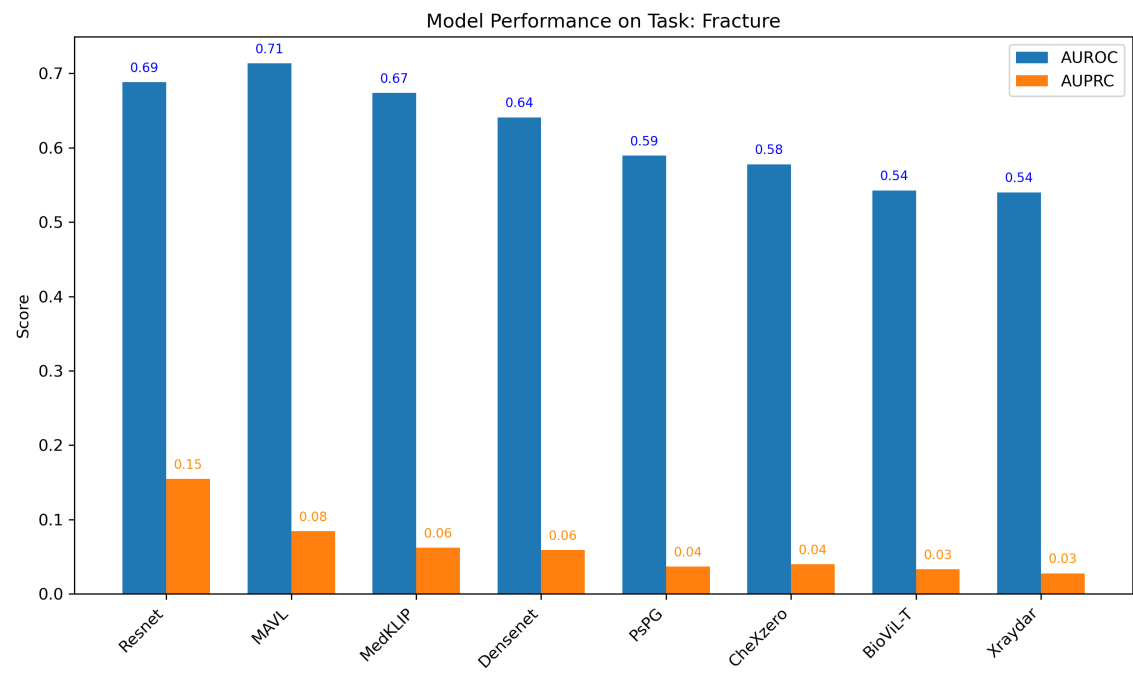
Edema



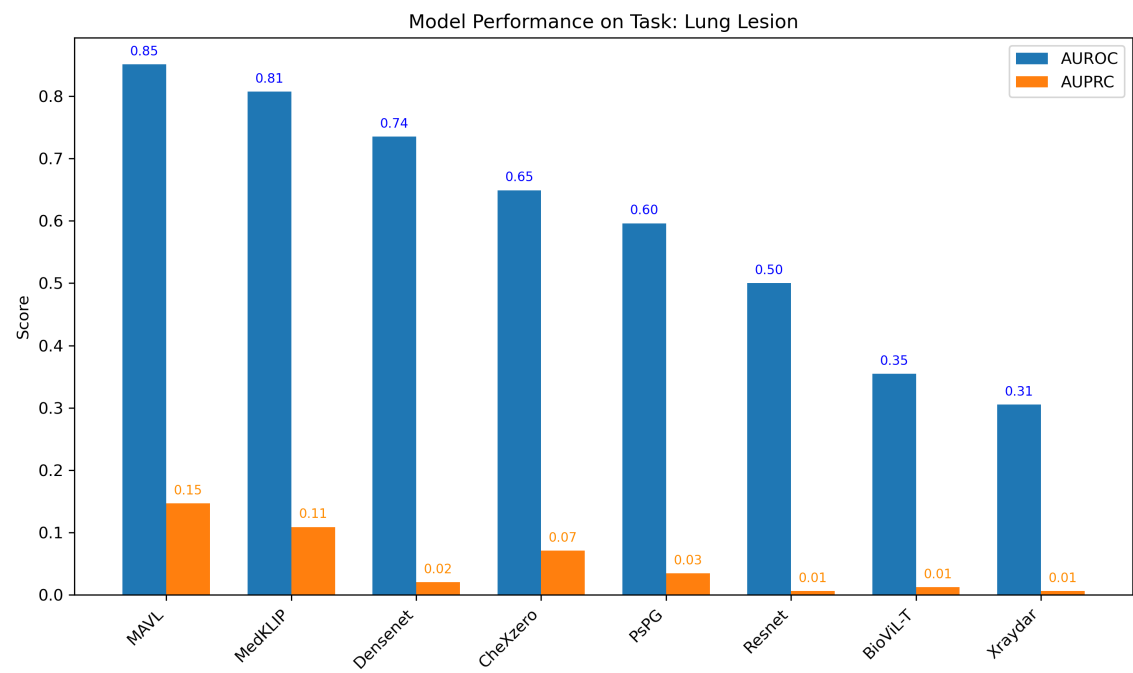
Enlarged Cardiomediatinum



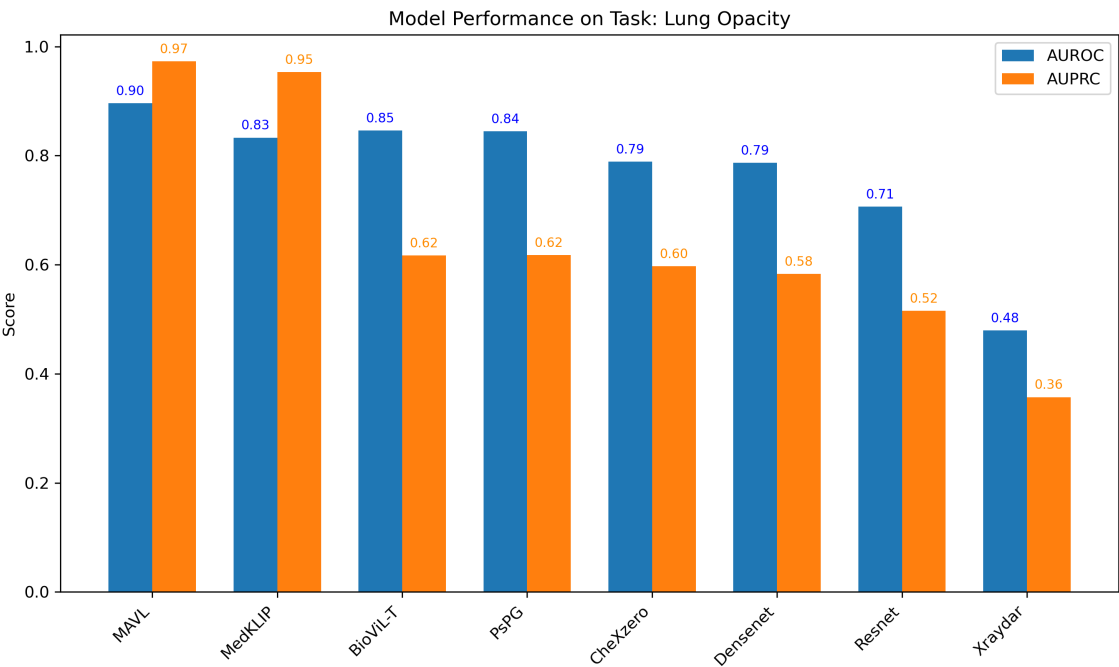
Fracture



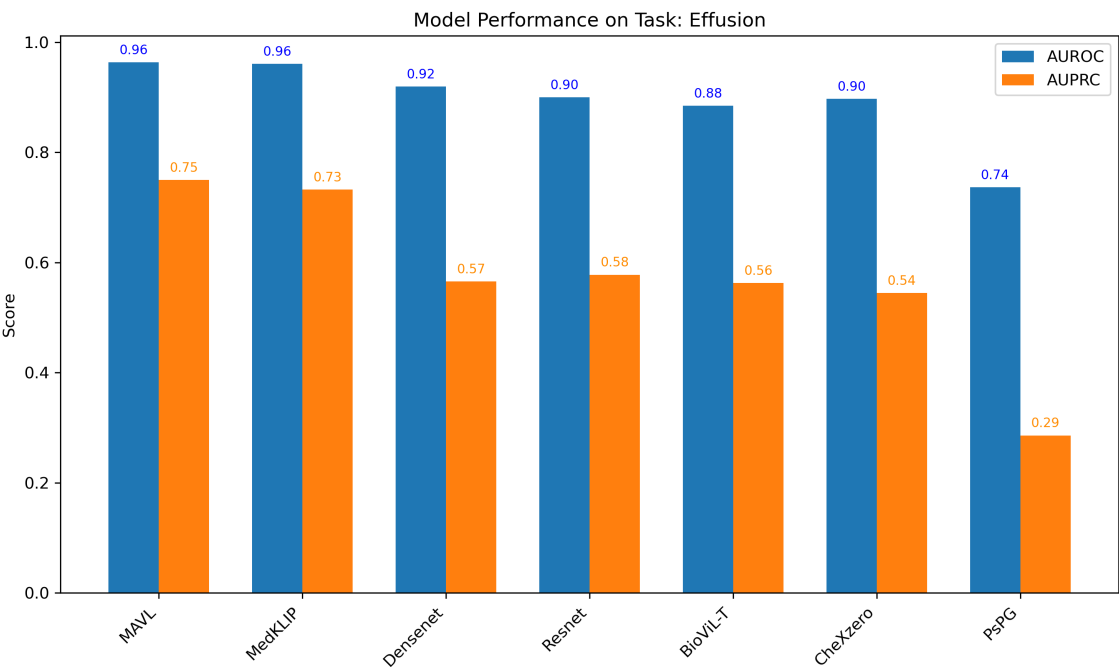
Lung Lesion



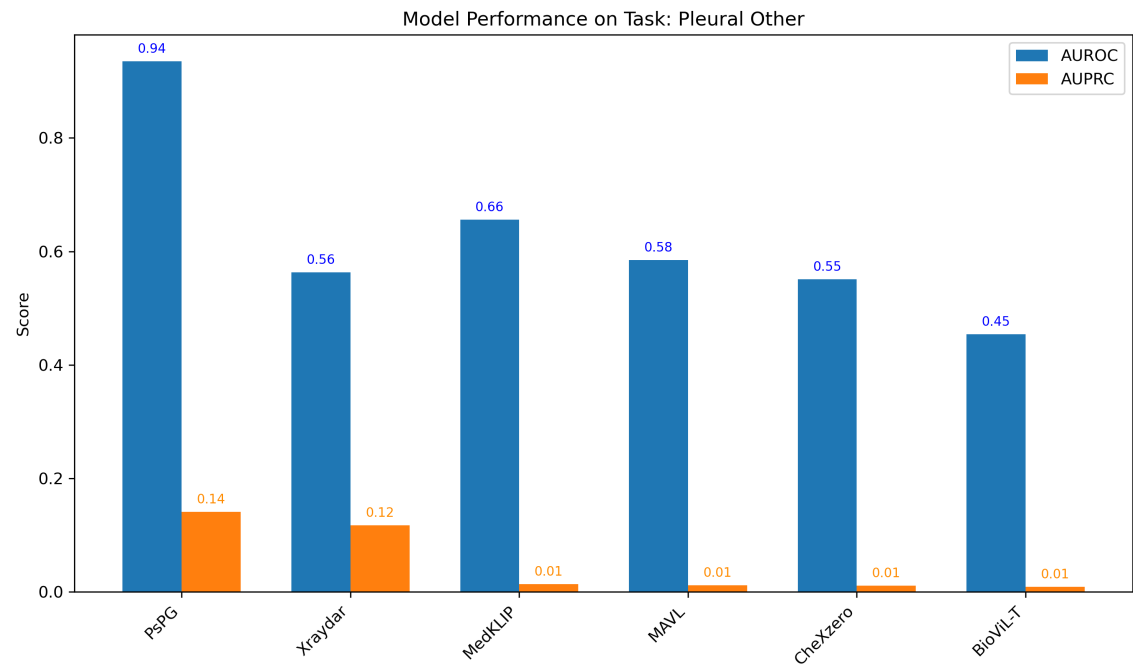
Lung Opacity



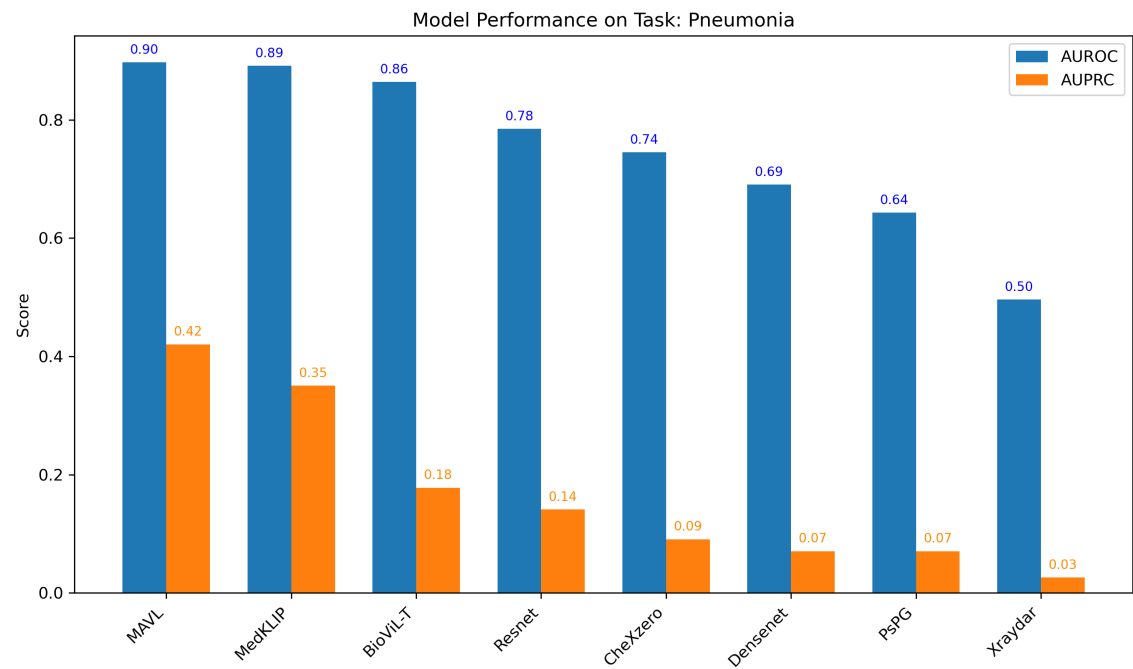
Effusion



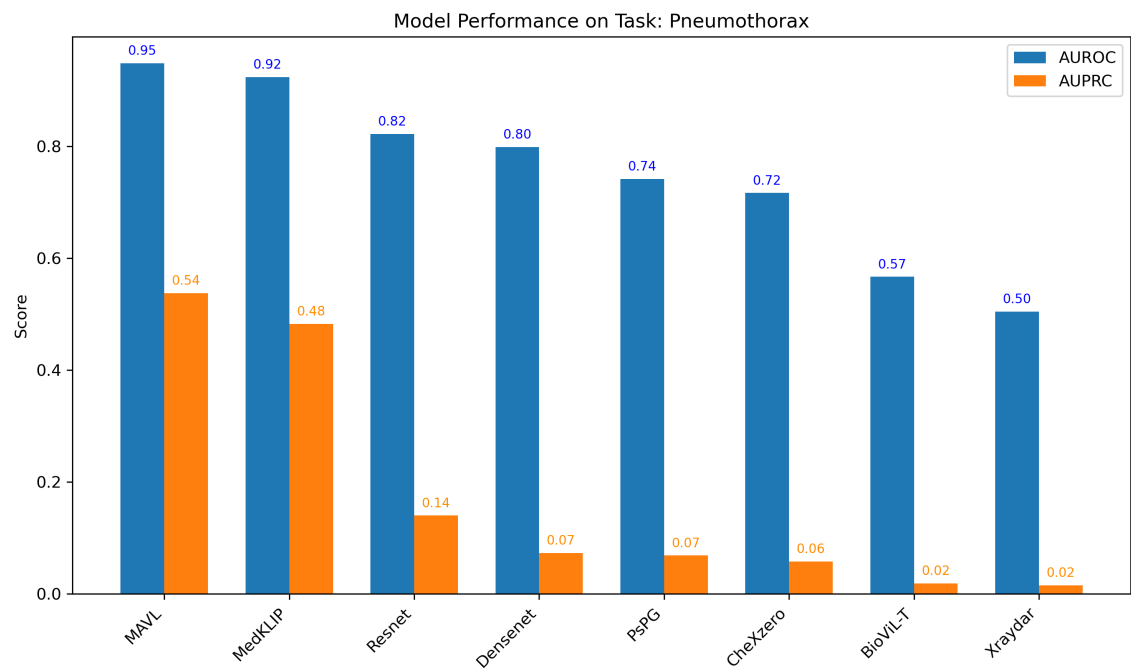
Pleural Other



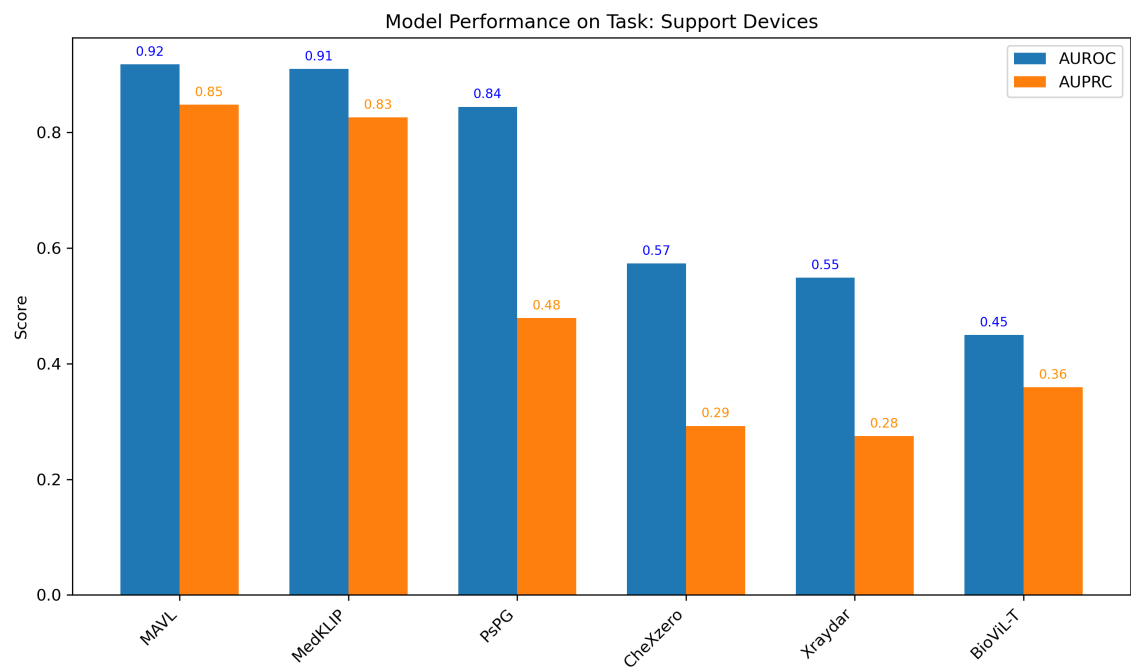
Pneumonia



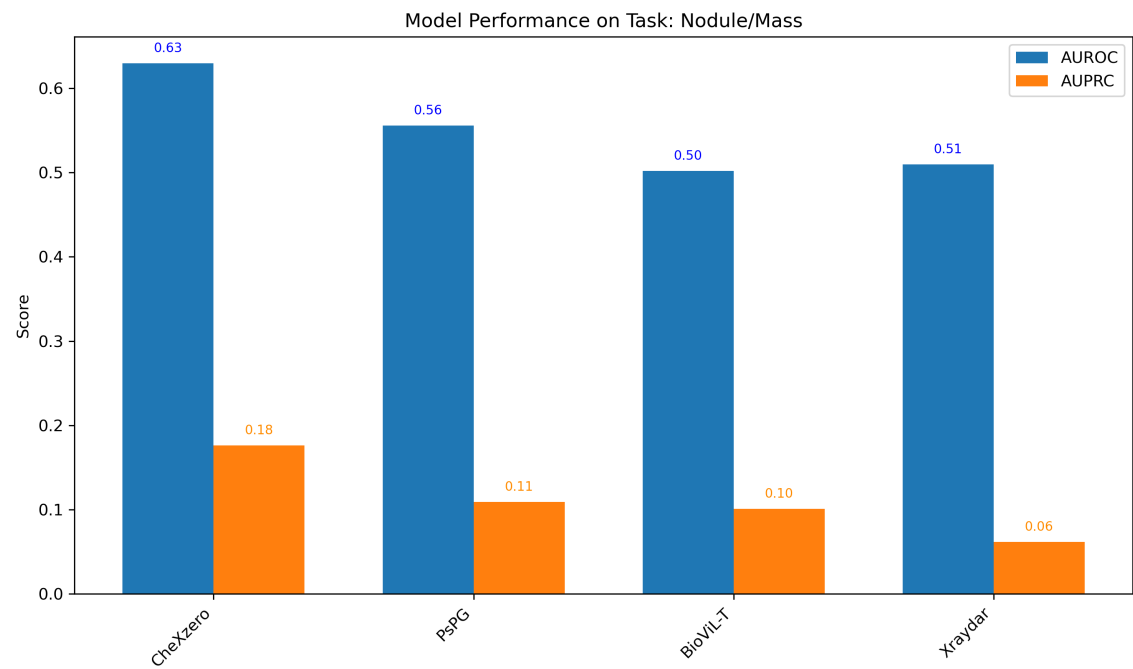
Pneumothorax



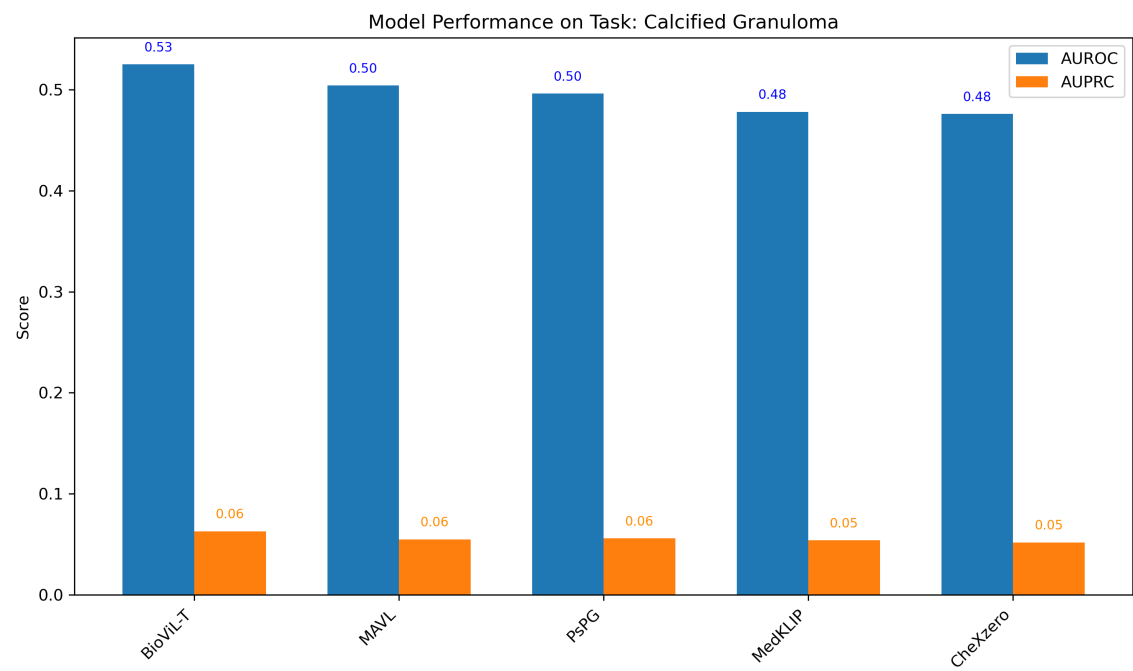
Support Devices



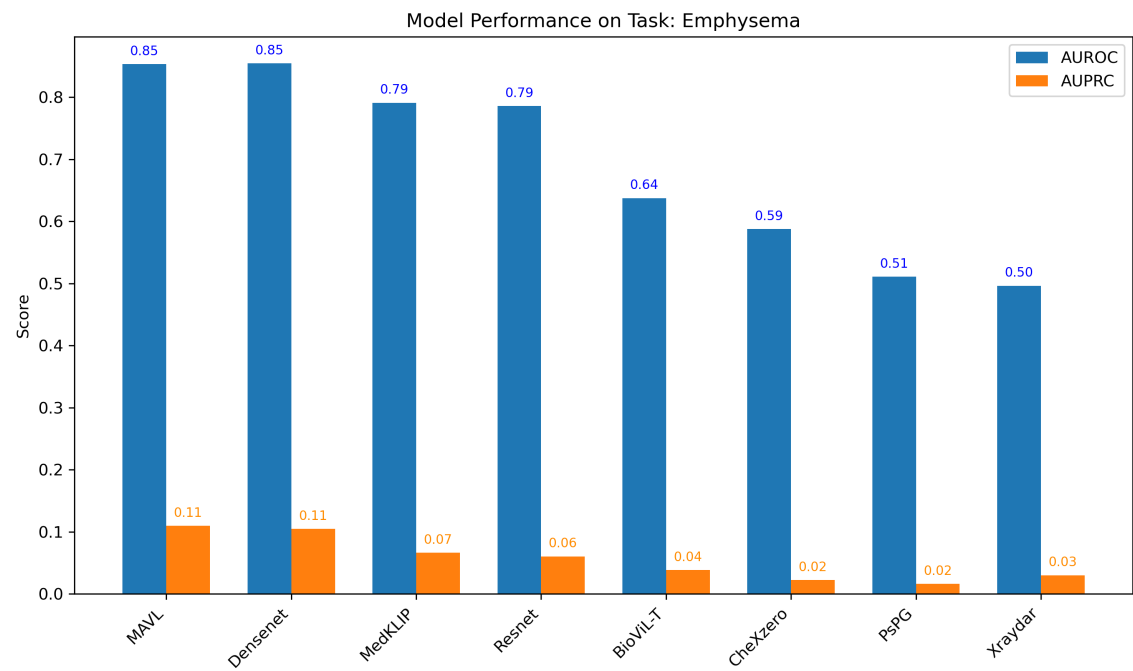
Nodule/Mass



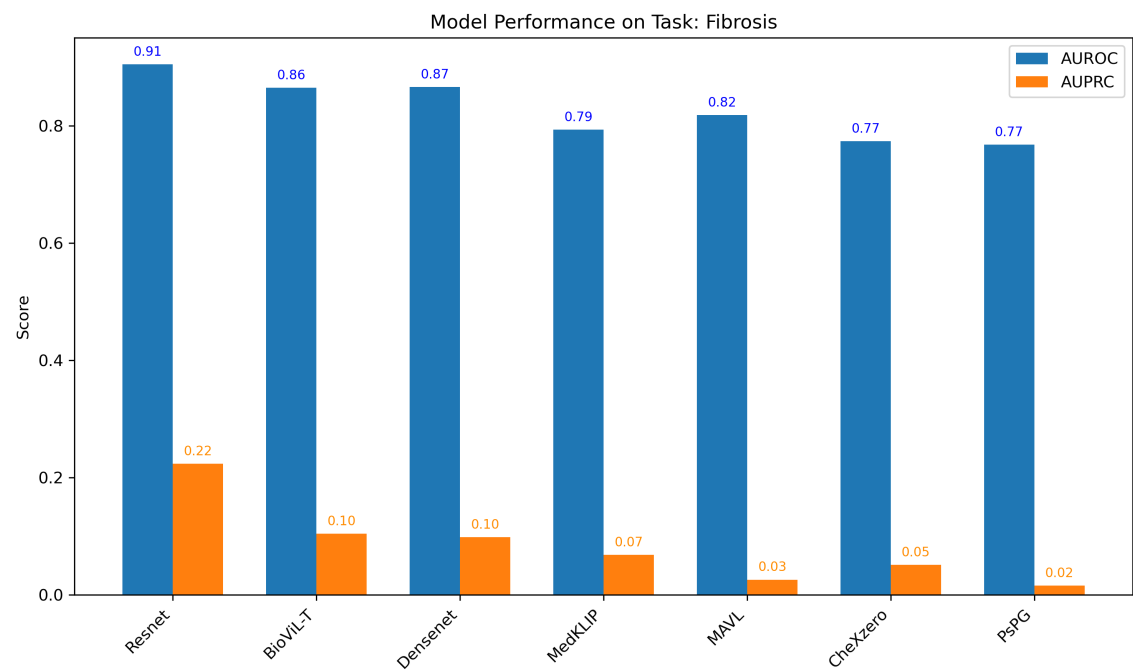
Calcified Granuloma



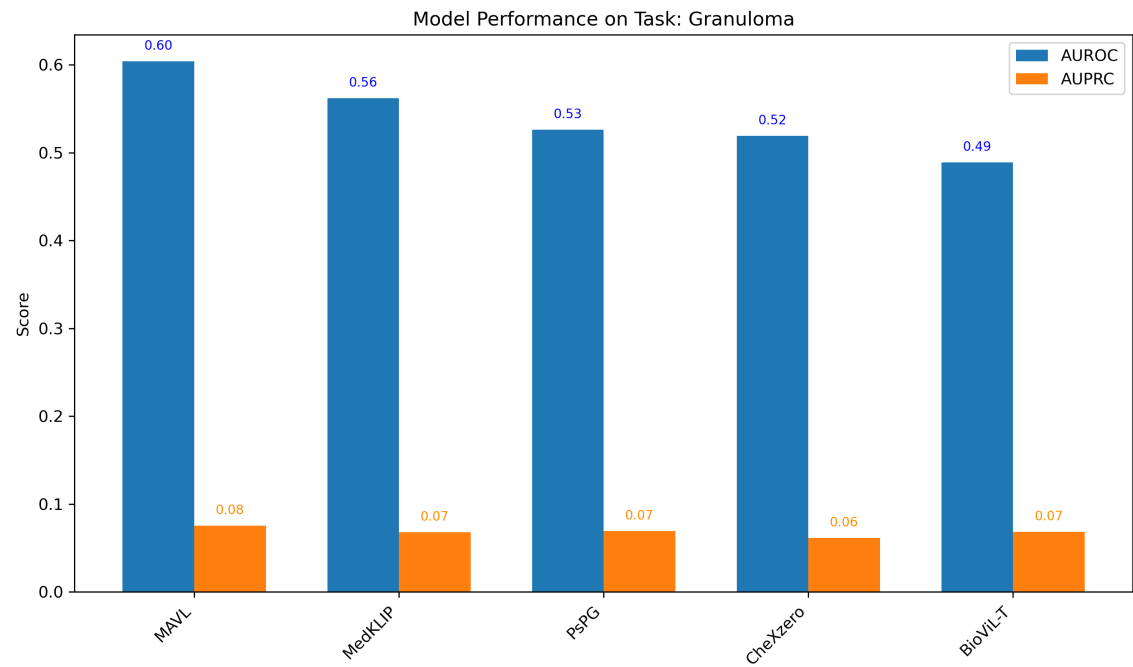
Emphysema



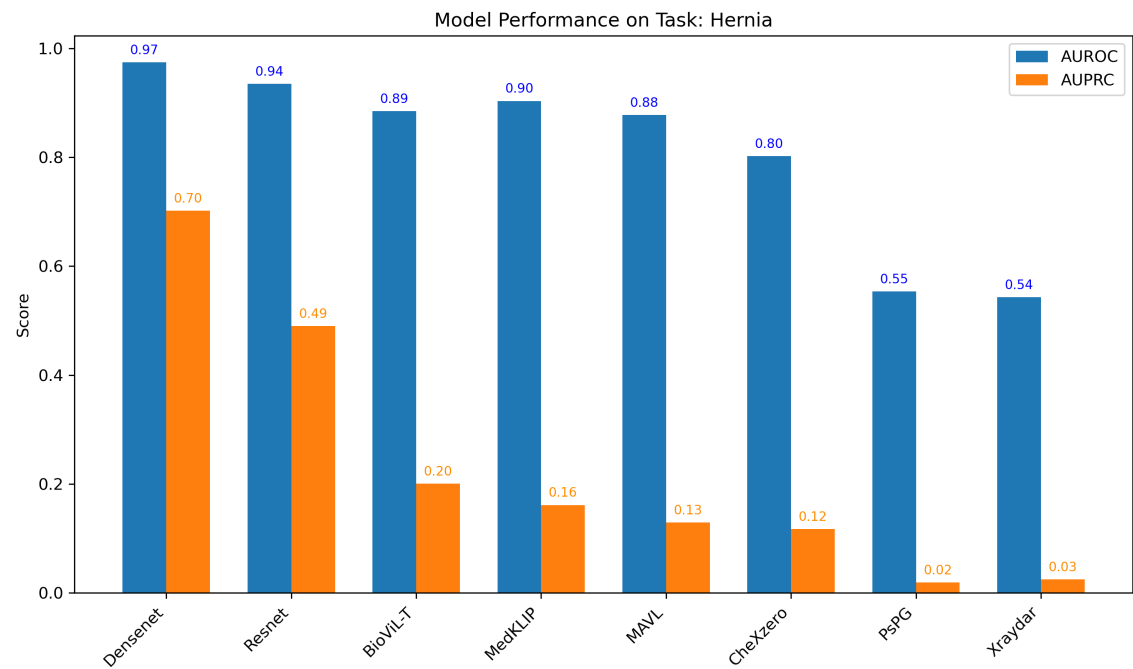
Fibrosis



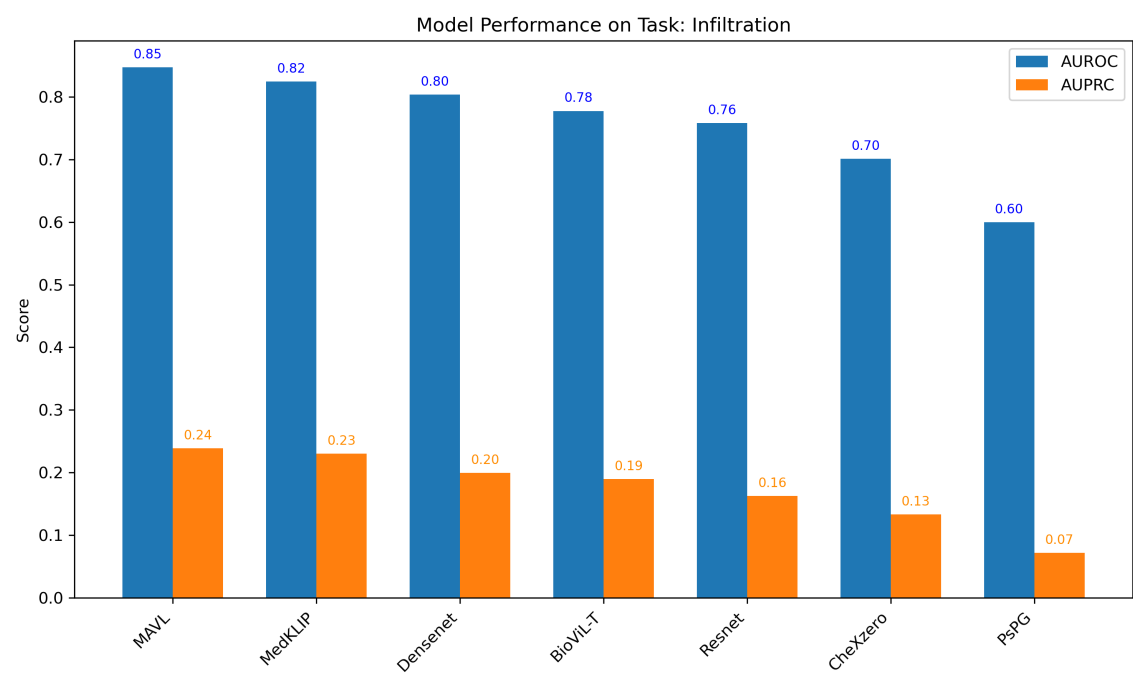
Granuloma



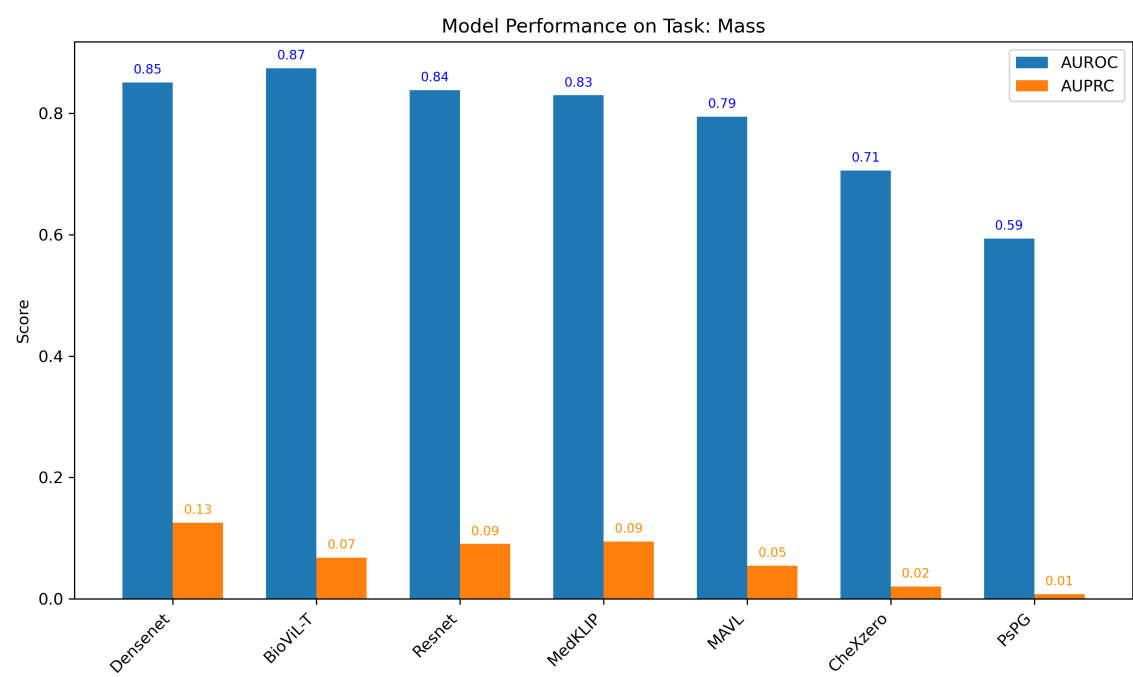
Hernia



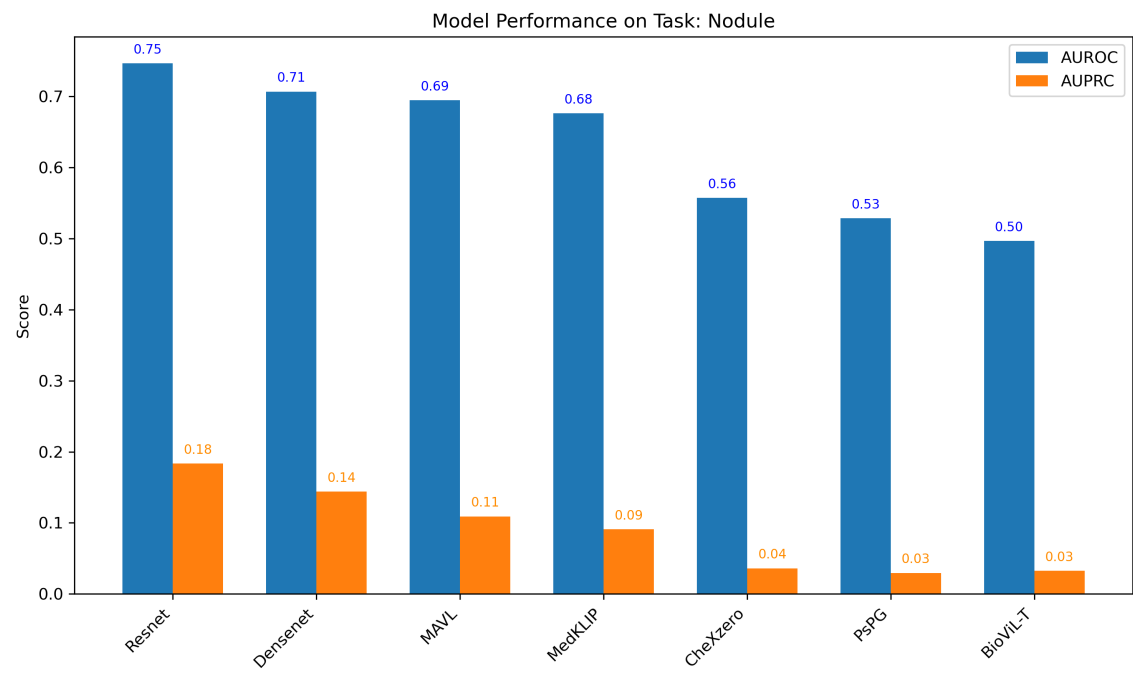
Infiltration



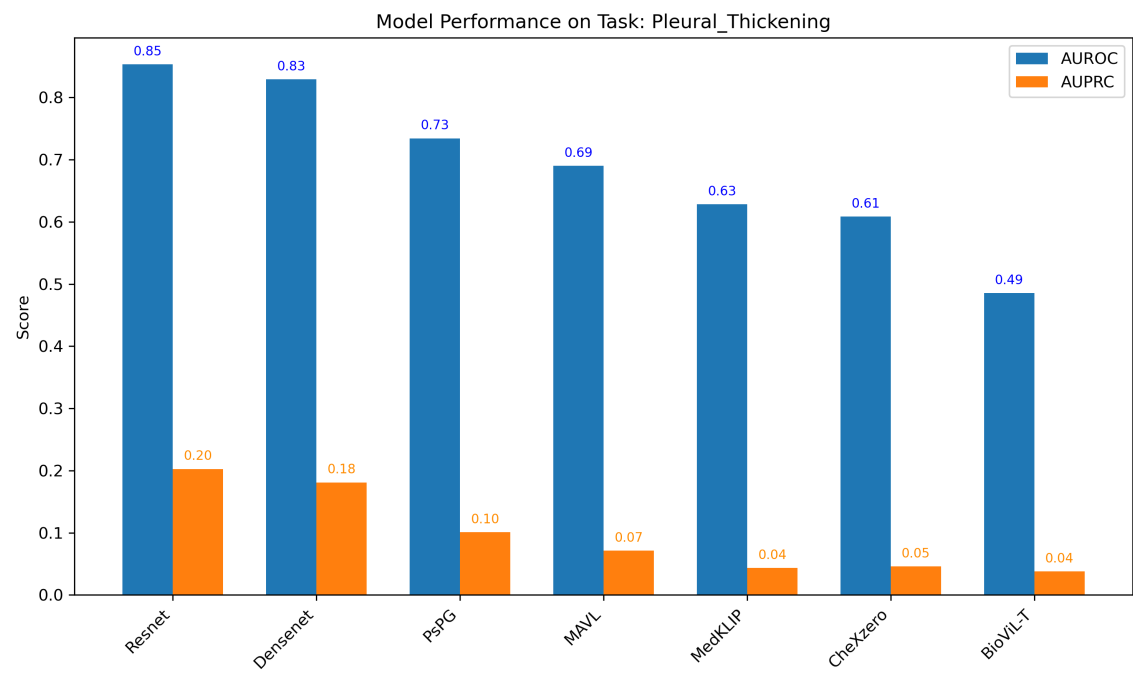
Mass



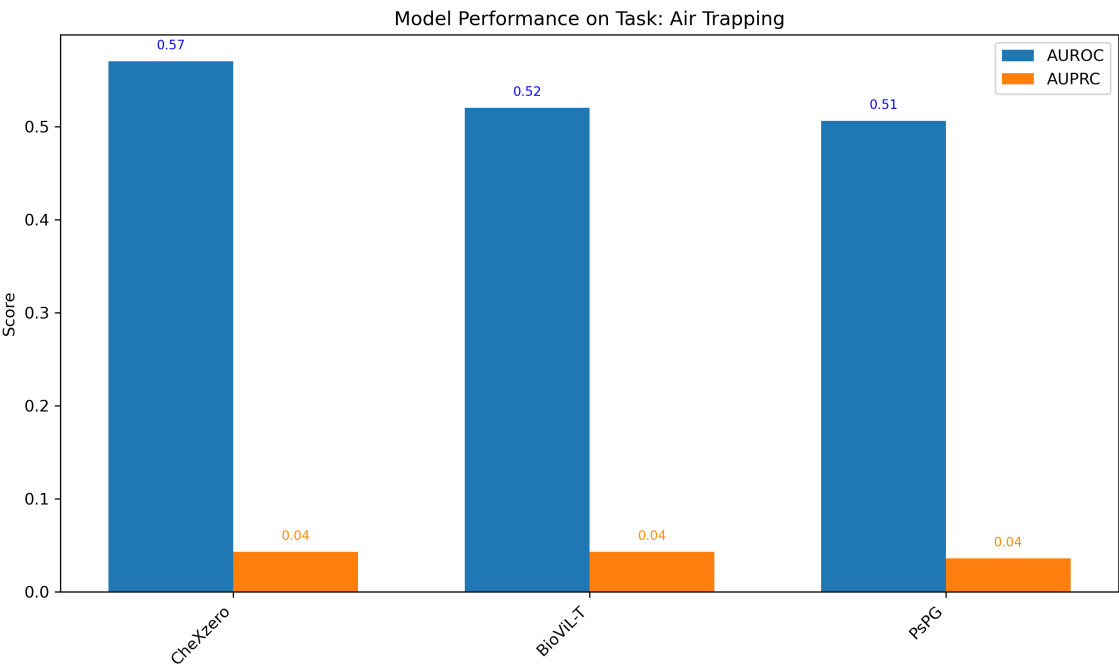
Nodule



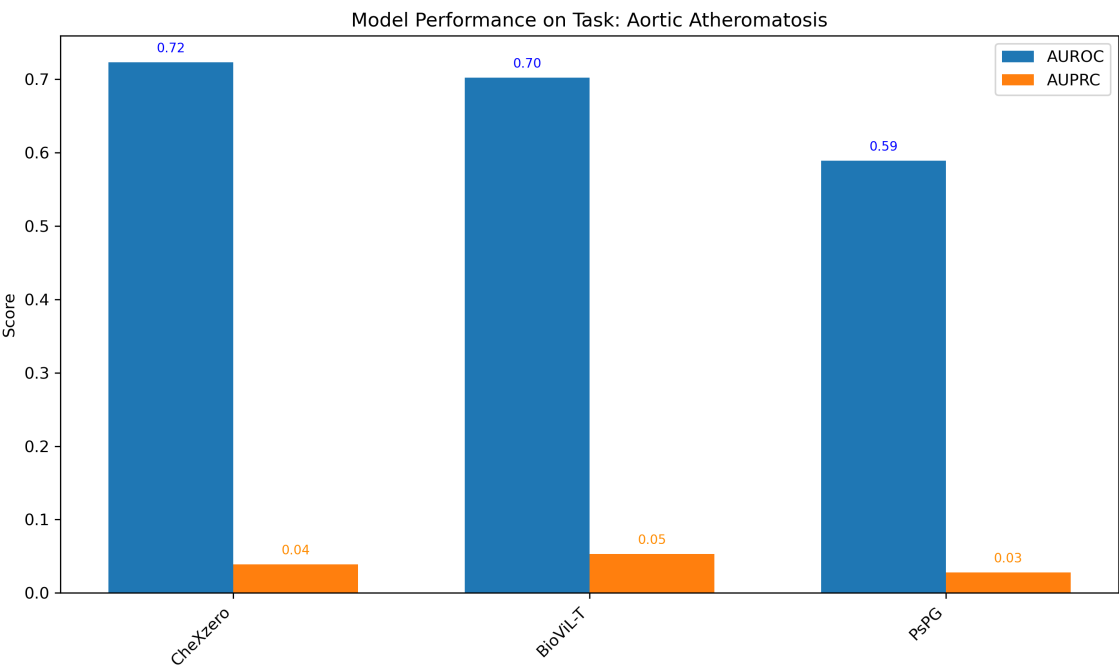
Pleural_Thickening



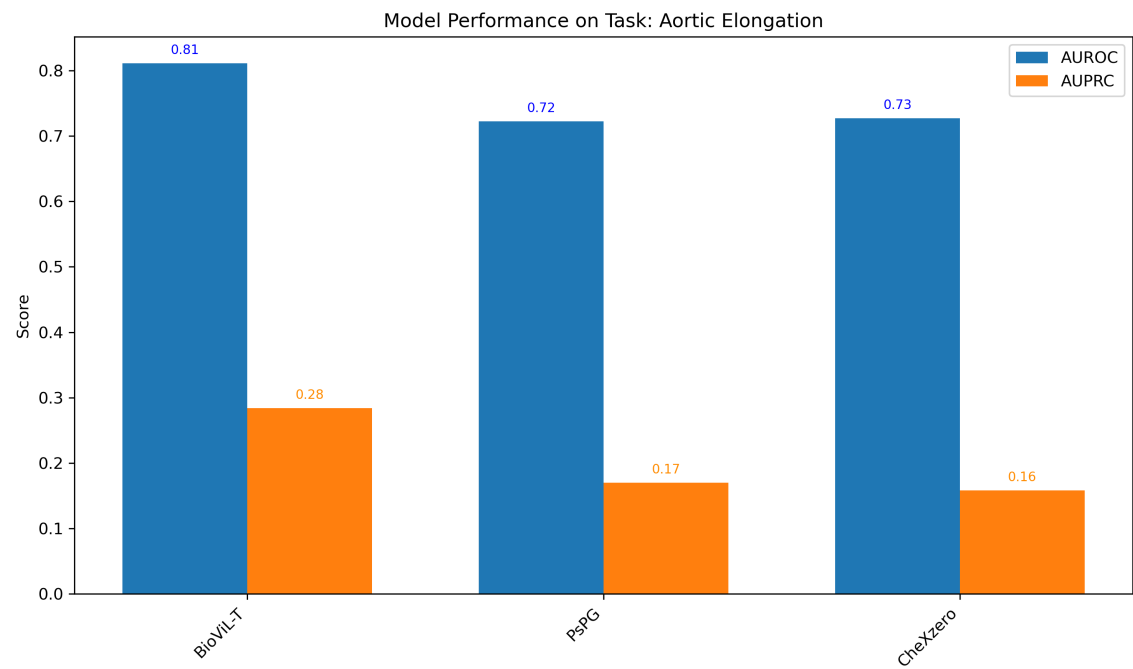
Air Trapping



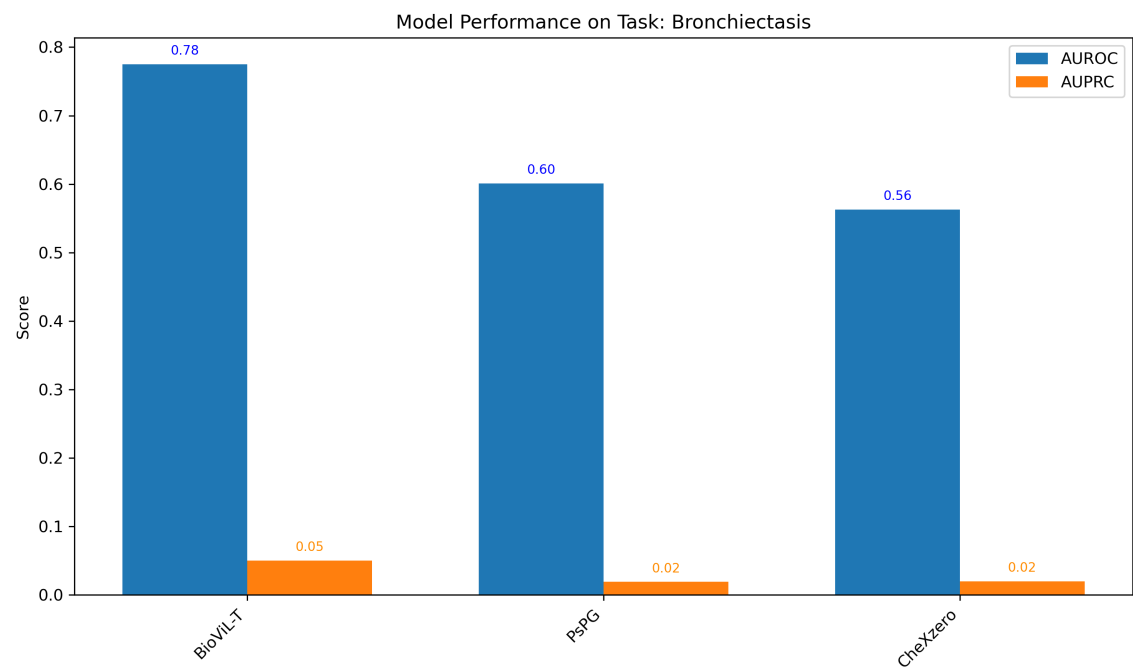
Aortic Atheromatosis



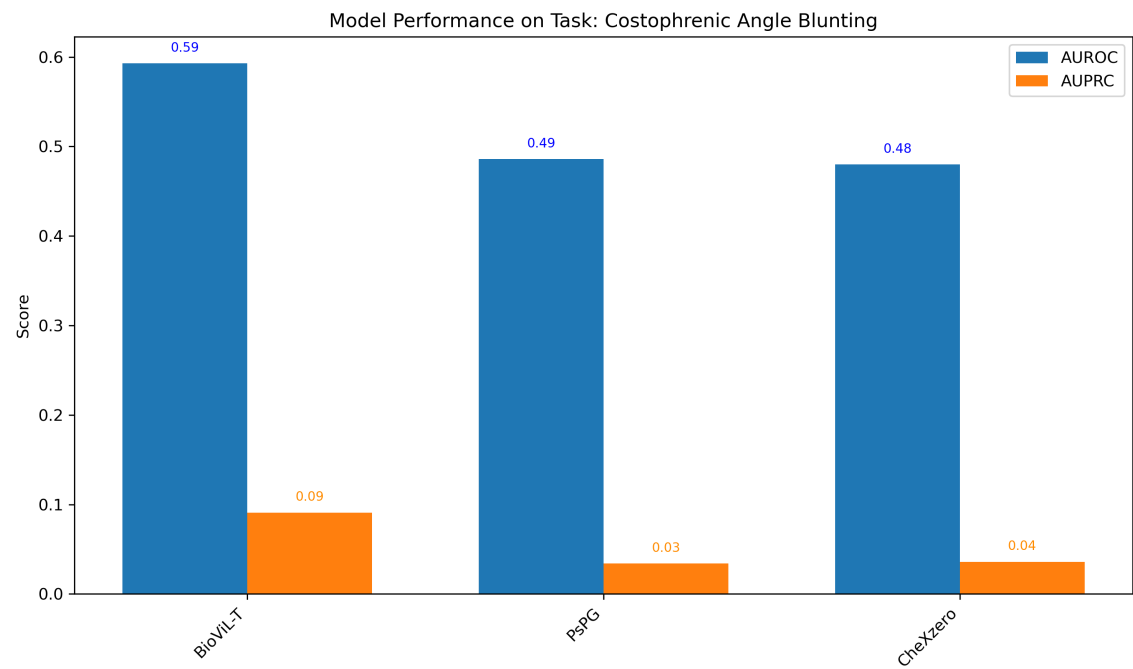
Aortic Elongation



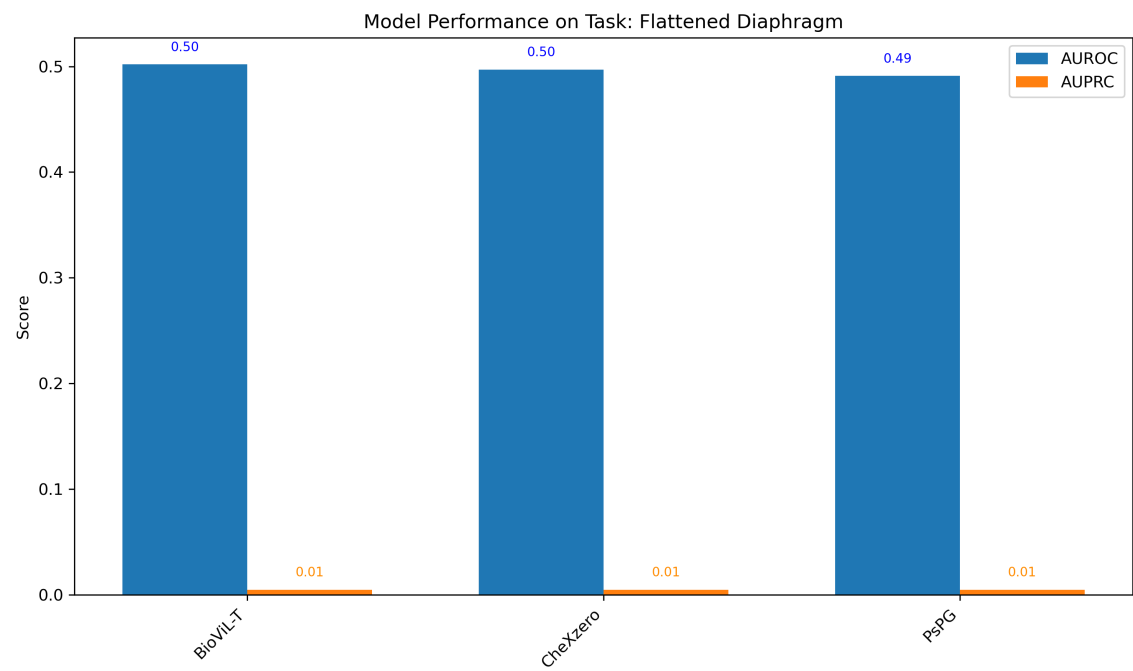
Bronchiectasis



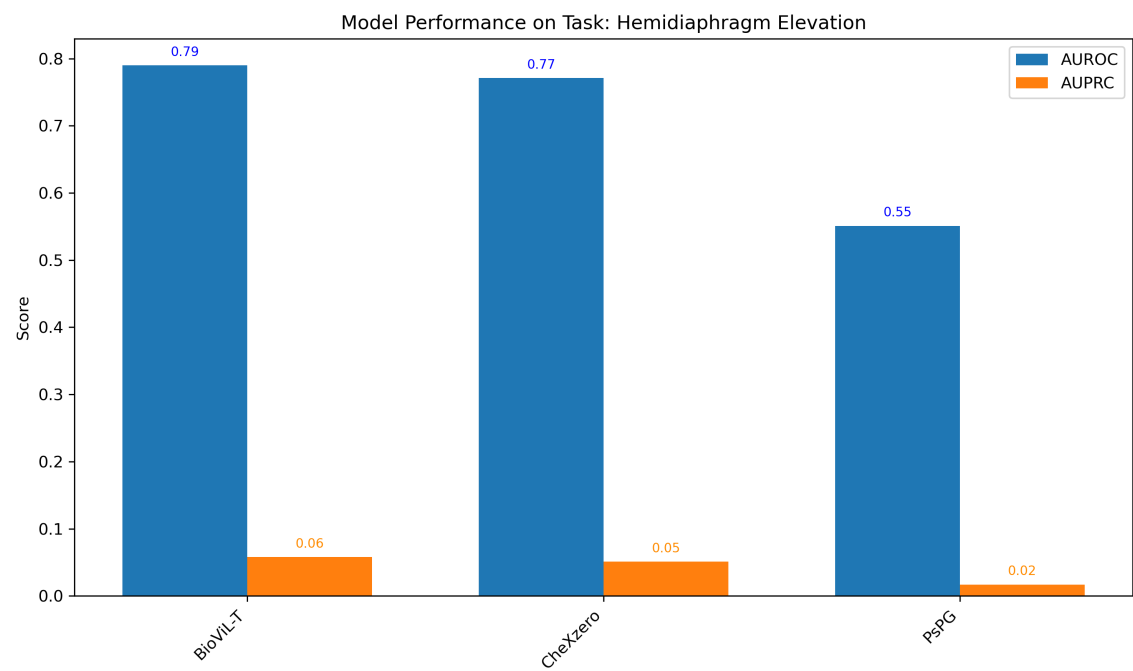
Costophrenic Angle Blunting



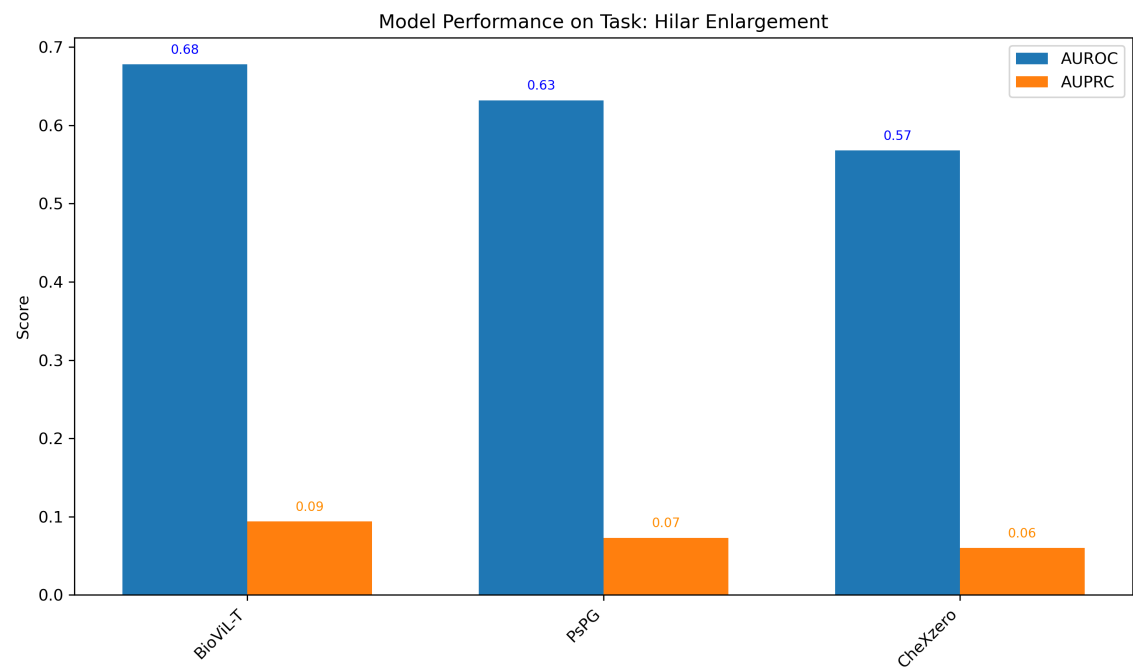
Flattened Diaphragm



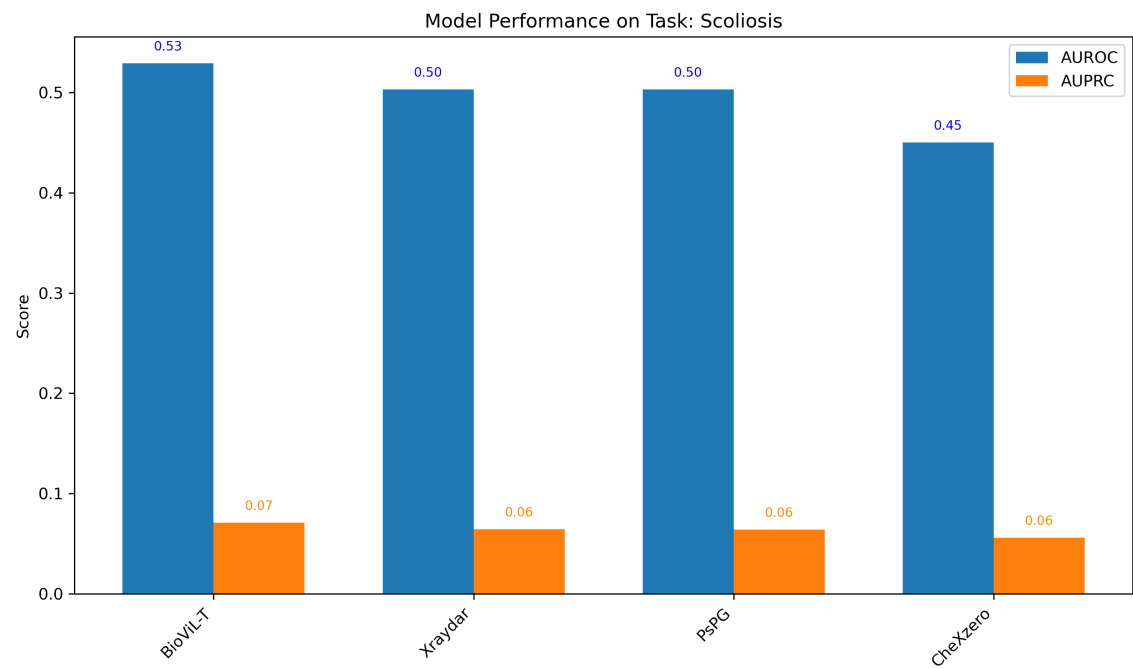
Hemidiaphragm Elevation



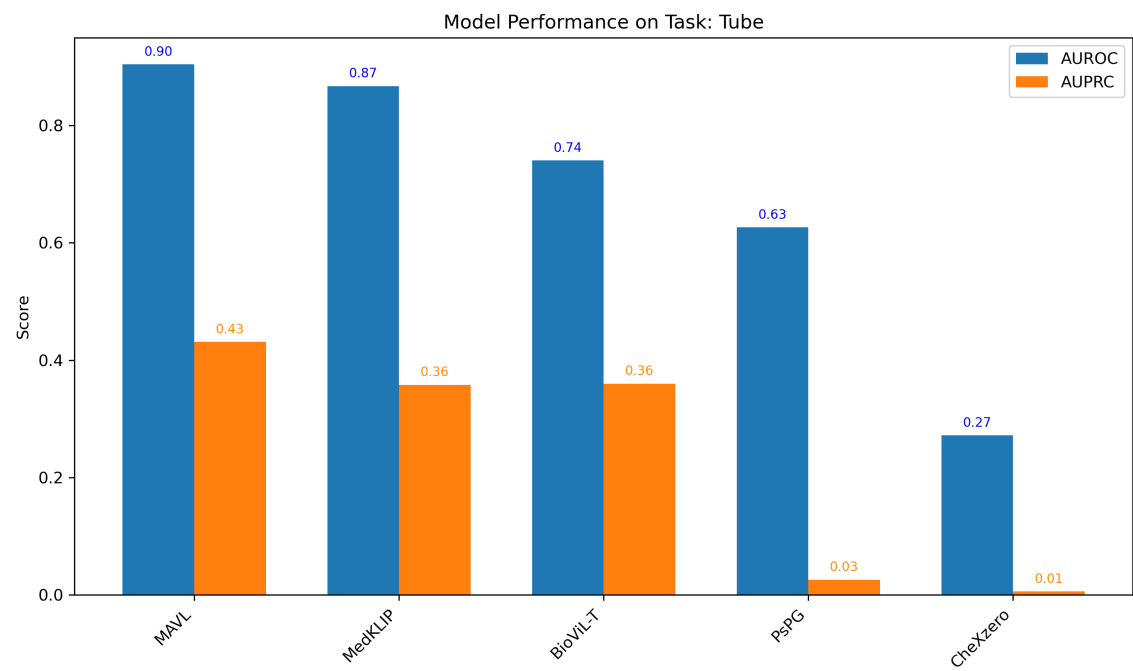
Hilar Enlargement



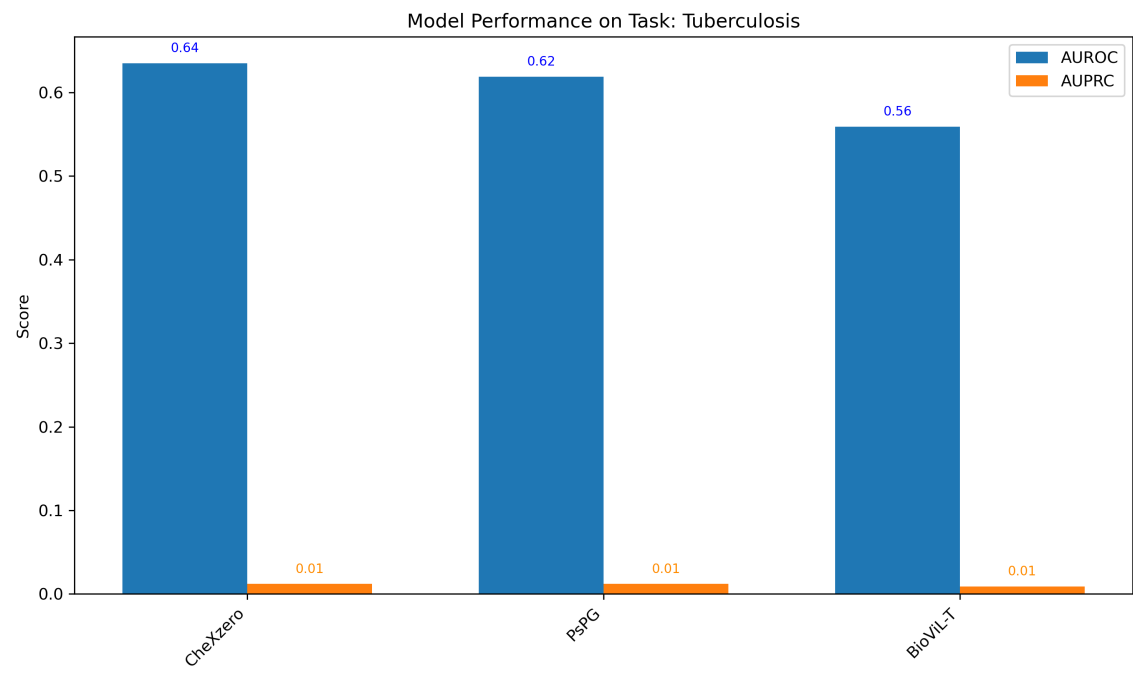
Scoliosis



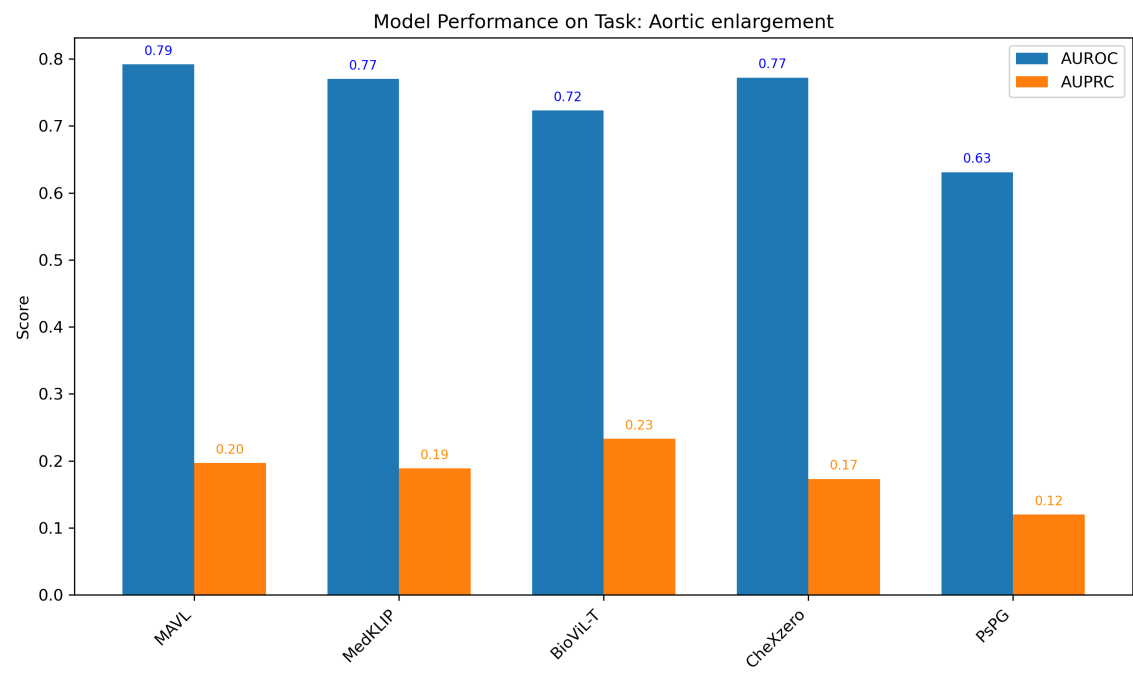
Tube



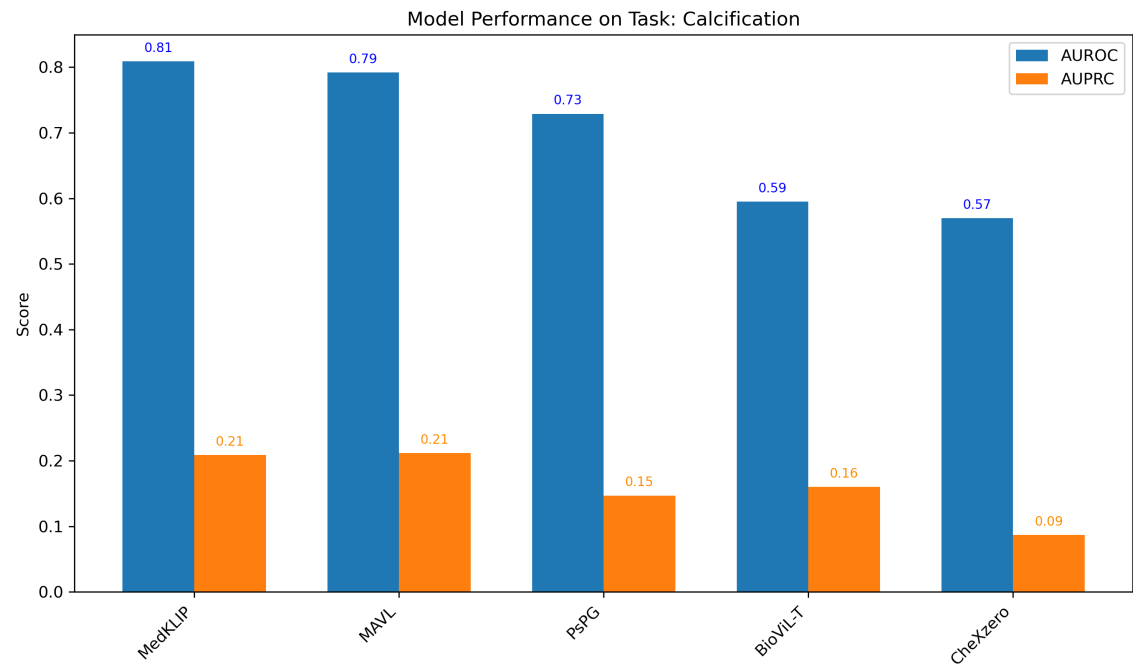
Tuberculosis



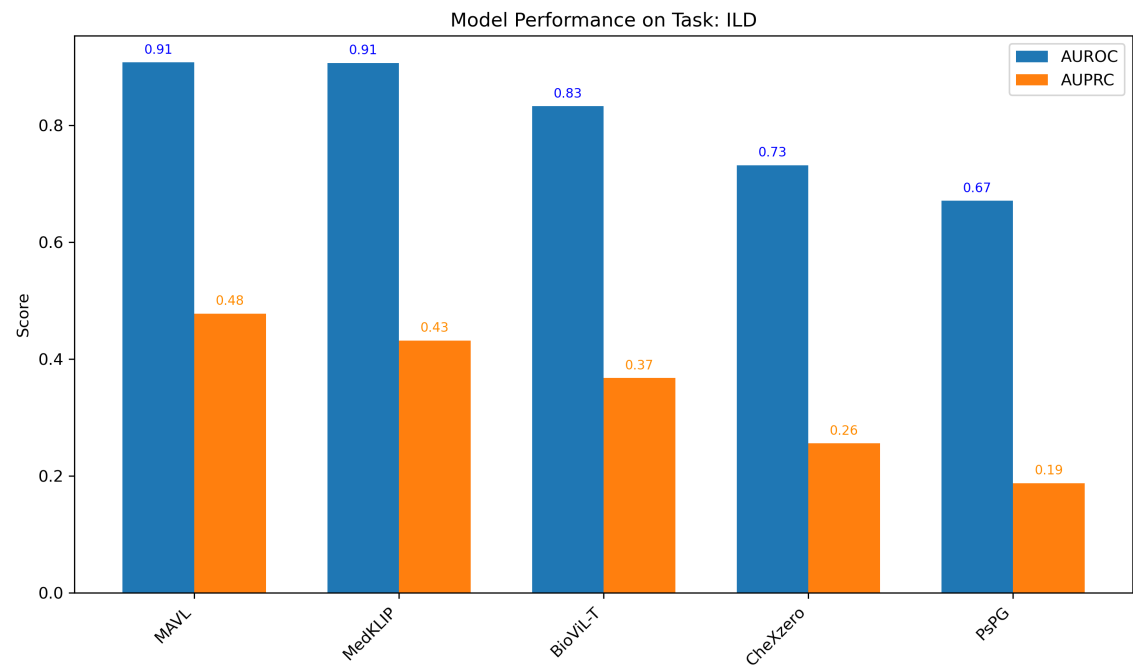
Aortic enlargement



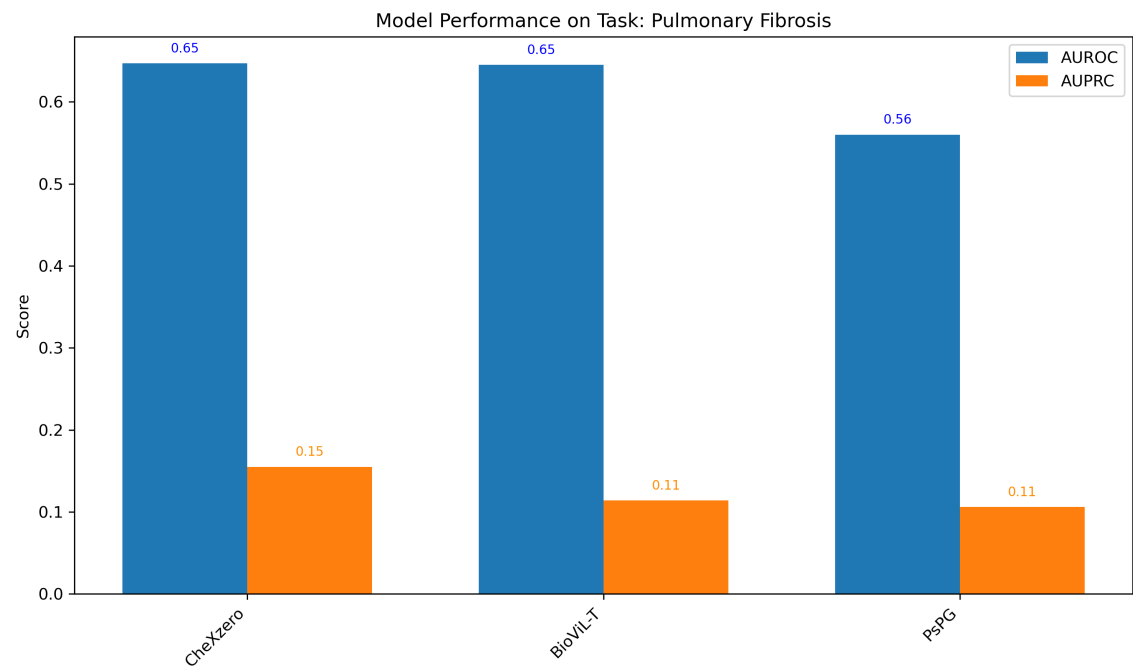
Calcification



ILD



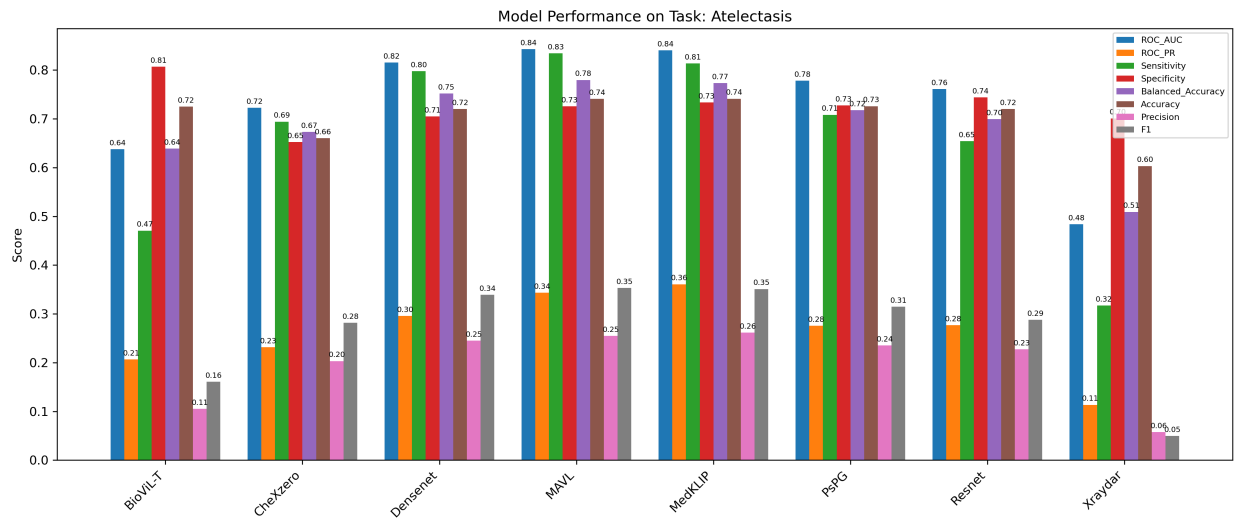
Pulmonary Fibrosis



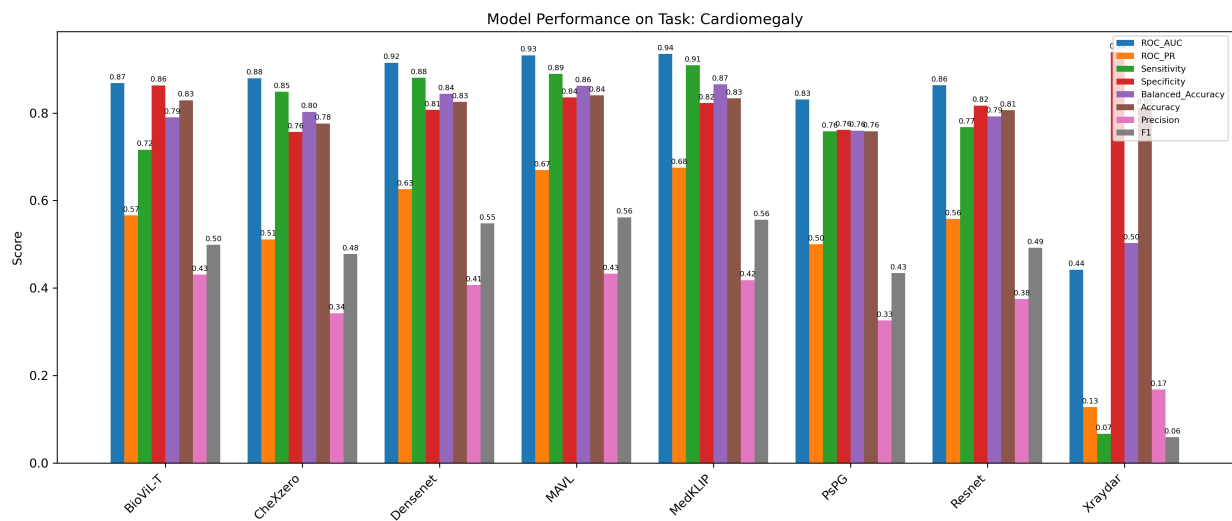
Supplementary Note 2

Model Performance on All Tasks (All Metrics)

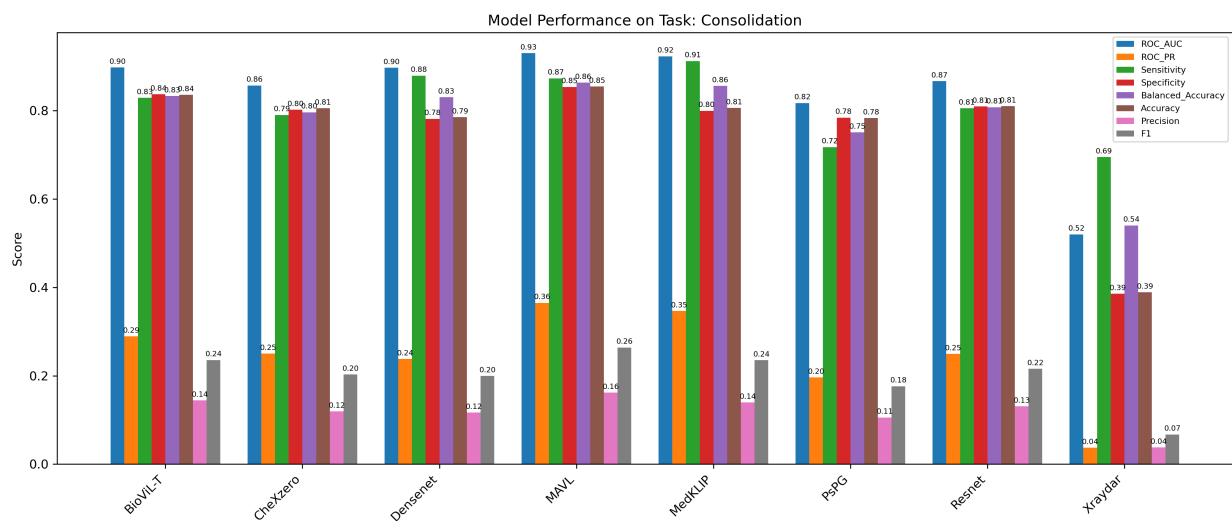
Atelectasis



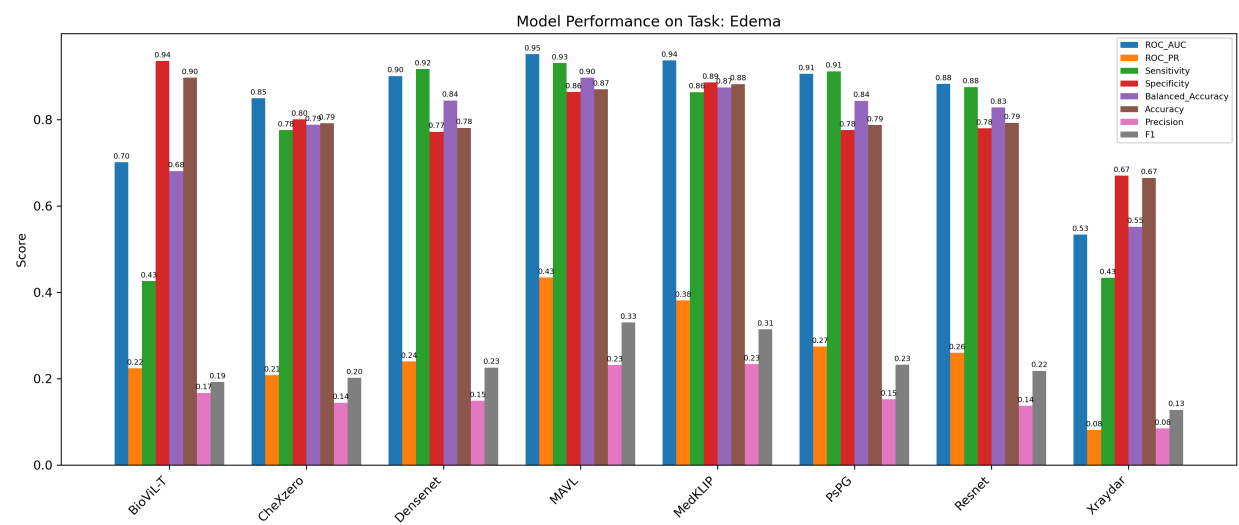
Cardiomegaly



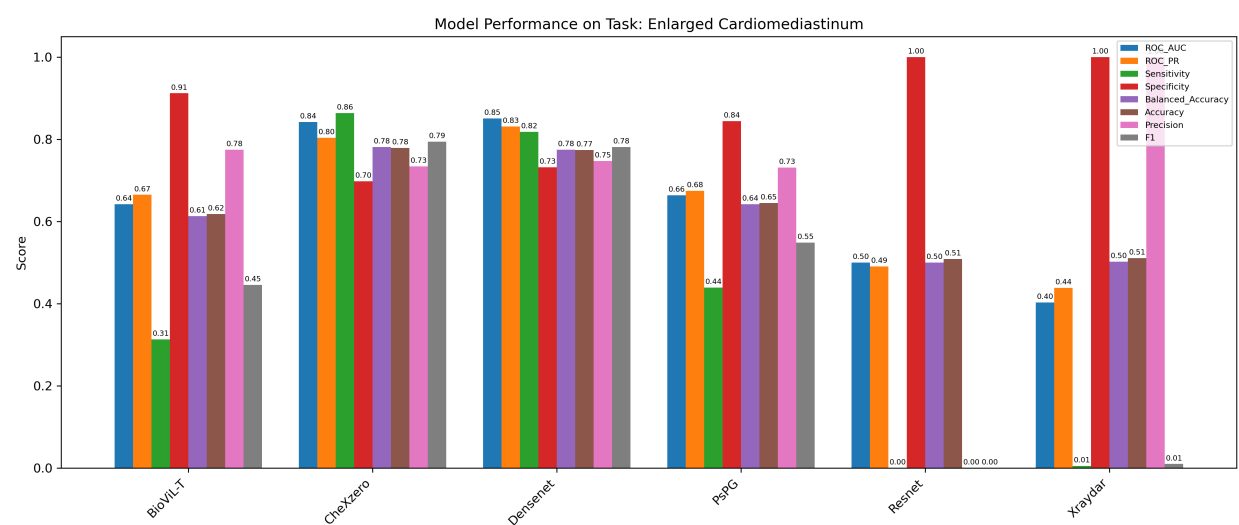
Consolidation



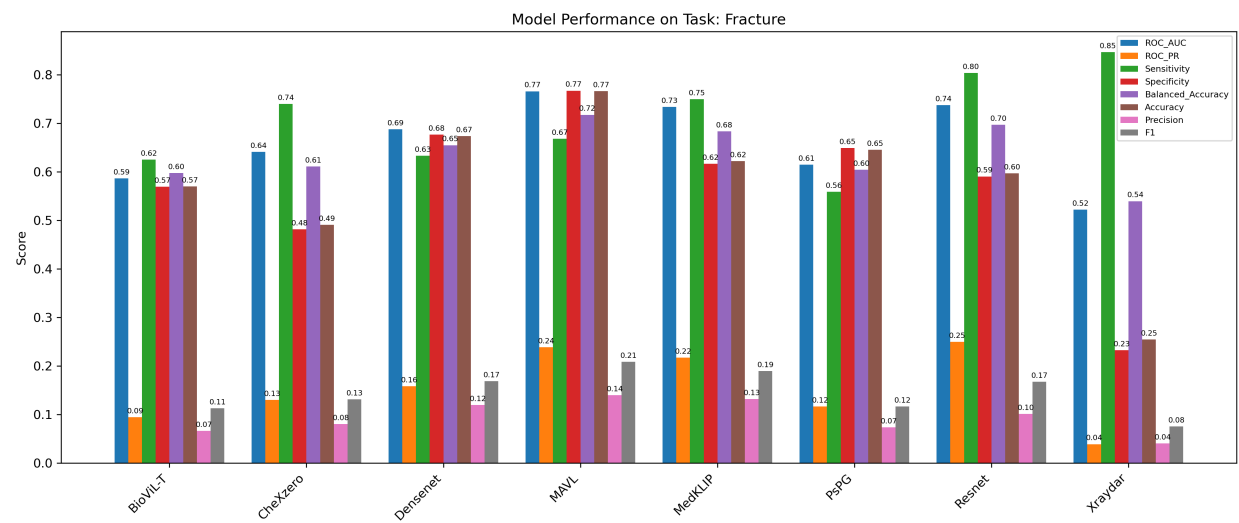
Edema



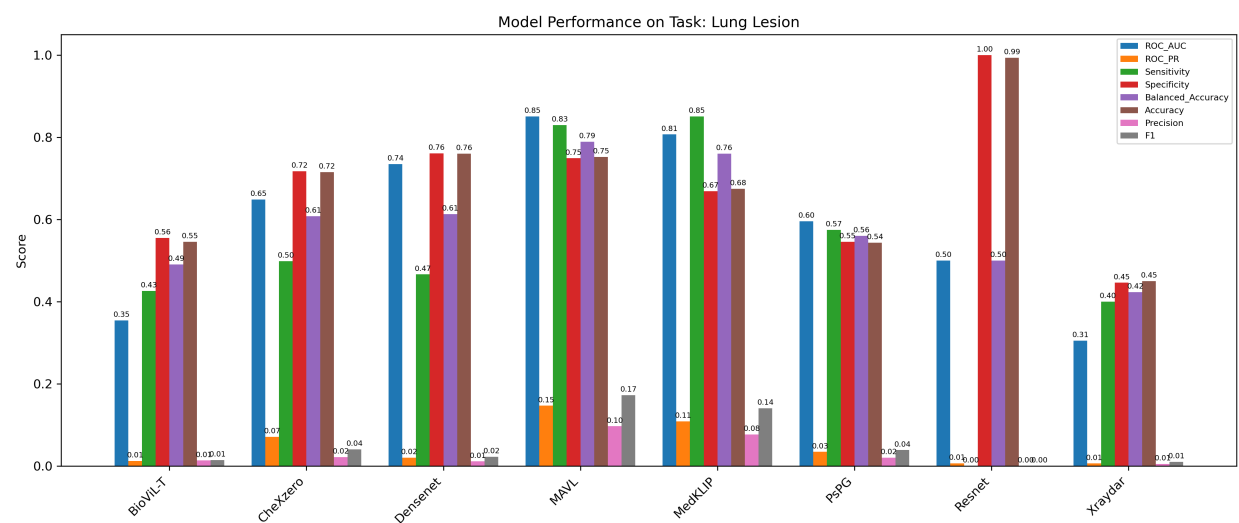
Enlarged Cardiomedastinum



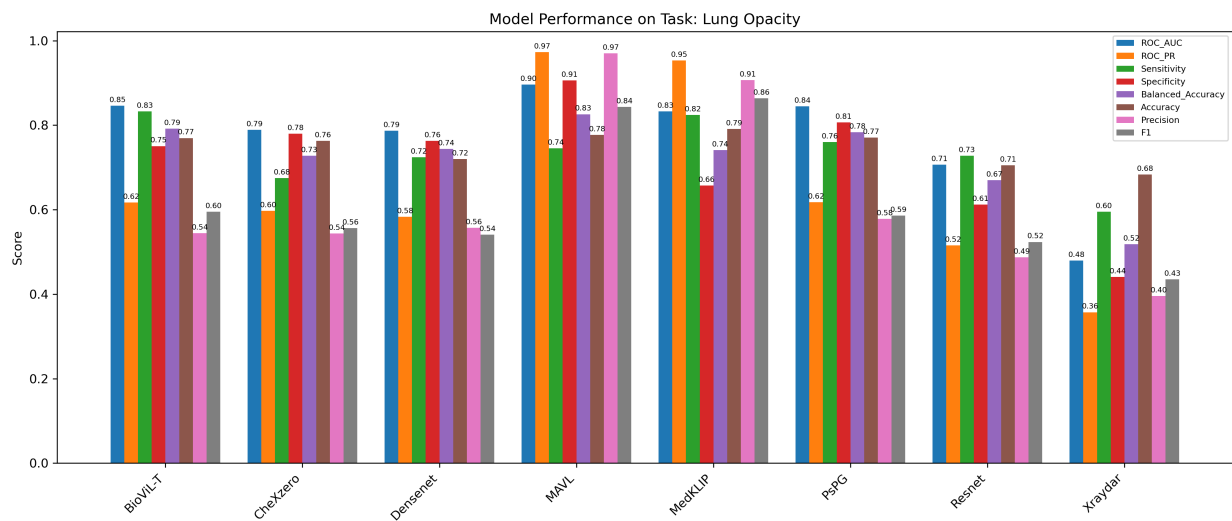
Fracture



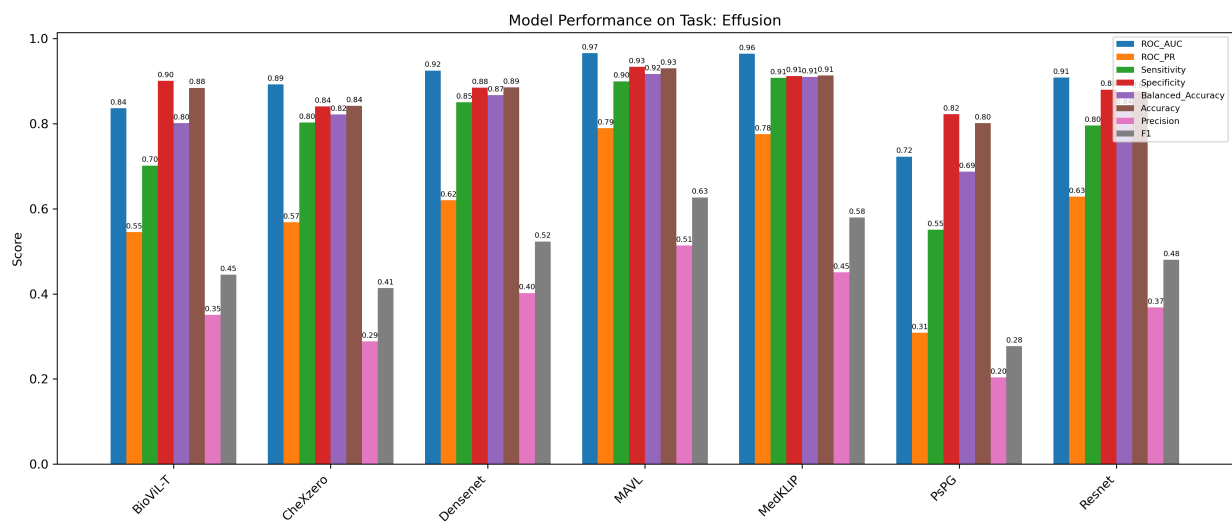
Lung Lesion



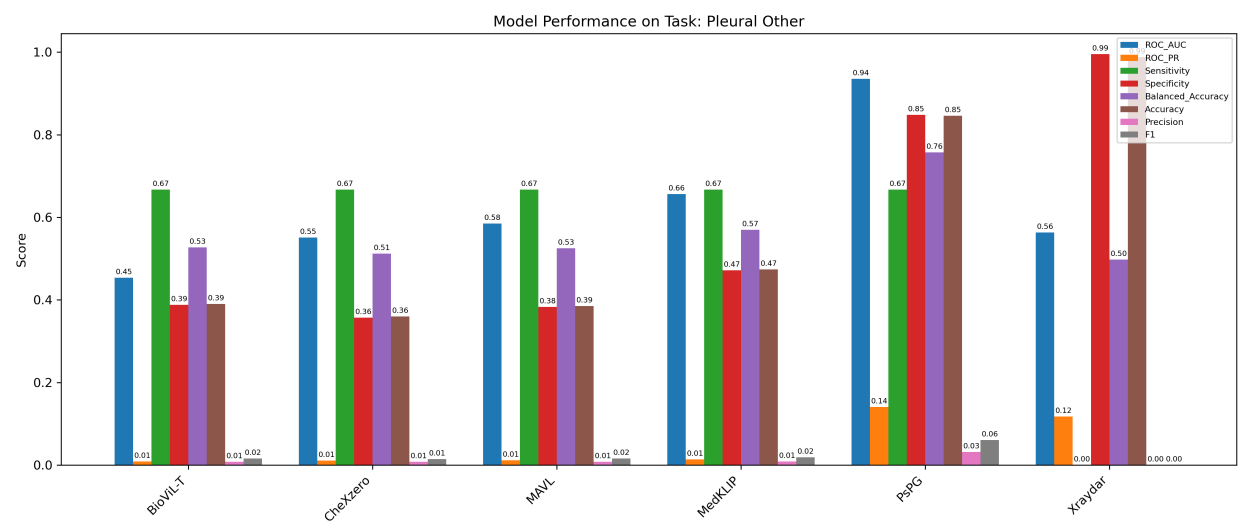
Lung Opacity



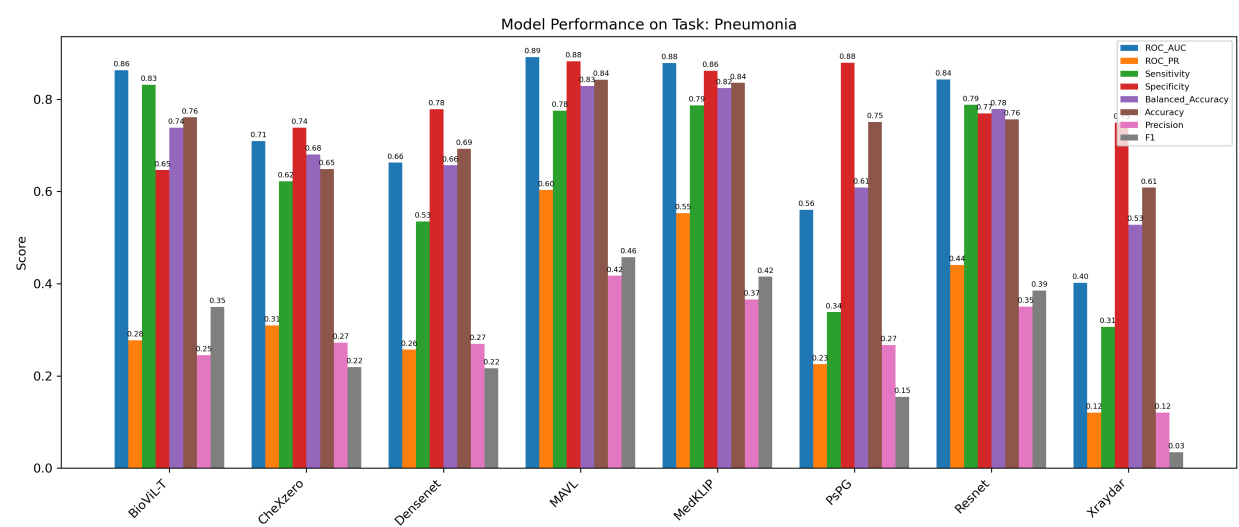
Effusion



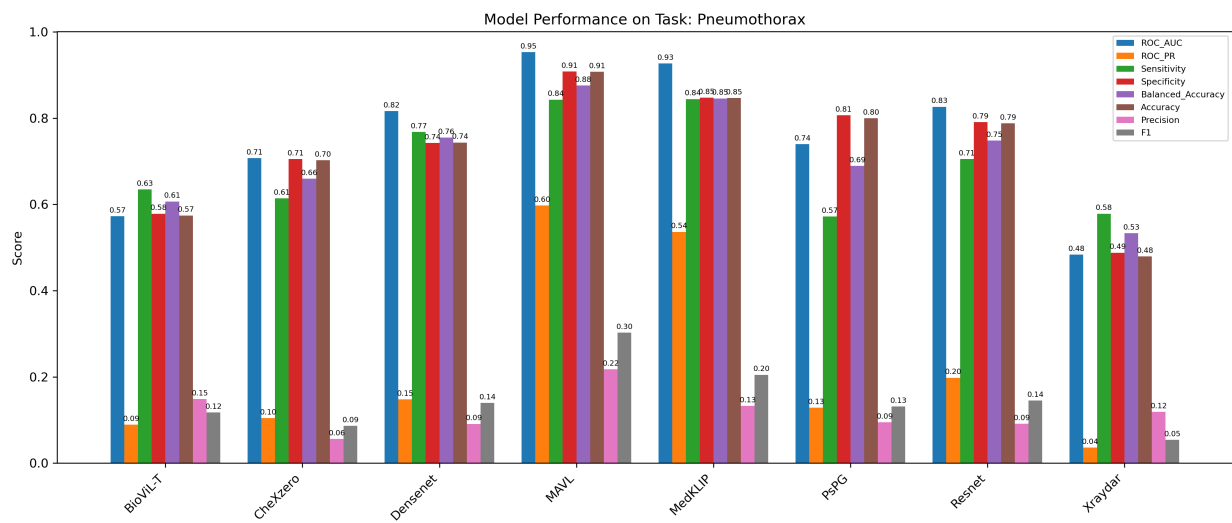
Pleural Other



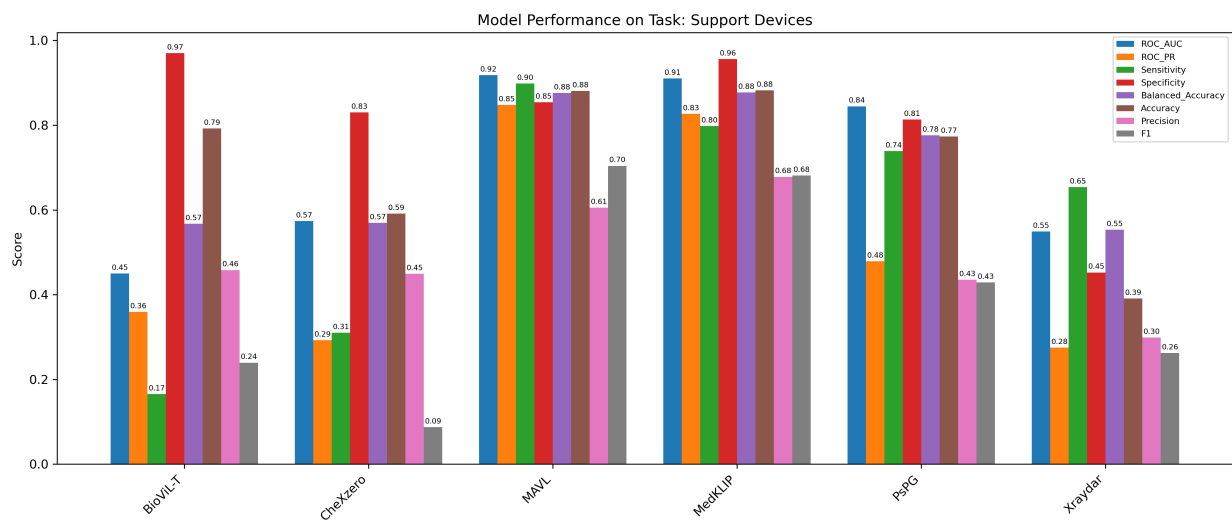
Pneumonia



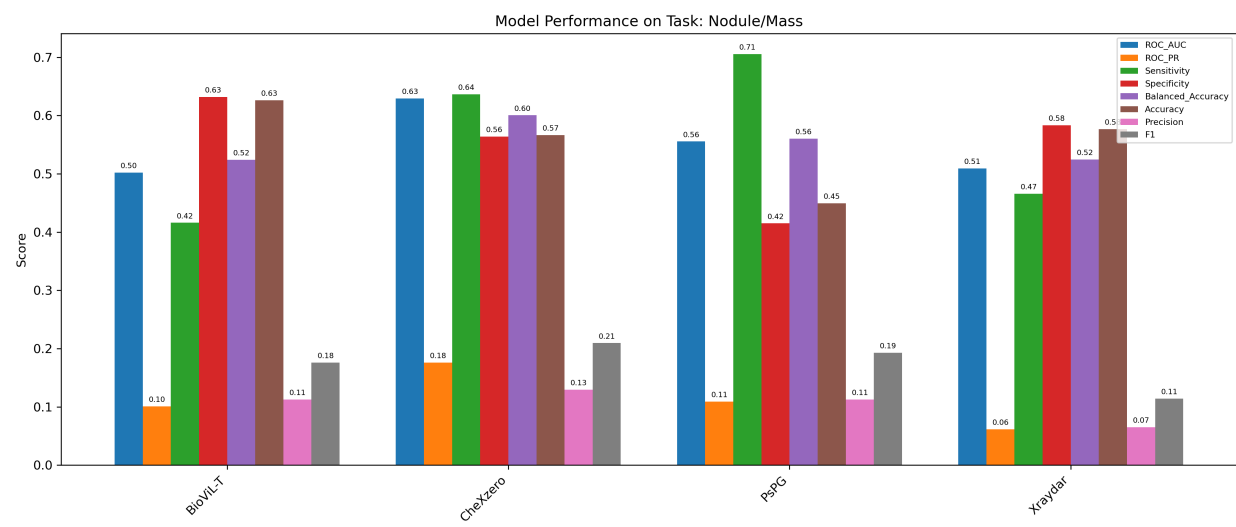
Pneumothorax



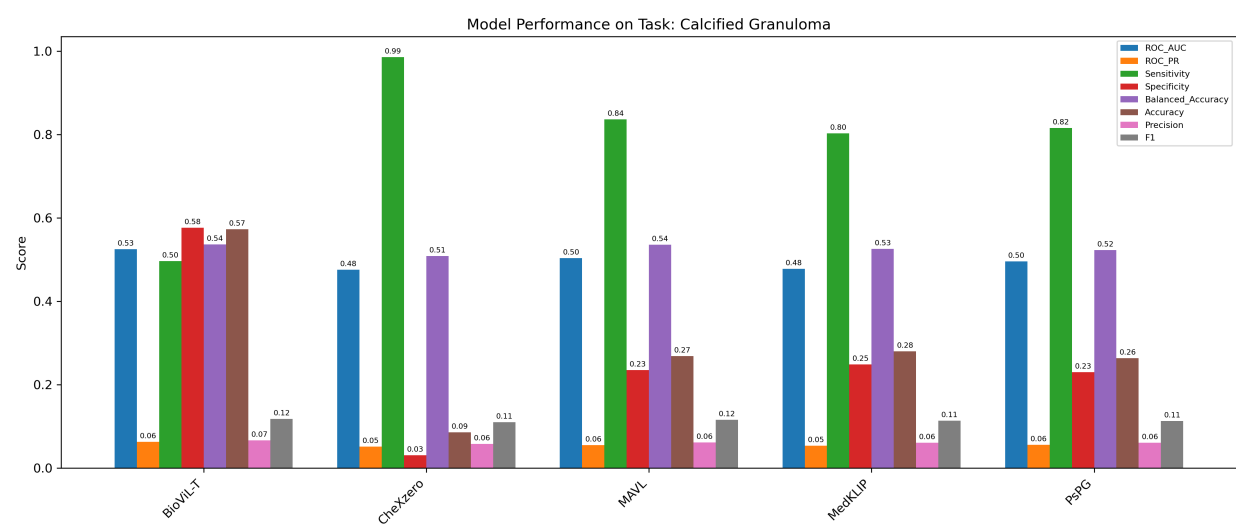
Support Devices



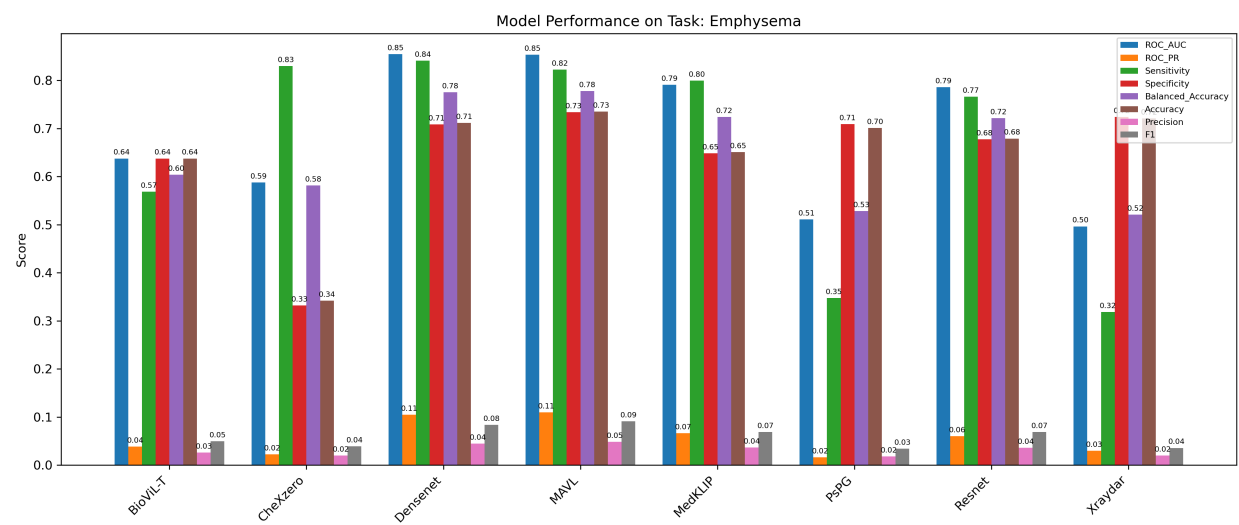
Nodule/Mass



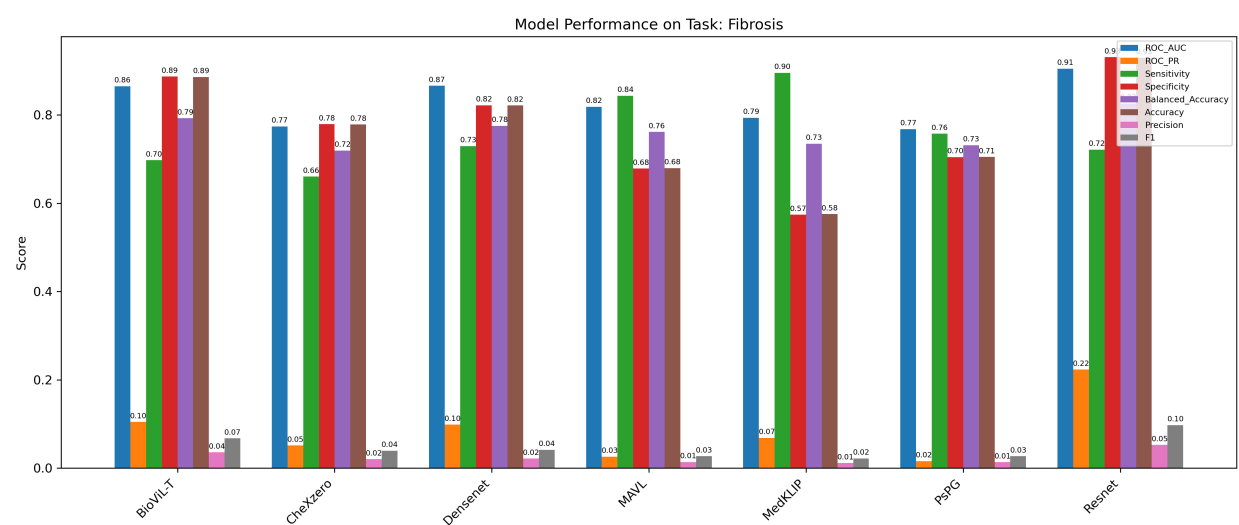
Calcified Granuloma



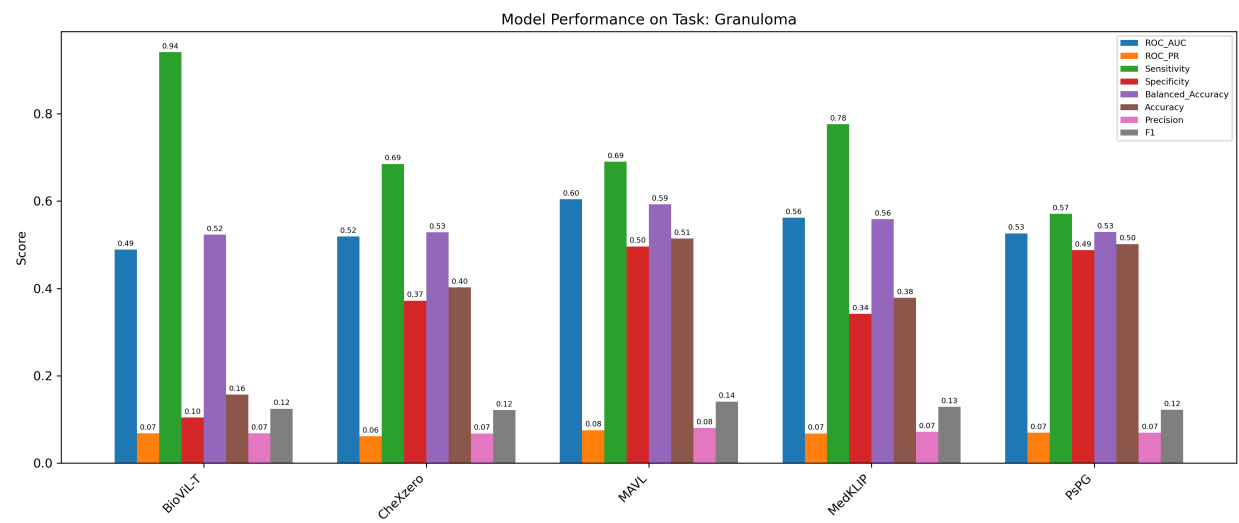
Emphysema



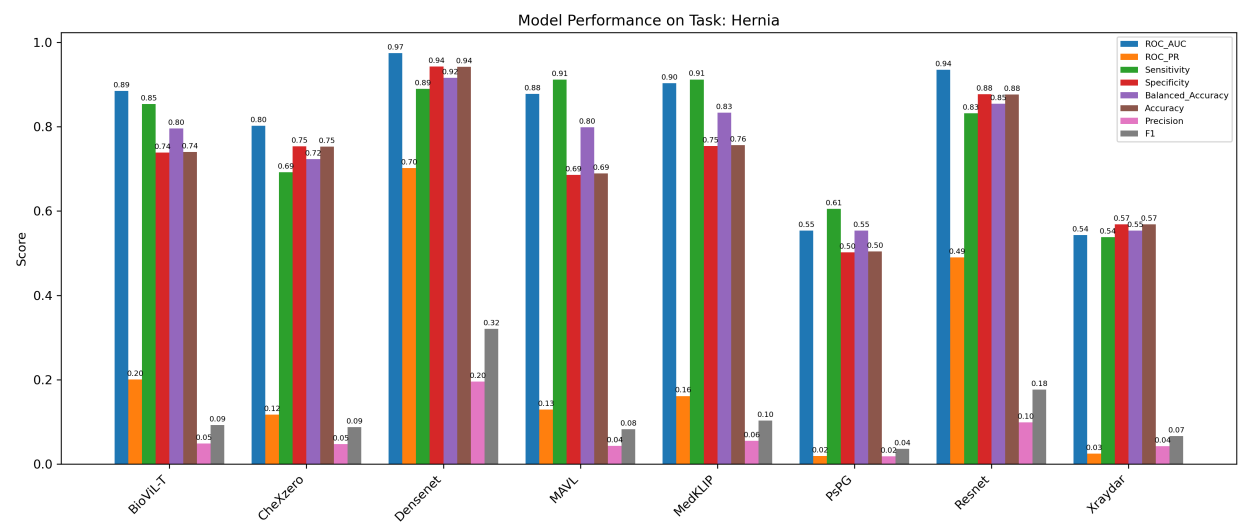
Fibrosis



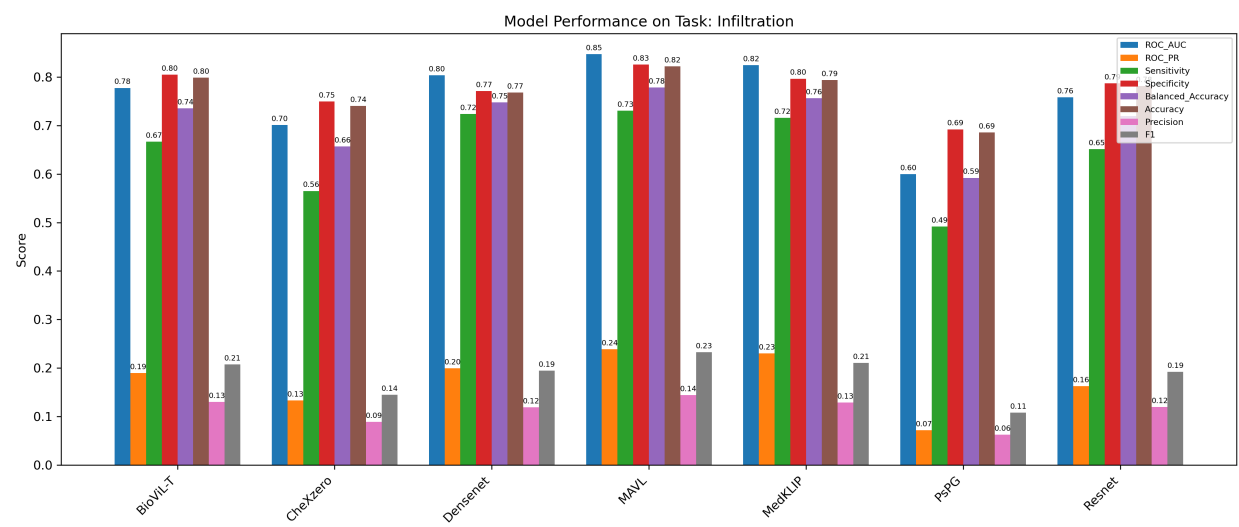
Granuloma



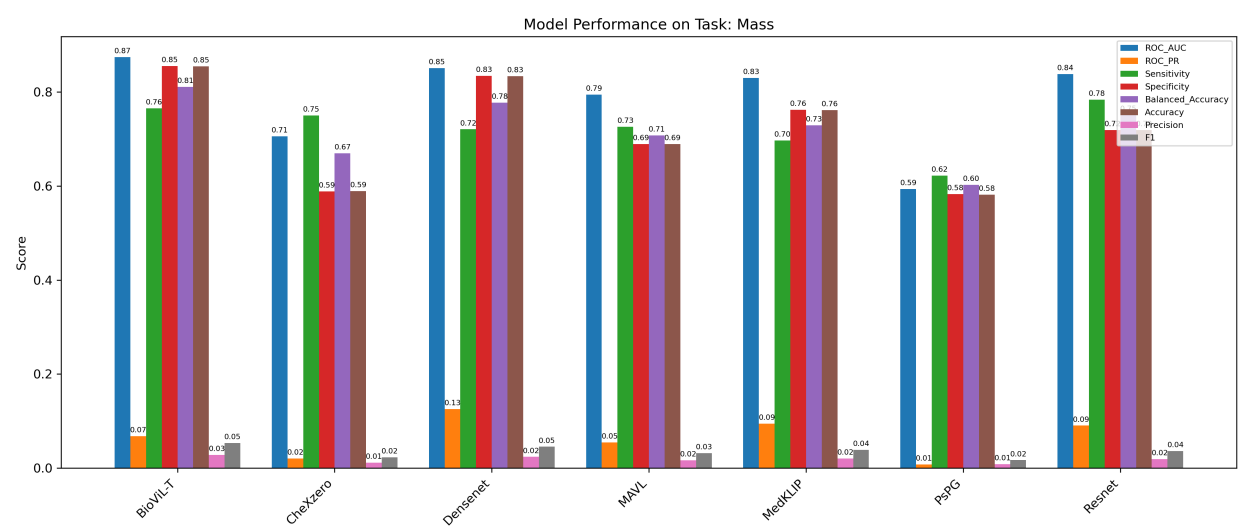
Hernia



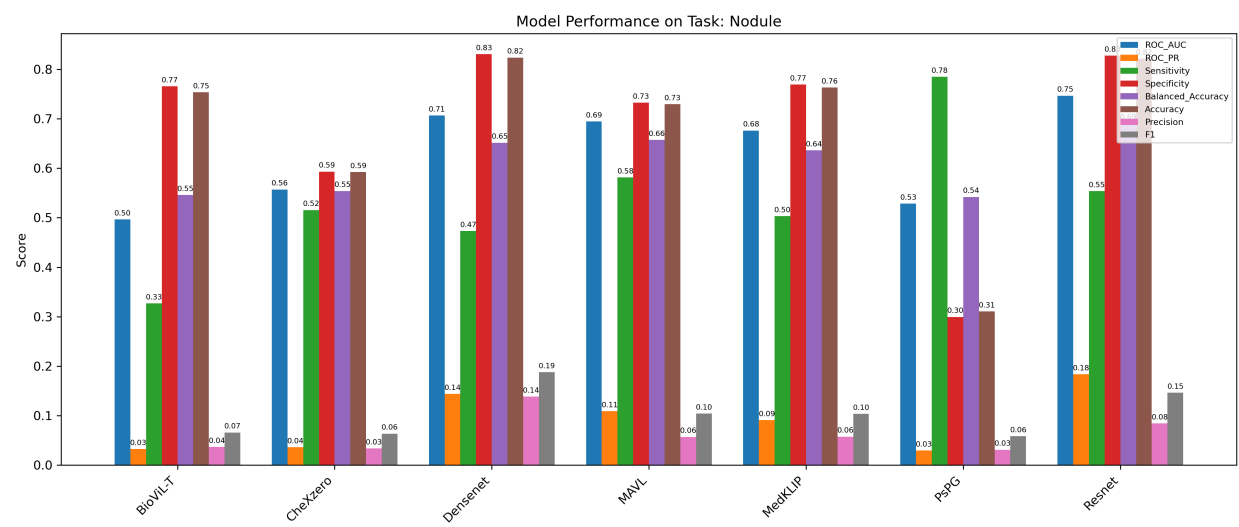
Infiltration



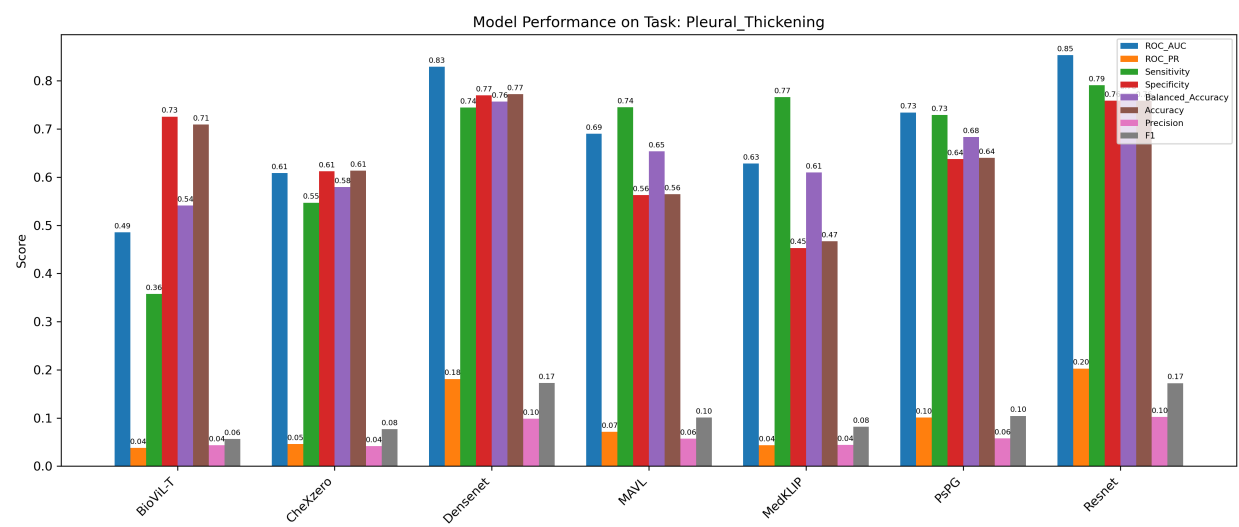
Mass



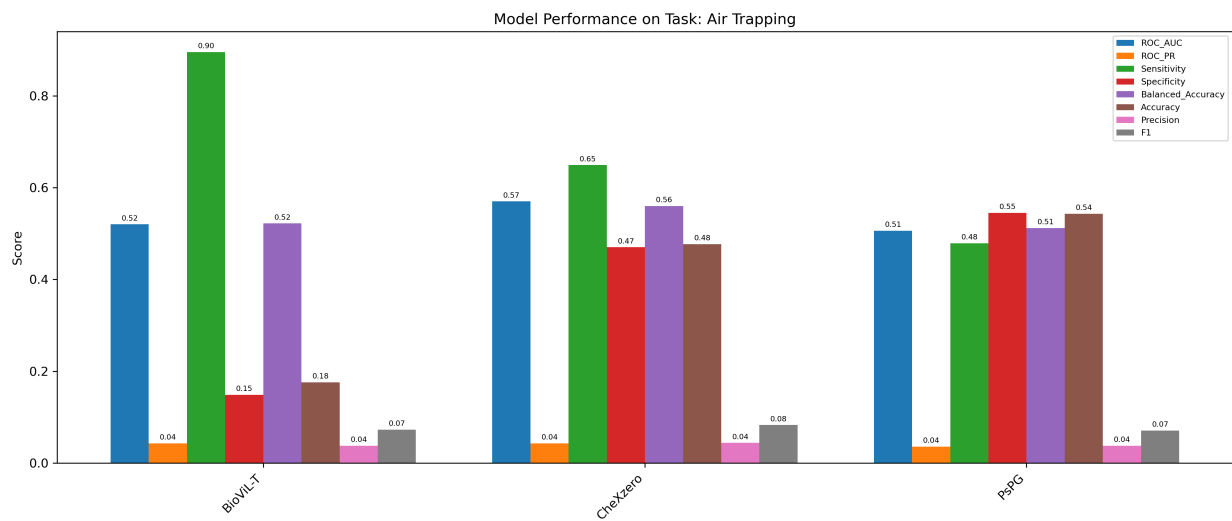
Nodule



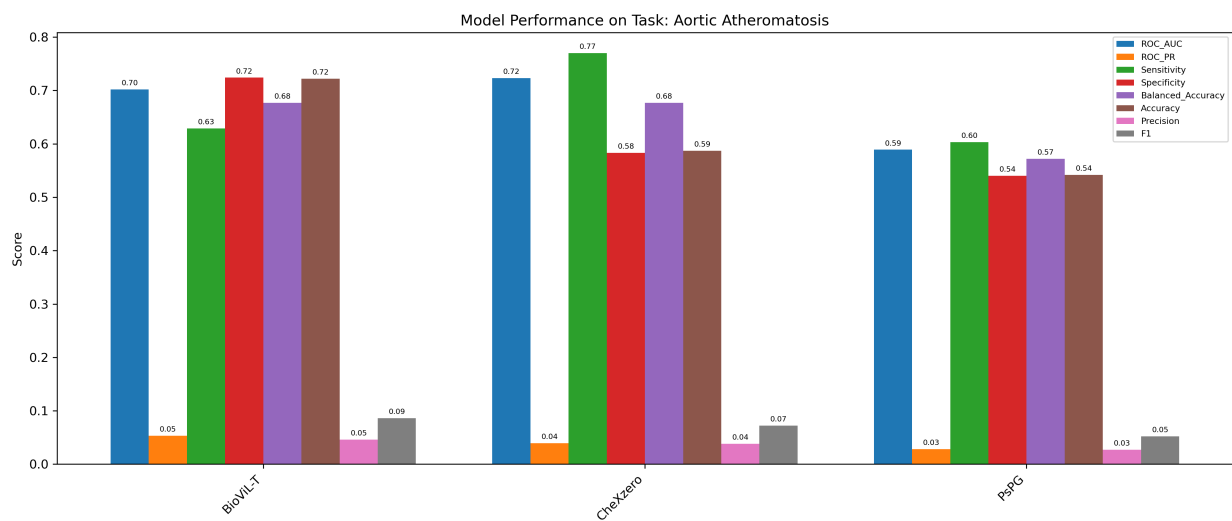
Pleural_Thickening



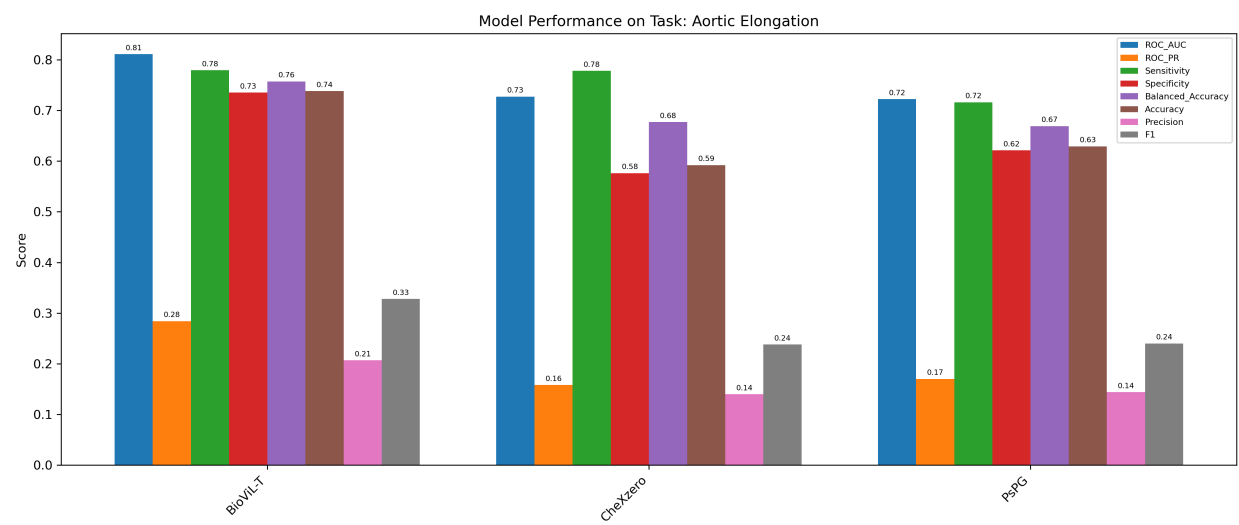
Air Trapping



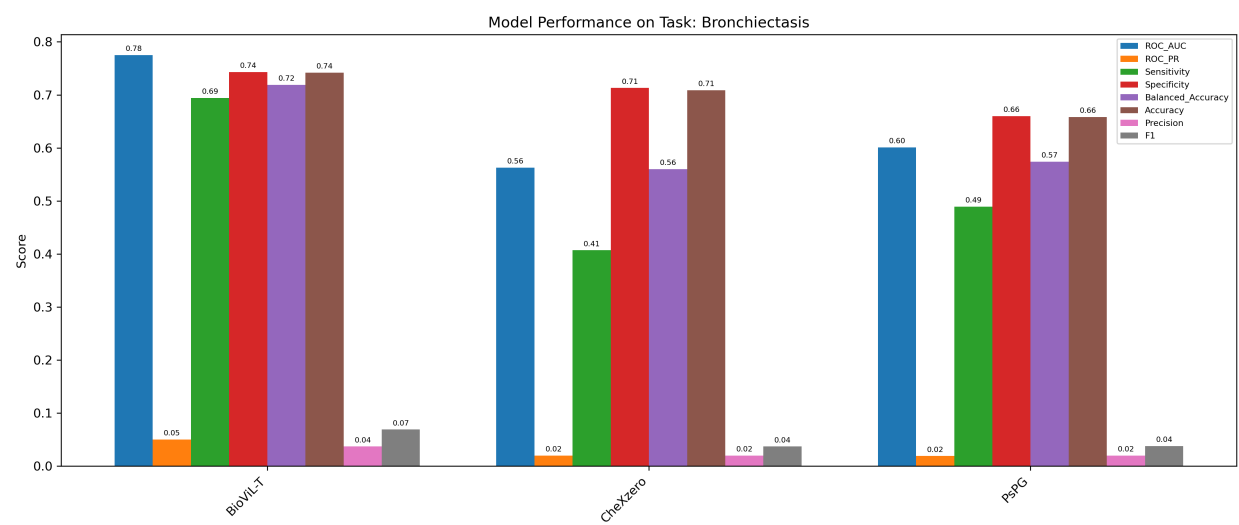
Aortic Atheromatosis



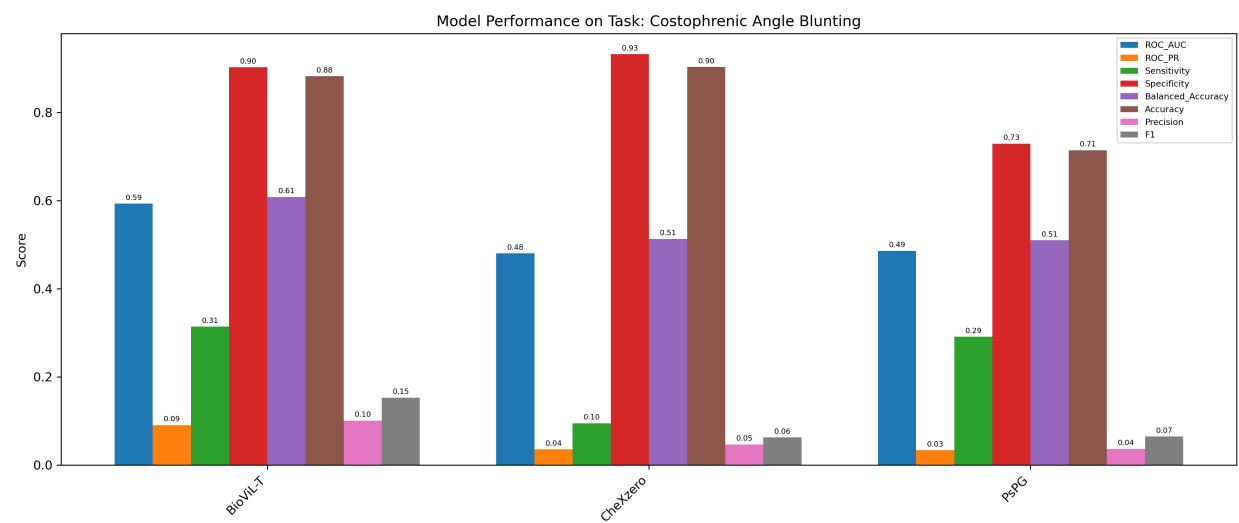
Aortic Elongation



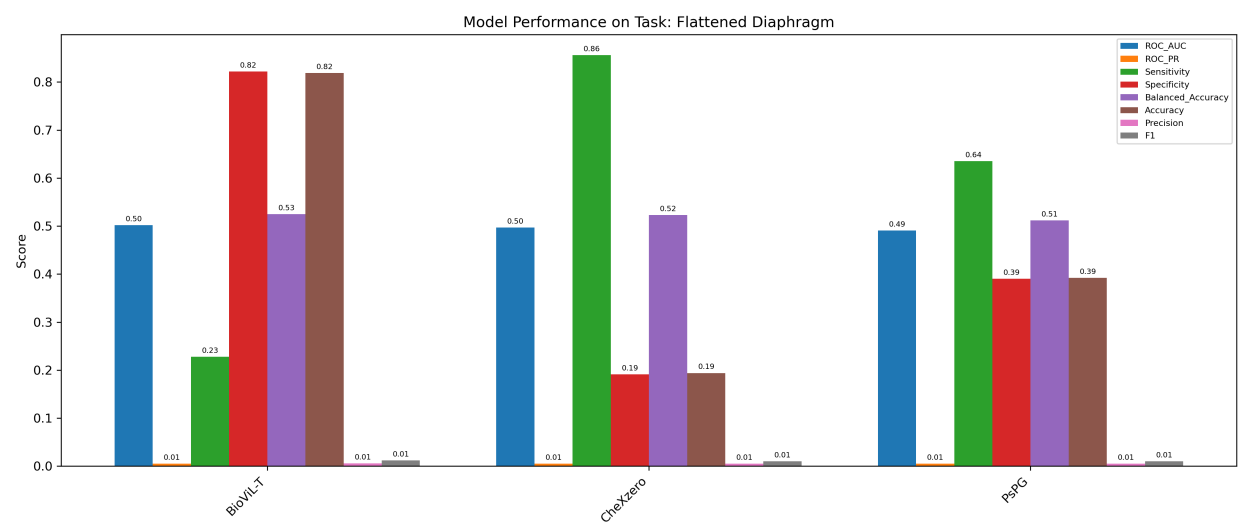
Bronchiectasis



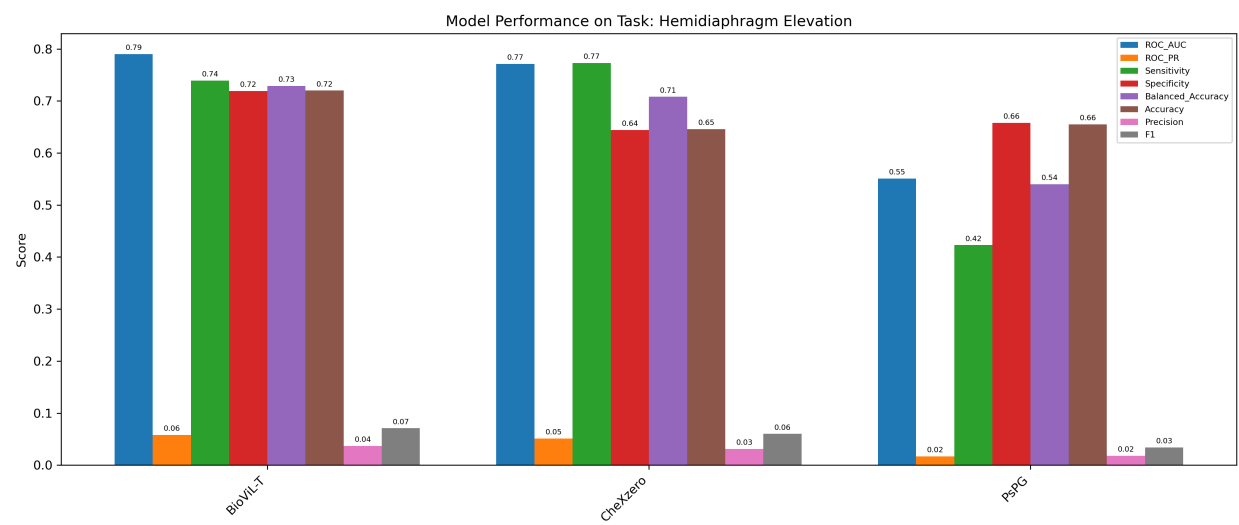
Costophrenic Angle Blunting



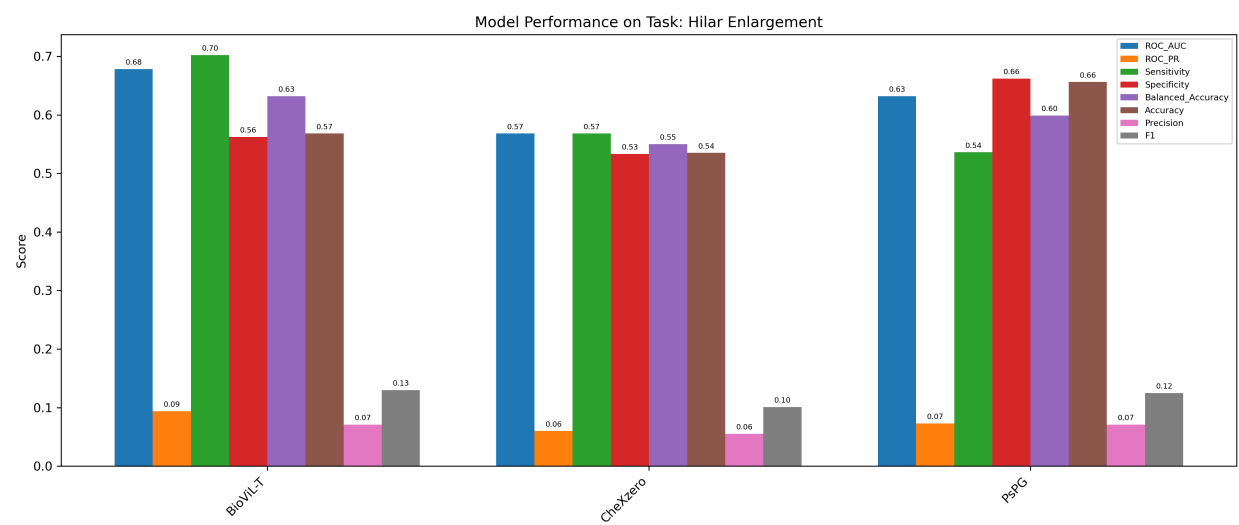
Flattened Diaphragm



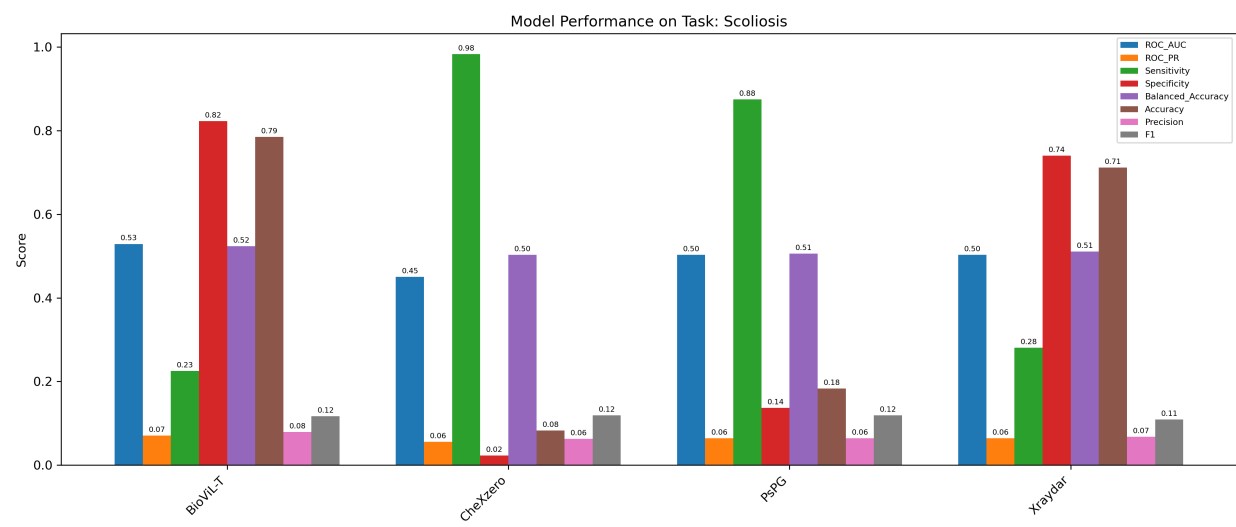
Hemidiaphragm Elevation



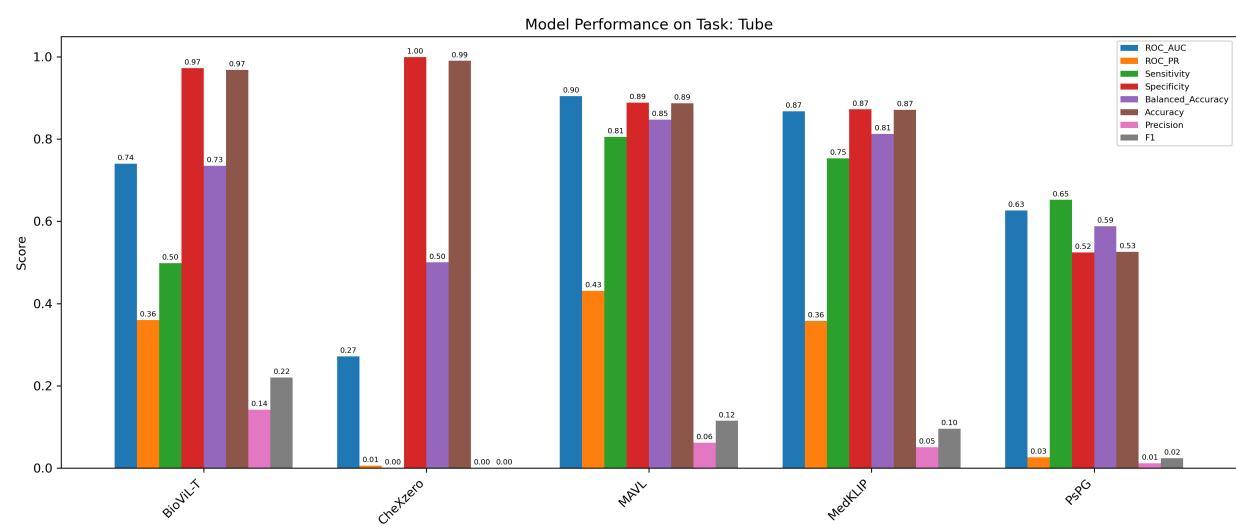
Hilar Enlargement



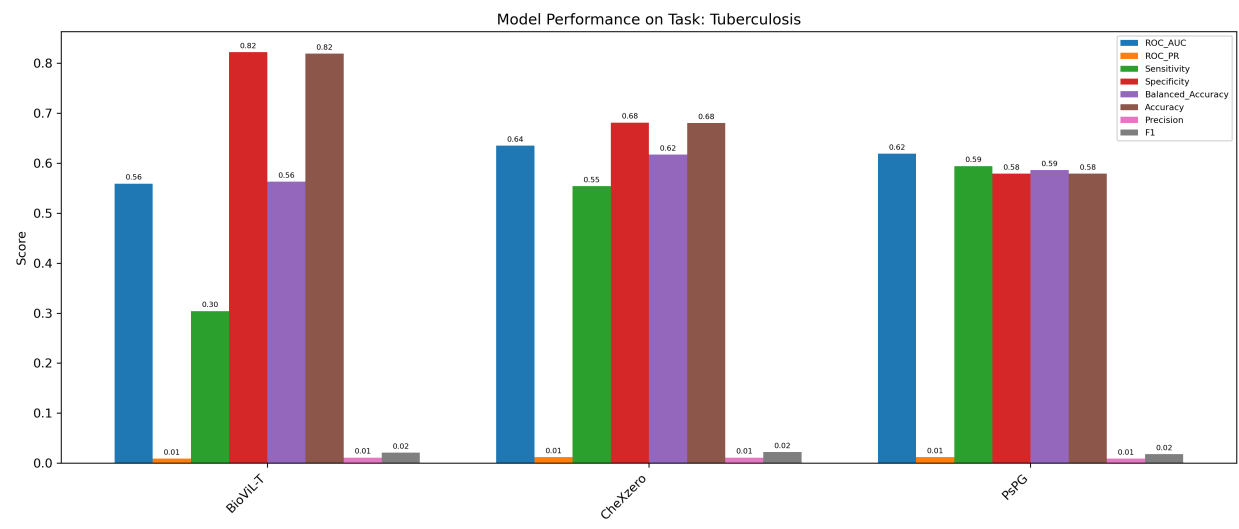
Scoliosis



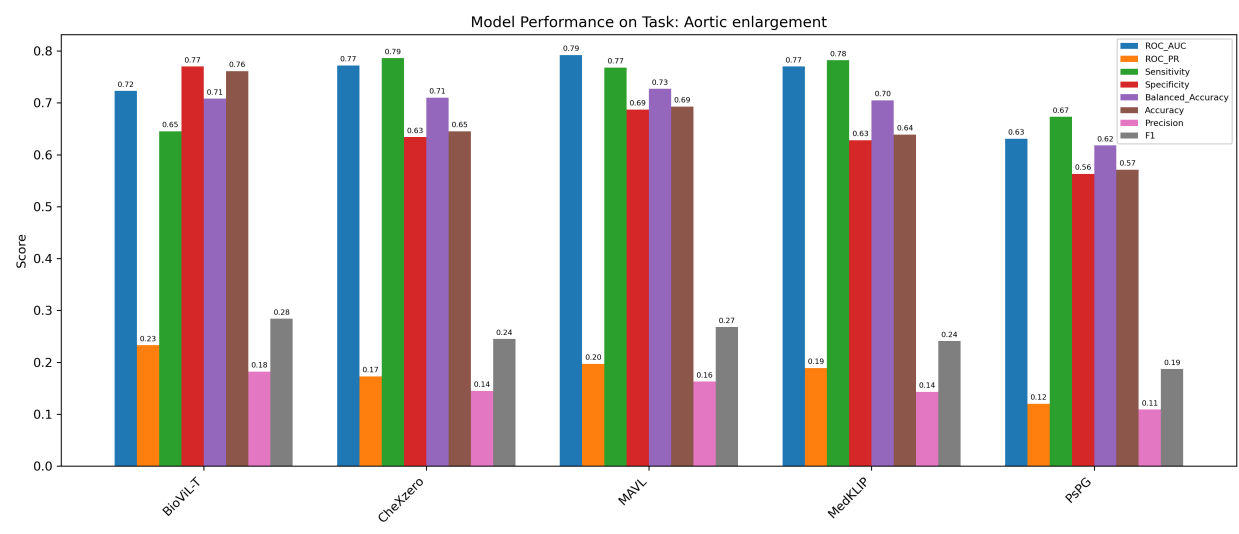
Tube



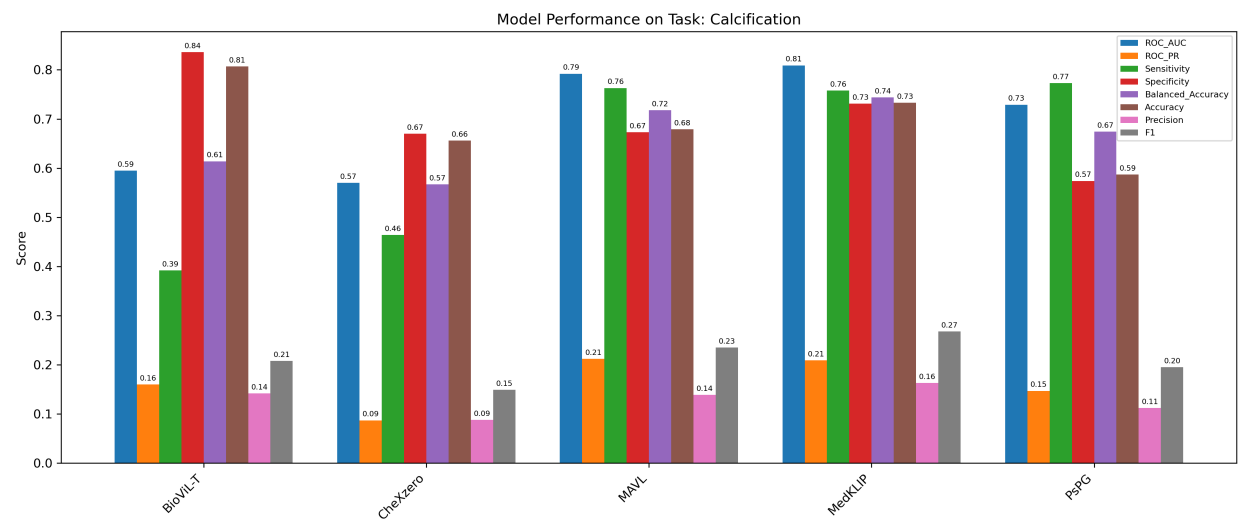
Tuberculosis



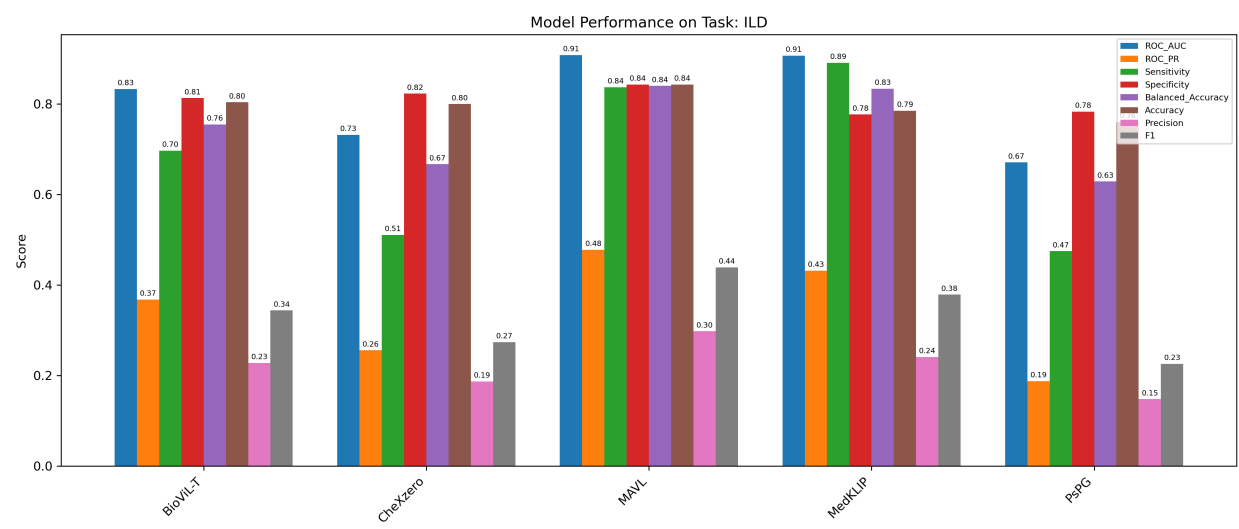
Aortic enlargement



Calcification



ILD



Pulmonary Fibrosis

